FEW-ELECTRON SIGNALS IN LIQUID XENON DARK MATTER DETECTORS

by

Abigail Kopec

A Dissertation

Submitted to the Faculty of Purdue University

In Partial Fulfillment of the Requirements for the degree of

Doctor of Philosophy

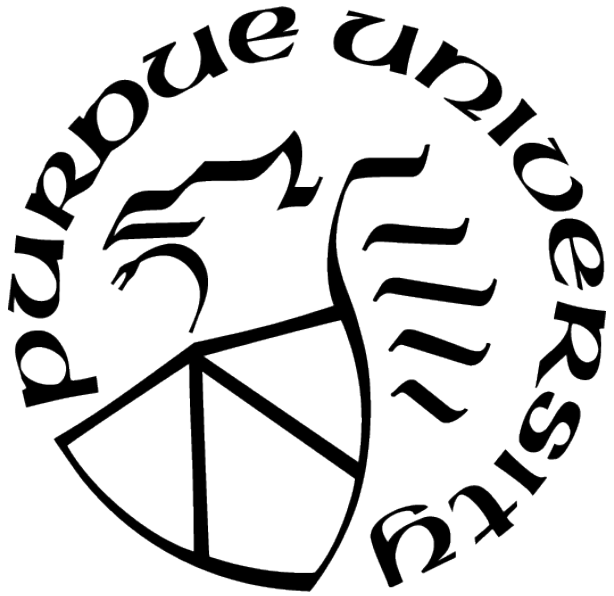

Department of Physics and Astronomy

West Lafayette, Indiana

December 2021

THE PURDUE UNIVERSITY GRADUATE SCHOOL
STATEMENT OF COMMITTEE APPROVAL

Dr. Rafael F. Lang, Chair

Department of Physics and Astronomy

Dr. Timothy Matthew Jones

Department of Physics and Astronomy

Dr. Martin Kruczenski

Department of Physics and Astronomy

Dr. Dan Milisavljevic

Department of Physics and Astronomy

Approved by:

Dr. Gabor Csathy

To my family and friends for loving and supporting me regardless of what I do, and to the fuzzy dark matter I find under my bed: my own little bunny rabbit. I will hug her, and squeeze her, and pet her, and pat her, and call her George.

☺ ♡ ★

ACKNOWLEDGMENTS

I acknowledge the guidance and support of the Purdue Dark Matters Research Group past and present, particularly Dr. Rafael F. Lang, Amanda Baxter, Juehang Qin, Dr. Michael Clark, Dr. Shengchao Li, Dr. Cassie Reuter, Dr. Jacques Pienaar, and Dr. Darryl Masson. My work was made more interesting by the constantly changing army of undergrads, and the teaching and mentoring experience has been invaluable. I appreciate the help and advice from the XENON and LBECA Collaborations. Thanks be to Amy Damitz and Dr. Dan Elliott for enabling the fiber illumination of ASTERiX. This work was made possible through funding from the National Science Foundation, Department of Energy, and the Indiana Space Grant Consortium, as well as support through the Department of Physics and Astronomy, and the Purdue Data Mine initiative. I also acknowledge the inspiration from my High School Physics Teacher Mrs. Carol Sullivan, my undergraduate research advisor Dr. Kenneth Burch, and former graduate student mentor Dr. Claire Watts. I am grateful that I could live closer to my Grandma for a few years, inspiring me to live my best life and take care of myself. I endeavor to be as strong, compassionate, and brilliant as my Nana. I lastly am thankful for the love and happy memories with Grandpa, Papa, and Aunt Barb.

TABLE OF CONTENTS

LIST OF TABLES

LIST OF FIGURES

ABBREVIATIONS

ASTERiX	A Small TPC for Experimental Research in Xenon
BiPo	Bismuth-214 beta decay and prompt Polonium-214 alpha decay
CEvNS	Coherent Elastic Neutrino-Nucleus Scattering
DPE	Double photoelectron
GeV	Giga-electron-Volt
MACHO	Massive Compact Halo Object
PE	Photoelectron
PID	Proportional-integral-derivative [controller]
PMT	Photomultiplier Tube
PTR	Pulse Tube Refrigerator
QCD	Quantum Chromodynamics
SE	Single Electron
SPE	Single photoelectron
TPC	Time Projection Chamber
WIMPs	Weakly Interacting Massive Particles

GLOSSARY

alpha decay	Nuclear decay where an unstable nucleus ejects two protons and two neutrons (a Helium-4 nucleus) called an alpha particle.
axions	Theorized particles to clean up the strong CP Problem, and a potential dark matter candidate.
baryonic matter	Normal matter made of atoms, since protons and neutrons are baryons.
baryons	Composite particles made of three quarks, such as protons and neutrons.
beta decay	Nuclear decay where a neutron turns into a proton: a down quark turns into an up quark by radiating a W^- boson, which promptly decays into an electron and an electron-flavored anti-neutrino.
bosons	Integer spin particles that are allowed to have identical quantum numbers among particles in an ensemble. Fundamental bosons include force-carrying gluons, photons, and the W, Z, and Higgs boson.
CP violation	Charge conjugation (C) and parity (P) symmetries are broken, so matter and anti-matter do not quite behave the same with opposite charge. Evident in the weak force.
dark matter	Unknown invisible matter controlling the universe through gravitational interactions because of its high mass density.
fermions	Fractional spin particles where identical quantum numbers among particles in an ensemble is forbidden.
gamma decay	Nuclear decay, usually following either an alpha or beta decay, where the nucleus is in an excited meta-stable state and falls to the ground state by emitting a high-energy photon.
leptons	Fundamental spin 1/2 particles including charged -1 electrons, muons or tauons, or uncharged neutrinos.
mesons	Composite particles made of one quark and one anti-quark.
neutrinos	Ghost spin 1/2 particles that carry lepton flavor, have minuscule masses, no charge, and interact rarely via the Weak force.
quarks	Fundamental particles with spin 1/2 and fractional charge, +2/3 charge for up-like quarks and -1/3 for down-like quarks.
S1	The initial scintillation signal from excited atoms de-exciting
S2	The secondary scintillation light from electrons exciting atoms in the amplification region of a TPC (gas in a dual-phase TPC). The amount of scintillation is proportional to the number of electrons.
scintillation	Light produced by the de-excitation of an atom in a medium at a wavelength for which the medium is transparent, such that the photon is unlikely to be reabsorbed by the medium and can be detected with high efficiency.
strong CP problem	Inexplicable lack of CP violation in the strong force.

ABSTRACT

An overwhelming majority of matter in the Universe is dark matter, a substance unlike anything we know. Detecting dark matter particles requires ruling out observed phenomena caused by known particles. This thesis advances efforts toward the detection of dark matter using one of the most sensitive particle detection technologies: the dual-phase liquid xenon time projection chamber. Specifically, data from the XENON1T Experiment, located in Italy, and the Purdue small-scale ASTERiX detector are analyzed. A background of Lead-214 beta decay events can be mitigated by tracing the radioactive Radon-222 decay chain in XENON1T. However, a preliminary reduction of background has a high cost to exposure. Research on several topics was conducted with Purdue undergraduates, including a search for dark matter particles up to the Planck Mass, characterizing backgrounds due to muons, and searching for Boron-8 solar neutrino signals. XENON1T single-scatter dark matter limits were extended to a particle mass of 10^{18} GeV/c^2. The ASTERiX detector was modified to characterize a significant background to the smallest detectable energy signatures: single- and few-electron ionization signals. Infrared light was determined to be ineffective at reducing this background, and their rates were observed to decrease inversely with time since an energetic interaction according to a power law. The rates of single- and few- electron backgrounds increase linearly with increased applied extraction fields and increased depth of the initial interaction in the detector. These results indicate that these backgrounds originate at the liquid-gas interface of dual-phase detectors. In exploring a single-photon threshold for initial scintillation signals, a previously unconsidered background of large dark count signals in the photosensors became apparent. The high background of small ionization signals and large dark count signals deterred a search for Boron-8 solar neutrino interactions in XENON1T. These studies are vital to mitigating backgrounds and improving the sensitivity of liquid xenon time projection chambers to new physical phenomena.

1. INTRODUCTION

The Epic of My Doctoral Thesis

Hear me, Urania, muse of astronomy. Help me to finish
all of my tasks yet ahead of me. Looking behind me like Orpheus,
five years vanish. My success depends on recalling them, writing
what I completed. The past holds the key to unlocking my future.

Here's how I started my journey in astroparticle physics.
Summer twenty-seventeen is when I began in the dark matter
research group headed by Professor Rafael Lang. For my first task:
veto Lead-two-fourteen betas that mimic the signal of hoped-for
Weakly Interacting Massive Particles. This I did using
Big Spheres, tracking in time from the alpha decay of Polonium
(parent) to Bismuth-Polonium (daughters) with Lead in between them.
Next, I constructed the ASTERiX research detector while also
searching for rare interactions from muons, or particle tracks, in
XENON-one-ton with the help of an army of undergrad students.
Energetic collisions of particles with liquid xenon result in
signals from single, to several, electrons appearing for seconds.
I, in the ASTERiX research detector, discovered that nearly
nothing affects how the rates of electrons evolve with time. See the
Power Law with a power of negative one always present.
Easy enough to avoid but, by cutting exposure, we limit
our sensitivity. Actual particles that interact with
xenon we know give both light and electrons. I looked for the photons
buried in light sensor noise. Scintillation from xenon can cause a
double photon-like signal. However the noise and electron
backgrounds are higher than practical for a neutrino search even.
Now I am pausing to graduate. I will continue with XENON.

What is the Universe made of? The Standard Model of particle physics contains a host of elementary particles that explain certain behaviors of matter very well. However, it is not comprehensive, and astrophysical observations indicate that only about 15% of the overall matter mass density in the Universe is made of known manifestations of these Standard Model particles [1]. The other 85% of matter is invisible, non-relativistic, and not obviously interactive–other than via gravity. This substance we call dark matter. There are many promising theories, and many emerging experiments to tease out what dark matter's particle (or particles) might be.

A world-leading technology to search for dark matter is the dual-phase liquid xenon time projection chamber. Beyond dark matter, these highly versatile particle detectors are sensitive to a wealth of rare interactions and natural phenomena [2]–[5].

In this chapter, I summarize relevant background knowledge that has both motivated my thesis work and served as its basis. I provide a rudimentary introduction to particle physics and delve into the mystery of dark matter. I then brush over a few dark matter models before describing the liquid xenon time projection chamber and how it can detect such particles.

1.1 Introduction to Particle Physics

Beta Decay - A Shape Poem

At a glance, everything tangible is made of atoms, which, in turn, are comprised of protons, neutrons, and electrons. Even protons and neutrons have constituent particles, known as quarks. Figure 1.1 lists the known fundamental particles of the Standard Model of Particle Physics, and gives some of their quantum numbers. Unlisted values for certain particles' parameters are assumed to be zero [6].

Protons are characterized by two up quarks and a down quark, and neutrons have one up quark and two down quarks. By having three quarks each, these composite particles are called baryons, and baryonic matter is synonymous to matter made of atoms. While up and down quarks are the most common, they each have two heavier counterparts that act similarly. They appear to have all the same possible quantum numbers, but they have heavier

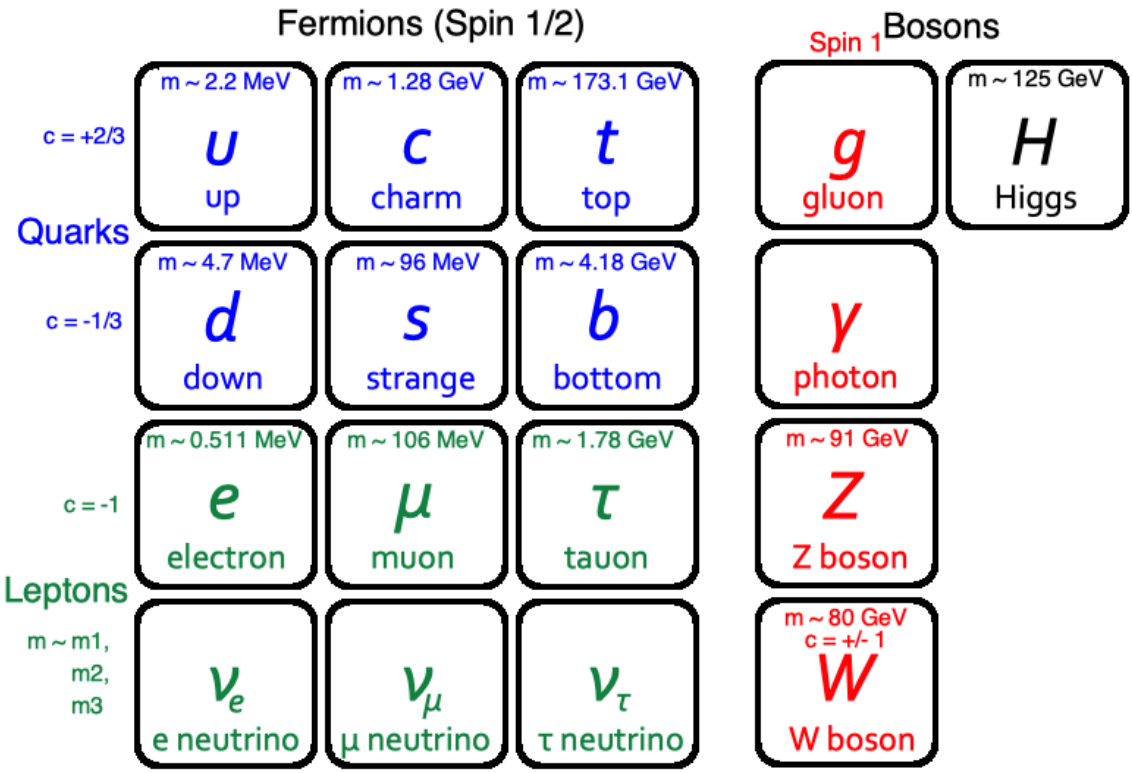

Figure 1.1. The current Particles in the Standard Model and their relevant quantum numbers and masses. The quarks are in blue and the leptons are in green. Force-mediating vector bosons are red, and the scalar Higgs boson is black. Adapted from information in Reference [6].

masses and are very unstable. The up-like quarks include the charm and top quarks. The down-like quarks include the strange and bottom quarks. Even the electron has two heavier counterparts: the muon and the tauon (or tau/tau lepton). These nine known particles and their anti-particles essentially compose matter as we know it, and all have intrinsic electric charge [6]. However, they are insufficient to describe how matter behaves dynamically in time and space, gaining and losing energy or even transforming into other particles. I have also neglected to mention neutrinos, yet.

A common exchange of energy comes in the form of light. The photon is the fundamental particle mediating the electromagnetic force, affecting how charged particles behave. A free electron passing nearby atoms will be decelerated by local electric fields from the atoms'

positive nucleus and bound negative electrons. This energy lost via photons is known as bremsstrahlung radiation [7]. A charged particle entering a substance and traveling faster than the speed of light in that medium will radiate a shock wave of blue Cherenkov light [8]. An electron bound in an atom might have more energy than the ground state configuration for that atom, making it unstable in such an excited state. The electron will radiate the extra energy in a photon and drop to a lower energy state. The nucleus itself can be in an excited state after a nuclear decay, emitting a high energy photon, known as a gamma, as it relaxes. As an uncharged and massless particle, photons are often the product of the annihilation of particles and corresponding anti-particles [6]. Since light interacts easily with Baryonic matter, we rely heavily on it to learn about our surroundings. Other electromagnetic effects generally observed at a macroscopic scale can be explained within the Standard Model framework. For motion resulting from the attraction and repulsion of charged objects and magnets, there are virtual photons in the fields that the objects convert to kinetic energy.

The functions of the other bosons are more abstract. Within a composite particle of quarks (such as a baryon) the quarks are held together by massless gluons, the mediators of the Strong Nuclear Force. When a neutron beta decays into a proton, it does so through the Weak Force. One of its down quarks transforms into an up quark by emitting a W^- boson that decays into an electron and an anti-electron neutrino, as in the introductory shape poem. Neutrinos are governed by the Weak Force. Hence, they are weakly interacting and require a charged W^+ or W^- boson for charged current interactions where there is a transfer of net charge and energy to the final products, or the Z boson for neutral current interactions where there is only a transference of energy. The rare Coherent Elastic Neutrino-Nucleus Scattering (CEvNS) process is an exchange of a Z boson between a neutrino and an atomic nucleus [9]. The Higgs boson is the quantum of the omnipresent Higgs field [10]–[12]. Particles interacting with the Higgs field gain energy that contributes to measured mass. However, mass is a difficult concept, since kinetic energy contributes to mass. In the case of a proton or neutron, the kinetic energy of the constituent quarks contributes more to the baryon's 1 GeV/c^2 mass than the sum of the quarks' masses, which is only about 10 MeV/c^2 [6].

Neutrinos are typically defined by their flavor (electron, muon, tau) rather than their masses. Weak interactions via W bosons with charged leptons, particularly electrons, historically are the best way to detect neutrinos [13]. Nuclear fusion in the Sun creates electron flavor neutrinos. Figure 1.2 shows the calculated solar neutrino flux based on the Sun's nuclear processes [14]. However, early experiments measured fluxes of solar electron neutrinos that were well below what was expected, leading to the Solar Neutrino Problem [15], [16]. Building on previous experimental results, the Sudbury Neutrino Observatory [17] solved the problem by measuring the full neutrino flux (independent of flavor) from neutrinos scattering with Deuterium in heavy water via neutral current interactions mediated by a Z boson. Somehow, many of the electron neutrinos had changed flavor in their journey from the Sun.

If the electron neutrinos changed flavor while traveling, then they could not travel at the speed of light. At the speed of light, a change in distance is instantaneous, so there is no time to undergo changes. If they are not traveling at the speed of light, they must have mass. Having been created with a specific mass and flavor, neutrinos from the Sun conserve their mass state as they travel, and oscillate their flavor. An electron neutrino could be any of three possible masses, although the m_1 state is preferred [6]. Then, based on the mass, the neutrino will change its lepton flavor at some rate. The mixing of flavor and mass states is determined with the Pontecorvo–Maki–Nakagawa–Sakata matrix [18], which governs neutrino oscillations. In addition to being difficult to detect, neutrinos have proven to be fascinating and mysterious [19].

Discovering that neutrinos have mass was a major problem for the expectations of the Standard Model of particle physics. Additionally, there remain other phenomena that its framework cannot explain. A glaring hole is the absence of any clear explanation for the force of gravity. On the scale of the Universe, the effects of gravity are everywhere.

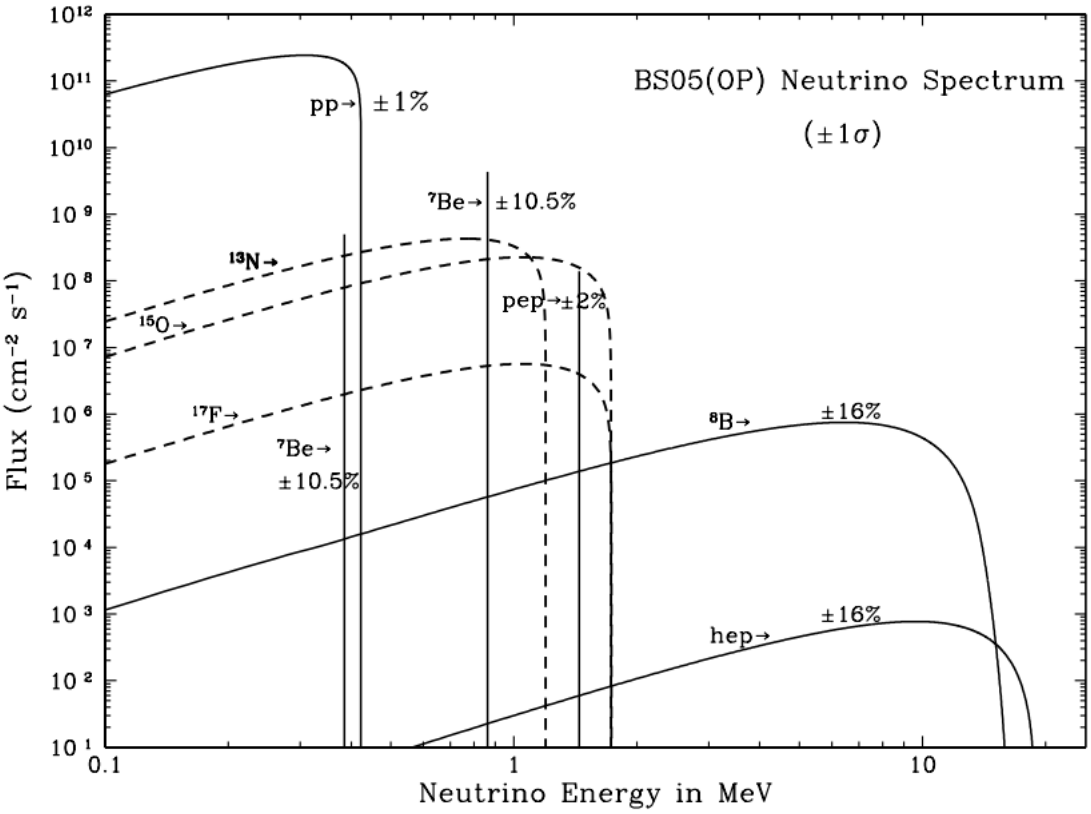

Figure 1.2. The expected neutrino fluxes per energy resulting from nuclear reactions in the Sun. From Reference [14].

1.2 Dark Matter

Elementary Enigma - A Poem

Dark Matter, it is all around.
It's nothing we can taste or see,
nor have we heard it give a sound.
Our Milky Way with it is bound
like every other galaxy.
We put detectors underground;
targets for it to hit, maybe,
as spaceship Earth ploughs through its sea.
More so in summer would it pound
us circling our Sun annually.

But on our efforts, Fortune's frowned.
No other force but gravity,
to interact with it we've found.
Yet not in hopelessness we've drowned.
Places unexplored, in theory,
remain and we must, like a hound,
sniff them out, not growing weary.
They who find it (I hope it's me)
will get a prize and be renowned:
a wonderful discovery.

Our understanding of gravity has remained nearly unchanged since Sir Isaac Newton's description of it in his Philosophiæ Naturalis Principia Mathematica [20]. By 1915, Albert Einstein introduced general relativity to account for discrepancies due to the finite speed of light (and therefore information) [21]. How much a massive object can affect the motion of another object is directly related to both objects' masses and inversely proportional to the squared distance between them. For correct units, Newton introduced his gravitational constant. Therefore, the measurement of an object's orbital motion at a given radial distance should be calculable for a given mass density profile. When applying this relation to the Milky Way Galaxy in 1922, Jacobus Kapteyn initially concluded that the observable stars would have insufficient mass to produce the measured orbital velocities of stars in the galaxy. Kapteyn was among the first to refer to the invisible substance as "dark matter" [22]. Since

then, the gravitational effects of this invisible, missing mass have appeared at all stages of the Universe's history, and at size scales from dwarf galaxies to galaxy clusters.

1.2.1 Evidence for Dark Matter

It has become increasingly clear that most of the mass in the Universe is dark matter, and that it has shaped our Universe throughout time. Hints from the first seconds of the Big Bang lead to signatures in the Cosmic Microwave Background that echo through structure formation and determine the dynamics of stars and galaxies up to the modern day. From the descriptions made by Newton and Einstein, gravity appears to work well. Except, there is a large amount of invisible mass. Dark matter's variable proportions within galaxies cannot be reconciled with any easy adjustments to the theory of gravity, such as Modified Newtonian Dynamics (MOND). Acceptance of the existence of dark matter has lead to a frenzy of experiments to search for its fundamental quantum [23].

Starting seconds after the Big Bang, the Universe had expanded and cooled such that the first protons formed out of the quark-gluon plasma. However, it was still hot and dense enough that these energetic Hydrogen nuclei collided with each other and captured neutrons to form Deuterium, Helium, and Lithium nuclei. The rates of **Big Bang Nucleosynthesis** depend on the abundance of baryonic matter (requiring rest mass energy) and the baryonic matter's kinetic energy to find other particles and fuse. We also have an expectation for the total energy density (critical density) of the Universe that informed expansion [24]. Therefore, we can observe the relative abundances of primordial Hydrogen, Helium, and Lithium isotopes left over from the Big Bang to estimate what fraction of the Universe's total energy was required to produce these nuclei in these amounts. Figure 1.3 shows the observed abundances, in boxes, relative to Hydrogen (protons), which indicate that only a few percent of the critical energy density is needed for all baryonic matter [25]. This means that we cannot yet account for a majority of the Universe's energy.

Within expected uncertainties, there is good agreement between the measured primordial abundances produced by Big Bang Nucleosynthesis, and the predictions of the **Cosmic Microwave Background**. Several hundred-thousand years after these first elements' nuclei

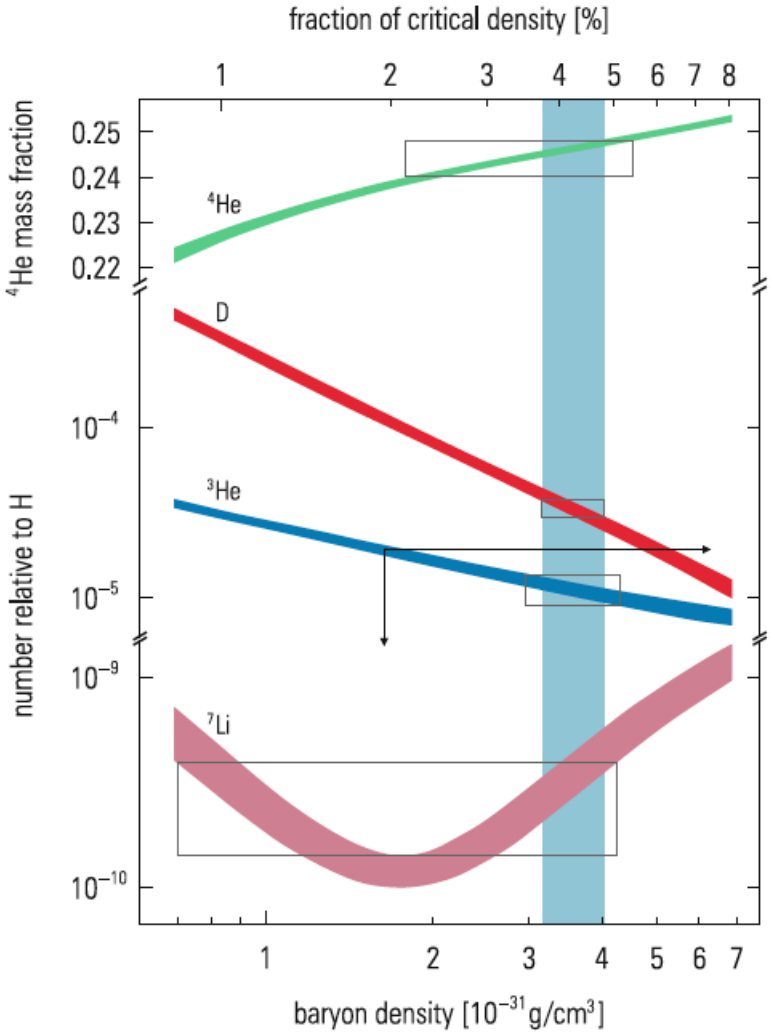

Figure 1.3. The abundances of Helium-4 (green), deuterium (red), Helium-3 (blue) and Lithium-7 (purple) relative to the abundance of Hydrogen, except for Helium-4 which is relative to all baryonic matter mass. These amounts depend on the fraction of the Universe's energy that makes up baryonic matter (top x-axis), corresponding to a total mass density of these baryons in the early Universe (bottom x-axis). The boxes indicate the observed relative abundances, accounting for systematic and statistical errors. Helium-3 has an unconstrained systematic error (arrows). The vertical light blue band is the expected critical density fraction from the Cosmic Microwave Background Measurements. From Reference [25].

formed, the Universe expanded and cooled such that the nuclei could bind electrons into complete atoms during recombination. Simultaneously, the mean free path of light became infinite as it no longer constantly Compton scattered with free electrons. This light from the surface of last scattering still travels the Universe. The continued expansion of space through which these photons traveled has stretched their wavelengths, Doppler shifting them into the microwave region of the electromagnetic spectrum [26]. Measuring this Cosmic Microwave Background hitting Earth from all directions, we can reconstruct the fireball of the young Universe.

The variations in energy of these Cosmic Microwave Background photons over the surface of the reconstructed fireball give insight into energy density fluctuations. Photons easily scattering with baryonic matter have more energy from locations with higher densities of matter. The baryonic matter falls into locations of gravity wells but the radiation pressure forces it back out in a cycle, creating **Baryon Acoustic Oscillations**. These matter density waves rippling across the early Universe are frozen in time in the Cosmic Microwave Background. The Planck Survey observes these ripples with good resolution to small distance scales (large spherical harmonic moments), as seen in Figure 1.4. Reconstructing how the Universe was expanding, the depth of the gravity wells, and the Baryon Acoustic Oscillation dynamics gives a breakdown of the energy of the Universe. The current ΛCDM model of the Universe's energy distribution builds on the Friedmann Equation [27], shown as Equation 1.1. H is the Hubble parameter describing how the expansion velocity of objects depends on their distance from the observer [28]. Using the scale parameter a, $H = \frac{\dot{a}}{a}$, depending on the distance scale and its time derivative (velocity). There is also a scale parameter k determining the curvature of space-time, c is the speed of light, G is Newton's gravitational constant, ρ is the matter density, and Λ is the dark energy-related cosmological constant. Dark energy mysteriously drives the accelerated expansion of the Universe [29].

$$H^2 + \frac{kc^2}{a^2} = \frac{8\pi G}{3}\rho + \frac{\Lambda c^2}{3} \tag{1.1}$$

The curvature k has been measured to be consistent with zero, indicating a flat, infinite Universe that will not expand rapidly forever nor collapse [1], [30]. The Friedmann Equation

can be parameterized by a, with the Hubble constant H_0 of ~70 km/(s Mpc) and in terms of the energy distribution fractions in various components: Ω_c of cold dark matter, Ω_b of baryonic matter, Ω_{rad} of photon radiation and Ω_Λ of dark energy, as shown in Equation 1.2. The equation of state for fluid dark energy requires a dimensionless parameter w depending on the ratio of pressure to energy density.

$$H = H_0\sqrt{(\Omega_c + \Omega_b)a^{-3} + \Omega_{rad}a^{-4} + \Omega_\Lambda a^{-3(1+w)}} \tag{1.2}$$

The negative pressure of expanding dark energy is comparable to its energy density, so $w \sim -1$ and the dark energy fraction term does not depend on the scale parameter a. Compared to the energy in the Universe, the energy in light is negligible. Planck has measured $\Omega_\Lambda = 68.5\%$, which is the fraction of the Universe's energy required to be in Dark Energy to drive expansion. Only $\Omega_b = 4.9\%$ is needed to account for the Baryon Acoustic Oscillations. That leaves $\Omega_c = 26.6\%$ that must be non-interacting mass contributing to the gravity wells, which is dark matter [1]. The Universe's energy density in baryonic matter from the Baryon Acoustic Oscillations in the Cosmic Microwave Background agrees with the estimate from Big Bang Nucleosynthesis, but it adds that there must be roughly five times more mass composing dark matter.

Beyond the Cosmic Microwave Background, the Baryon Acoustic Oscillations remained throughout the evolution of modern **Large Scale Structure**. The dark matter gravity wells maintained their relative positions in the expanding Universe and galaxies formed and clustered nearby. Dark matter is essential for attracting baryonic matter together via gravity to form galaxies and galaxy clusters and the filaments observable in Large Scale Structure. The distance scale for higher density locations in the Cosmic Microwave Background became rings with radii about 150 Mpc that can be used as standard rulers in space [31]. As the Universe developed toward modern day, other traces of dark matter become more evident.

Similar to the work of Kapteyn, Vera Rubin mapped the rotational velocity profiles of several galaxies in the early twentieth century. Strikingly, the **Velocity Curves of Galaxies** flatten at high radii where the reduced number of stars should mean that the velocities drop [32]. The observed mass acting at those radii cannot counteract the inverse

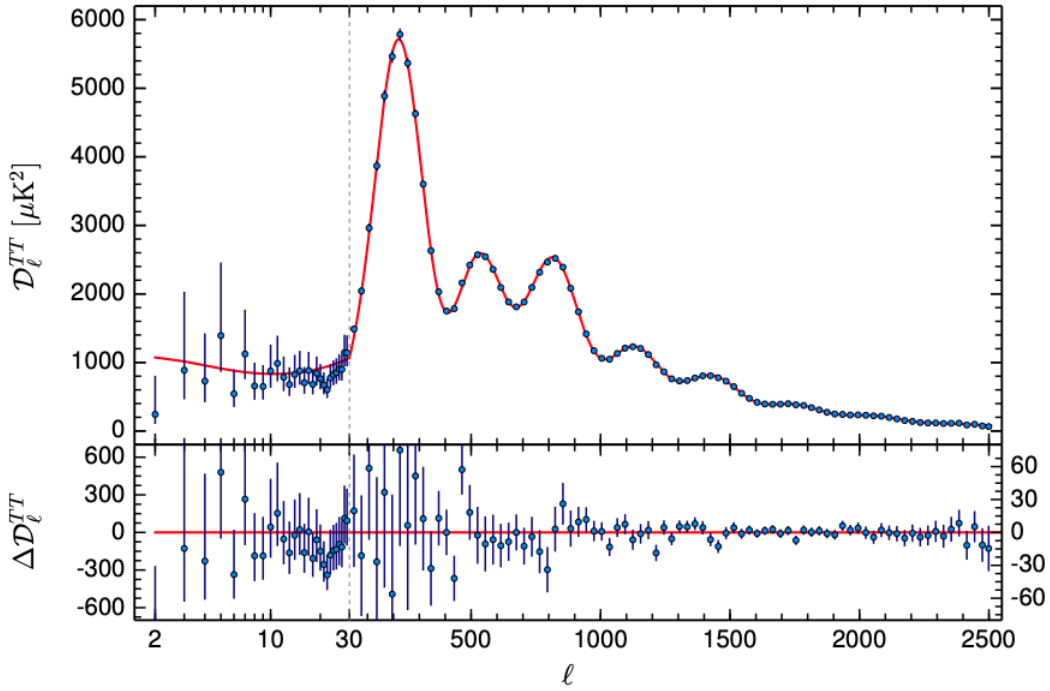

Figure 1.4. The energy distribution of the Cosmic Microwave Background as a function of the spherical harmonic moments, measured by the Planck Survey. Larger moments correspond to smaller details, requiring higher resolution. From Reference [30].

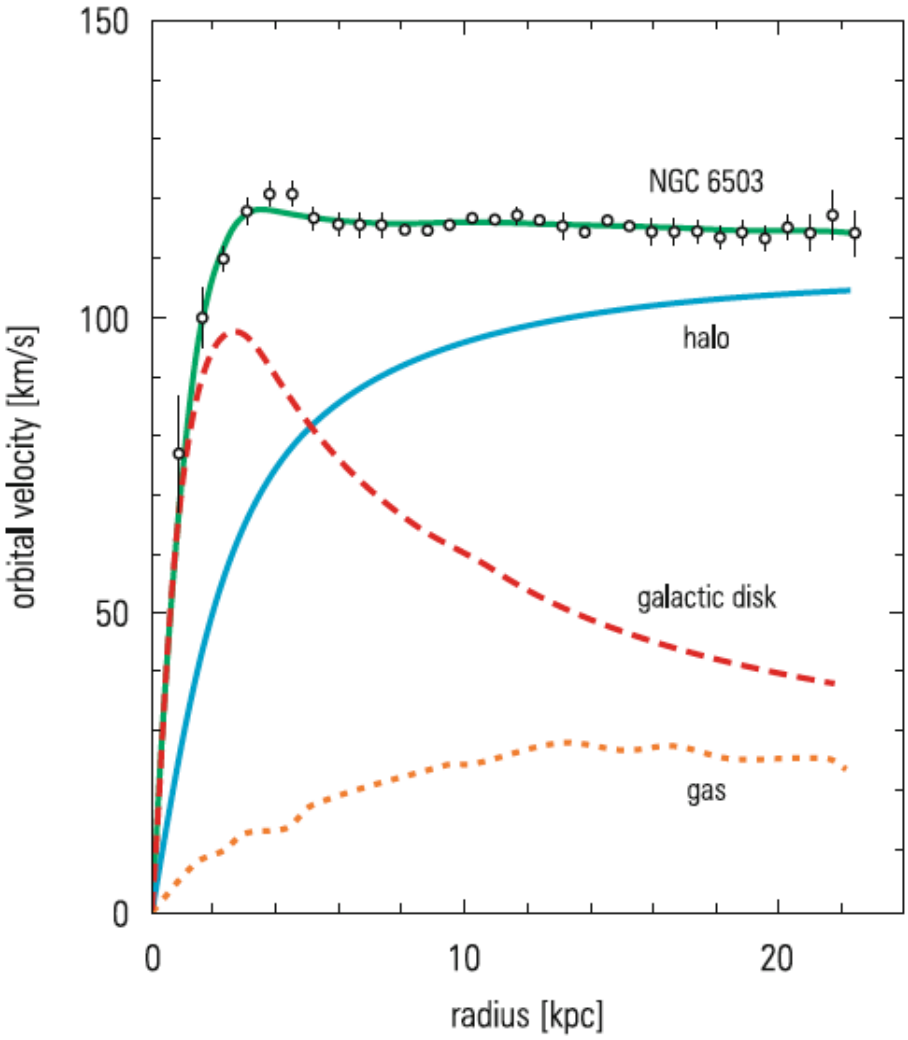

Figure 1.5. The rotational velocity profile of the NGC 6505 galaxy as a function of radius from the spiral galaxy's center (open circles). The green fit is based on the contributions of the galaxy's gas (gold dotted), stars (red dashed), and a significant dark matter halo (blue). From Reference [25].

dependence on radius. Therefore, a significant amount of mass, in the form of dark matter, must extend in a halo to radii beyond the typical locations of luminous baryonic material. Figure 1.5 shows the matter components that are required to produce this flat rotation curve. In fact, a majority of the matter in the galaxy must be in this dark matter halo in order for its gravity to produce these rotational velocities.

The dark matter halo itself is not expected to have a net angular momentum nor be constrained to the galactic disk region. A galaxy's flat rotating disk of baryonic matter is formed through continual magnetohydrodynamic interactions among the baryonic matter [33]. If the dark matter halo is a thermal sphere of dark matter particles, then we would expect to encounter a headwind as we travel with the Sun around the galaxy at 235 km/s. The Earth additionally circles the Sun at about 30 km/s. Therefore, we predict an **Annual Modulation** of dark matter particles passing through the Earth as we move faster into the halo to pass the Sun in June, and slower through the halo to circle behind the Sun in December [34].

Scaling up to galaxy clusters, over a quarter of a century before Vera Rubin, Fritz Zwicki used the **Virial Theorem** on the Coma Cluster to determine that there must be more mass than expected just from observed baryonic matter [35]. The Virial Theorem, Equation 1.3, defines a stable bound system as one where the amount of potential energy, U is twice the amount of kinetic energy, T.

$$U + 2T = 0 \tag{1.3}$$

$$-G\frac{Mm}{r} + 2(\frac{1}{2}mv^2) = 0 \tag{1.4}$$

$$v^2 = G\frac{M}{r} \tag{1.5}$$

For two gravitationally bound objects of masses M and m, the velocity, v, of the object with mass, m, directly depends on the mass, M, exerting the force of gravity. To attain the observed velocities of the galaxies in the Coma Cluster, there needed to be significantly more mass than was visible, of which a large amount was distributed outside the point-like galaxy locations themselves.

Gravitational effects of dark matter in galaxy clusters also include **Gravitational Lensing** distortions of more distant galaxies behind the galaxy cluster in the foreground. Einstein's general relativity predicts that mass distorts space-time, causing the shortest path between two points in space to follow a curve around a massive object. Therefore, an object directly behind a massive foreground object can still be seen as its light curves around the

massive object and to our telescopes. The background object's image appears smeared and sometimes in multiple locations around the massive foreground object. Strong gravitational lensing can be obvious on images, such as produced by the Hubble Space Telescope, and form Einstein Rings. Microlensing requires special spectroscopic instruments to pick out gravitational lensing effects.

The **Bullet Cluster** is an example where gravitational microlensing exposed a dark matter distribution very different from the observed locations of baryonic matter. The various distributions of the different forms of matter can be seen in Figure 1.6. Two galaxy clusters collided, and the galaxies (point-like objects at this scale) were unaffected. The intergalactic medium of each cluster, however, was affected. One galaxy cluster's intergalactic gas collided with the other, creating a bow shock according to magnetohydrodynamics. The clear image of the shock gives the Bullet Cluster its name. The mass density profile required for the observed gravitational microlensing reveals that most of the mass should exist in two distinct locations, not the middle where most of the intergalactic medium is. This indicates that a majority of the mass in the colliding galaxy clusters passed through without interacting to remain distinct centers of mass separate from the locations of most of the baryonic matter [36]. Again, dark matter, which does not appear to interact electromagnetically, must make up a majority of the mass in this part of the Universe to account for gravitational observations that baryonic matter cannot explain.

From these observations, dark matter must constitute most of the mass of the Universe. It appears throughout all time and on a wide range of distance scales through its gravitational effects. It does not seem to interact with anything except through gravity. It passed through itself in the Bullet cluster, and does not reflect or produce any noticeable light. Even before the the Cosmic Microwave Background was formed, when light was constantly interacting with the baryons, the dark matter appeared unaffected by significant radiation pressures. With these constraints, what attributes could a dark matter particle have?

Figure 1.6. The Bullet Cluster. Galaxies can be seen as points of light. Most of the baryonic matter in the cluster is in the intergalactic medium, which glows with X-rays and is here seen in pink. Gravitational microlensing surveys of background objects require that most of the mass be distributed according to the density contour lines, and centered on the locations highlighted here in blue. A combination of images from References [25], [36].

1.2.2 Select Dark Matter Models

Generous mass limits on the fundamental unit of dark matter "constrain" it to nearly 90 orders of magnitude. The smallest structures containing dark matter are dwarf galaxies. The escape velocity from a dwarf galaxy of ten million solar masses with a radius of a kiloparsec is less than 10 km/s. Therefore, dark matter needs to be non-relativistic and "cold" to avoid evaporating away from these galaxies. Ultimately, the dark matter particle mass m must be greater than 10^{-57} kg for the de Broglie wavelength $\lambda = 1$ kpc to fit in the dwarf galaxy at this velocity (according to Equation 1.6). In more reasonable particle physics units of rest mass energy, this lower bound on dark matter's particle mass is about 10^{-22} eV/c^2, and we would look for macroscopic effects from a dark matter field rather than from individual particles. A more careful analysis of the satellite dwarf galaxies around the Milky Way by the Dark Energy Survey sets the lower mass limit at 10^{-21} eV/c^2 [37].

$$m = \frac{h}{\lambda v} \tag{1.6}$$

At the other end of the mass spectrum, dark matter might be **Massive Compact Halo Objects** (MACHOS) up to a few tens of solar masses, 10^{67} eV/c^2. The gravitational effects of anything larger, particularly in binaries, would be obvious to microlensing surveys [38]. At the smallest masses, the number density of dark matter particles to compose the observed mass density profile require them to be bosons. The Pauli Exclusion principle doesn't allow for dark matter to be fermionic unless the particles have a mass above $\mathcal{O}(10)$ eV/c^2 [39]. The Planck Mass, $\sqrt{\frac{\hbar c}{G}} = 10^{19}$ GeV/c^2, gives a natural upper limit on allowed particle mass. Dark matter candidates with masses above this would be composites of other particles. By making certain particle assumptions, the most interesting mass range may be much smaller [40]. However, with such limited information regarding dark matter's attributes, it is important to pursue experiments that could rule out any allowable dark matter parameter space.

An example composite candidate would be **Primordial Black Holes**. Over-dense regions of standard model particles in the earliest Universe (before primordial atomic abundances were frozen out from Big Bang Nucleosynthesis) could have collapsed into black holes,

which could still exist today despite Hawking Radiation [41]. In this case, we do not expect any new particles for the Standard Model. However, microlensing studies find that MACHOs (which include any dim objects composed of baryonic matter from brown dwarfs to black holes) cannot account for all the dark matter mass in the Universe [42].

The most promising dark matter candidates include **Axions** and **Weakly Interacting Massive Particles** (WIMPs). Axions would be bosons, while WIMPs would be fermions around 100 GeV/c^2. Axions, sometimes specified as QCD Axions, were proposed to solve the Strong CP Problem, but could also be dark matter candidates. WIMPs are particularly motivated by the WIMP Miracle.

When looking at symmetries and conserved quantum numbers in particle interactions, decays via the Weak Force do not necessarily conserve charge conjugation (C) and parity (P). The decays of neutral K [43] and B [44] mesons via the Weak Force do not behave symmetrically when the particles are exchanged with their anti-particles (charge conjugation) and after switching spatial directions (parity). This CP violation in Weak decays indicates matter and anti-matter are not simply mirror images of each other with different charges. However, the mathematical framework for the Strong Force with quarks and gluons is analogous, and there is no observed CP violation in the Strong Force. An example of the suppression of the CP violating term is the electric dipole moment of the neutron. With three constituent charged quarks, the neutron electric dipole moment is consistent with zero. The inexplicable lack of CP violation is known as the Strong CP Problem [25].

Axions are proposed bosons existing in a field that couple to quarks and gluons to suppress CP violation in the Strong Force [45]. Named after a popular soap brand, they "clean up" the Strong CP Problem [46]. Their potential interactions with photons, leptons, and baryons can be sufficiently small to constitute dark matter. Axion-like particles could also be dark matter, and interact similarly to QCD Axions without being particles that solve the Strong CP Problem.

Separate from bosonic Axions permeating space in a field, there are proposed fermionic WIMPs drifting in the Universe. There may have been a time (long before light decoupled from baryonic matter to create the Cosmic Microwave Background) when dark matter and baryonic matter were coupled in thermal equilibrium. Baryons would have annihilated

into dark matter and vice versa until the Universe expanded and cooled to a point where the interactions were extremely rare. Then, the relative abundances of dark matter and baryonic matter would have been frozen out. With those known relative abundances and considering the thermodynamics of this expansion period dominated by radiation, certain values for WIMP dark matter fall out. Thermalized WIMPs with $\mathcal{O}(100)$ GeV/c^2 mass can create the observed relic densities if their velocity-dependent annihilation cross-section is $\langle \sigma v \rangle \sim 10^{-26}$ cm^3/s. [23]. Such a cross-section is remarkably similar to cross-sections characteristic of the Weak Force, and the mass is reasonable for particles proposed by **Supersymmmetry**. These values for WIMPs, and how they tie into Supersymmetry is known as the WIMP miracle [47]. More generally, WIMP candidates encompass a wide range of potential fermionic particle masses, and interaction mechanisms other than through the Weak Force, indicating a potential new force.

Another possible dark matter candidate is a **Sterile Neutrino**. Neutrinos have all the characteristics of dark matter, except that they are relativistic, as observed through their participation in Weak Force interactions. The number of relativistic neutrino species N_{eff} has been measured with high precision to be limited to the three known mass states of neutrinos [1]. A sterile neutrino would require a fourth flavor and mass state. However, the sterile neutrino mass state would be much heavier than the other known mass states, making it extremely unlikely to be produced with an electron, muon or tau flavor. Similarly, the lighter mass states would not frequently oscillate into the fourth flavor. From a detection standpoint, sterile neutrinos would be evident if there is a component of the neutrino flux conspicuously absent. This is akin to the solar neutrino problem, but would not be solved with flavor-independent Weak interactions, which would still fail to detect the sterile flavor. Otherwise, sterile neutrinos could be categorized as a light WIMP candidate if they additionally interact or decay through new physics.

1.3 Liquid Xenon Time Projection Chambers

XENON DETECTORS - An Acrostic Sonnet

Xenon, the target in our TPC,
Encounters dark matter that's floating past.
Nucleus, hit! Behold the S1 fast!
Other atoms set some electrons free.

Now these electrons we will surely see
Drifted up to the gas through which they blast.
Electrons create an S2 at last!
Though, if not dark matter, what could it be?

Events caused by beta decays also
Create an S1 and an S2, too.
Though the needed S1-S2 ratio
Of nuclear recoils has less S2.
Regardless of neutron or neutrino,
Search we must for any dark matter clue!

With WIMPs so well-motivated by the WIMP miracle, they could be directly detected interacting weakly with a target of well-understood baryonic matter. The aftermath of such collisions with atoms, via the Weak Force or any new physics, can be observed and forensically reconstructed to learn about the dark matter particle. An ideal target atom would be about the same mass as the expected WIMP. Too massive of a target would not appear to be hit. Too light of a target would not be able to usefully constrain the dark matter particle's mass. For a $\mathcal{O}(100)$ GeV/c^2 WIMP expected to coherently scatter with a nucleus, xenon–with an atomic mass of 131 GeV/c^2–is a good choice.

Other characteristics of xenon are also particularly advantageous. It is a noble element and does not chemically react with other elements, allowing for low background interaction rates and easy purification techniques. Its primary isotopes are either completely stable, or nearly so with half-lives comparable to the age of the Universe, thus reducing intrinsic radioactive decay backgrounds. As a liquid, it is dense and impurities diffuse through it very slowly. Liquid xenon in bulk will self-shield, allowing analyses to choose a central, ultra-pure fiducial volume that avoids contamination from the surrounding materials used to build the

detector chamber. Attaining a liquid state is easy near atmospheric pressure at only 180K (-93°C), so most equipment made for room-temperature applications still works, and refrigeration technology is commercially available. The final attribute of xenon that makes it a perfect dark matter detection target is its ability to scintillate. Particle interactions exciting xenon will create light signals, photons with 178 nm wavelengths, and that ultraviolet scintillation light is easily detected with photosensors [48].

The mechanism of scintillation in xenon can occur in two ways: a singlet or a triplet case. The singlet case proceeds as in Equation 1.7, and the triplet case proceeds as in Equation 1.8.

$$Xe^{*} + Xe \rightarrow Xe_2^{*} \rightarrow Xe + Xe + \gamma \tag{1.7}$$

$$Xe^{+} + Xe + e^{-} \rightarrow Xe_2^{+} + e^{-} \rightarrow Xe^{**} + Xe \rightarrow Xe_2^{*} + E_{heat} \rightarrow Xe + Xe + E_{heat} + \gamma \tag{1.8}$$

In the final step of both, an excited xenon atom (denoted with a *) will be slightly polarized, loosely attaching to another nearby xenon atom. The de-excitation photon γ released is not a characteristic energy transition of monatomic xenon. The bulk liquid xenon is therefore transparent to the scintillation photon and it is unlikely to be re-absorbed, making it detectable [49]. In xenon, the time scales are comparable, so the two processes cannot easily be distinguished.

To measure these scintillation photons and ionization electrons created by particles energetically interacting with xenon, the world-leading technology is a liquid xenon Time Projection Chamber (TPC) [2]. The concept is illustrated in Figure 1.7. A weakly interacting dark matter particle is expected to scatter elastically with a xenon nucleus once while passing through the detector. The recoiling nucleus collides with other xenon atoms in its path, exciting them. Some atoms de-excite and emit scintillation light. An electric field, E_{drift}, between the Cathode at the bottom of the TPC and the Gate electrode just below the liquid surface is applied to the target. This electric field ionizes the rest of the excited atoms, and drifts their ionization electrons toward the gas. A stronger field, $E_{extraction}$, between the Gate and the Anode in the gas, pulls the electrons out of the liquid to scatter with gaseous xenon. Thus, there is a second signal of scintillation photons, proportional to the number of

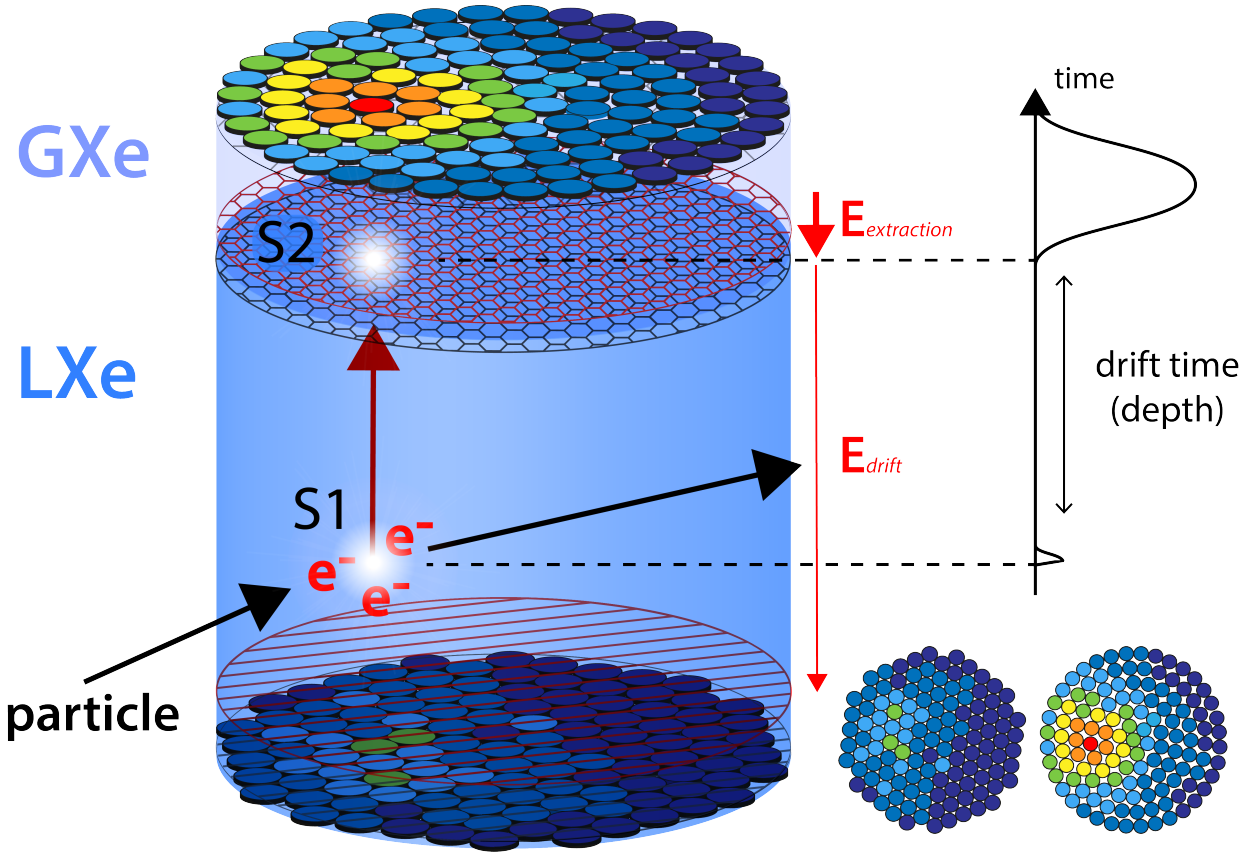

Figure 1.7. A schematic of the XENON1T dual-phase liquid xenon Time Projection Chamber (TPC). A particle enters the liquid xenon and scatters once on a nucleus before exiting. The recoiling nucleus deposits the interaction energy to nearby atoms. Some scintillate, others lose their excited electrons, which drift upward and are extracted into the gas. The PMT arrays record initial scintillation light, S1, and secondary scintillation light proportional to the number of freed electrons, S2. Image Credit: Lutz Althüser.

extracted electrons. Arrays of photomultiplier tubes (PMTs) on the top and bottom of the TPC record the light signals from the initial scintillation (S1) and delayed scintillation from the ionization electrons (S2).

The hit pattern of the S2's photons on the PMT arrays gives the horizontal (x and y) coordinates of the interaction. The drift velocity of electrons in liquid xenon is constant in a uniform electric field. For XENON1T with $E_{drift} = 0.125$ kV/cm, the drift speed is 1.44 mm/μs [50]. Therefore, the time difference between the S1 and S2 projects how deep (z coordinate) in the detector the interaction happened. The kinematics of the dark matter

interaction determine how much energy was deposited, which determines the number of excited atoms. The total energy transferred in the collision can be calculated from the S1 and S2 light signals.

The energy reconstruction requires Equation 1.9, where E is the energy deposited by the interaction in the xenon and $W = 13.7$ eV is the excitation energy. The factor g_1 is dependent on the detector efficiencies to translate detected light to number of atoms that scintillated. The factor g_2 likewise translates the detected light to number of ionization electrons produced. Both g_1 and g_2 can be determined from mono-energetic calibration sources. Typically, g_1 is $\mathcal{O}(0.1)$ PE/γ due to low light detection efficiency, and g_2 can be $\mathcal{O}(10-100)$ PE/e^- for bright electron signals and good efficiency transporting them to the amplification region.

$$E = W\left(\frac{S1}{g_1} + \frac{S2}{g_2}\right) \tag{1.9}$$

While de-excitation occurs on timescales of $\mathcal{O}(10)$ ns, regardless of through the singlet or triplet states for xenon, electrons passing through the amplification region cause scintillation along their paths that can last $\mathcal{O}(1)$ μs. Due to detector efficiencies, the lowest-energy interaction clearly detectable in a liquid xenon TPC would cause a single-electron ionization signal, requiring ~15 eV [51], [52] for electronic recoils and ~250 eV [53] for nuclear recoils after considering heat loss and relative probabilities for recombination. Electrons give large signals and are detectable with high efficiency [54]–[60]. I spent the most time of my doctoral work exploring these single-electron S2s, as presented in Chapter 4.

The observation of an S1 followed by an S2 constitutes a clear, typical event indicative of a particle interaction. Studying the relative properties of the S1 and S2 signals in an event reveal a wealth of information about the progenitor particle interaction.

1.3.1 Particle Interactions in these TPCs

Events will be recorded whether an external particle scattered with a xenon nucleus, known as a nuclear recoil (NR), or with an electron of a xenon atom, resulting in an electronic recoil (ER). Radioactive impurities in and around the xenon also produce observable events.

Gammas from relaxing meta-stable nuclei Compton scatter with electrons, appearing as ER backgrounds. Higher energy gammas can multi-scatter, resulting in events where the S1s occur simultaneously from the gamma traveling at the speed of light, but multiple S2s can appear depending on the depths of different interaction vertices. Beta decays eject electrons into the xenon from certain radioactive impurities, appearing as ER events, too. An alpha decay is the ejection of a Helium-4 nucleus (alpha particle) from a larger unstable nucleus, which appears more like an NR background but is monoenergetic. A detector's reaction to NR and ER events can be calibrated with known sources. WIMP NR events are expected to resemble neutrons, which elastically scatter with xenon nuclei through the Weak Force, mediated by a Z boson.

In a nuclear recoil, the much heavier xenon nucleus deposits its kinetic energy from the interaction along a shorter recoil path. With a higher density of excited xenon atoms, ionization electrons are more likely to recombine, producing more scintillation overall, especially through the triplet state. This leaves a smaller number of ionization electrons in the S2 compared to the produced scintillation photons in the S1. Also, the process is less efficient, and a larger fraction of the interaction energy is dissipated in heat, requiring higher energy depositions to be detectable. The limited light collection of photosensors and detector geometry make S1s less detectable in general. In an electronic recoil, the electron travels farther, so excited atoms are more spaced out. Fewer atoms de-excite, and they favor the singlet state. Thus, ERs typically have relatively more electrons in the S2 than photons in the S1, are more efficient with less lost heat, and more detectable for lower energy depositions.

Figure 1.8 shows the S2 vs S1 parameter space for ERs and NRs in XENON1T [61]. Radon-220 is dissolved in the xenon, and its Lead-212 daughters beta decay to produce signature ERs. After several hours, the source decays to stable Lead-208, essentially disappearing. An Americium-241 alpha source combined with Beryllium-9 (an AmBe source) will produce neutrons as Beryllium nuclei absorb decaying Americium-241's alpha particles and transmute into Carbon-12 with a neutron left over. Since neutrons are neutral particles interacting weakly, the AmBe source can be temporarily mounted outside the detector and the neutrons will pass into the xenon target.

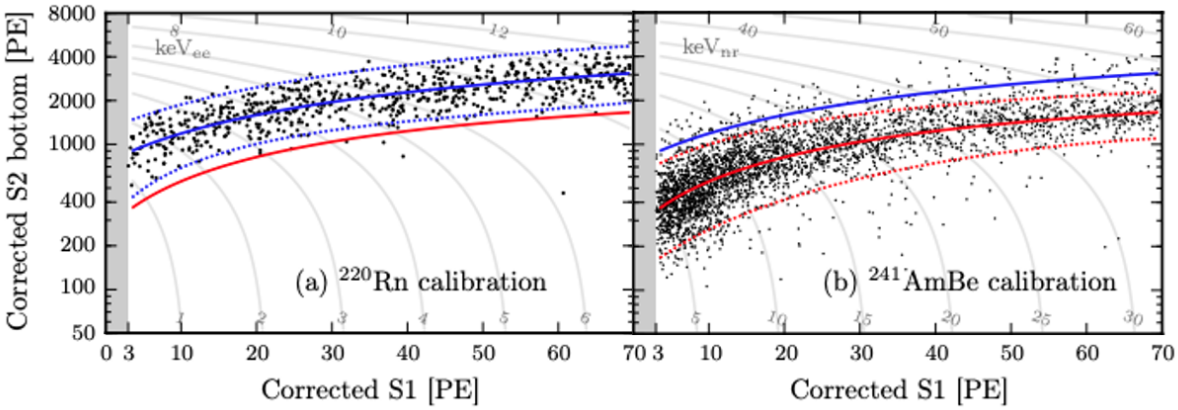

Figure 1.8. The S2 vs S1 ratio for two main calibration sources in XENON1T. (a) ER calibration of Lead-212 beta decay events from the Radon-220 decay chain. (b) NR calibration of elastically scattering neutrons from an Americium-241 Beryllium-9 neutron source. The median ratio for ERs is the blue solid line, the median ratio for NRs is along the red solid line. In the respective calibration plots, the $\pm 2\sigma$ band is denoted with dotted lines. From Reference [61].

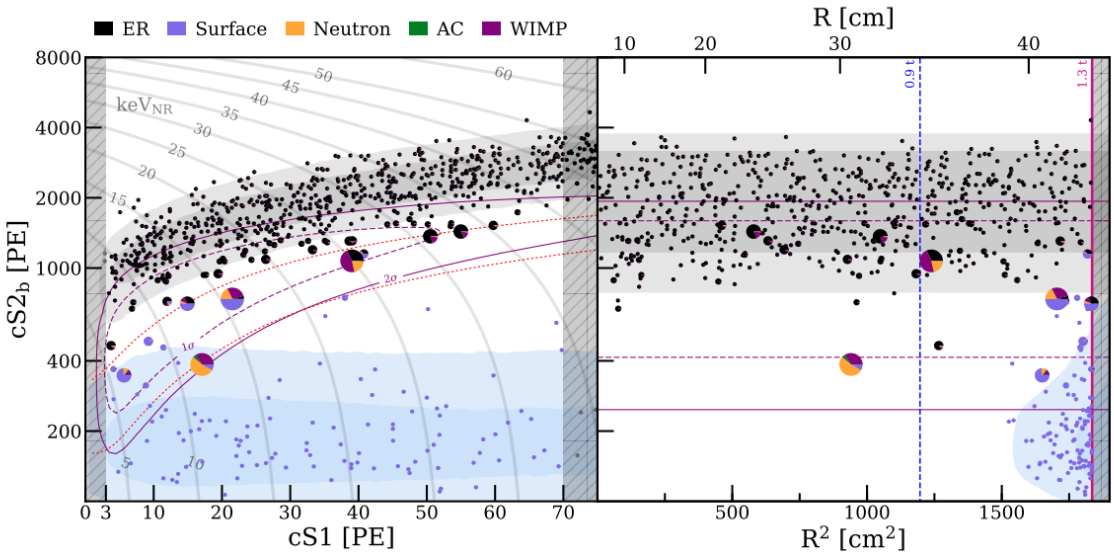

Figure 1.9. The events in XENON1T during its one ton·year exposure. Candidate WIMP events are the pie charts showing the probabilities for signal and background models. The expected CEvNS rate was negligible and not even considered. From Reference [2].

For a standard WIMP search looking for NRs due to WIMPs elastically scattering with xenon nuclei, there are nearly no expected backgrounds. Relativistic neutrinos interacting via CEvNS are one. The only known natural neutrinos with a sufficient combination of energy and flux are solar Boron-8 neutrinos, as from Figure 1.2. However, this interaction has not yet been measured despite our best efforts [62]. Other backgrounds could be stray neutrons, but detector effects give larger backgrounds. Misreconstructed events of an unrelated S1 and S2 accidentally coincident in the detector depend strongly on lone S2 rates, which are high. Events near the walls can have a lower S2 efficiency that makes them appear more NR-like. The largest low-energy background events are ERs from Lead-214 beta decays, a daughter of Radon-222 and Uranium-238, which is in all materials. The sheer number of Lead-214 events statistically produce some interactions with S1-S2 ratios that are more NR-like. Figure 1.9 shows the WIMP candidate events for XENON1T's one ton·year exposure based on background models and an example signal model of 200 GeV/c^2 WIMPs interacting elastically and having a spin-independent cross-section of $\sigma_{SI} = 4.7 \cdot 10^{-47}$ cm^2 [2].

Axions are expected to couple to electrons, producing ERs. While most dark matter cannot be relativistic, QCD Axions may be produced in the sun with larger, more detectable energies. A 3.4σ excess of low-energy ERs was found in XENON1T [63]. However, the Axion fit values are in tension with other experimental constraints, and we could not rule out that XENON1T might have been contaminated with tritium, which has a beta decay spectrum in that energy region.

Beyond looking for NRs from WIMPs and ERs from Axions, some looser constraints can be made on those dark matter models and more by looking at total event rates. The rates would be agnostic to ER or NR classification, but are particularly powerful for low-energy interactions. Since the S1 detection efficiency is a limiting factor to lower energy interactions, it can be ignored and we can conduct an S2-only search [64]. Our understanding of the backgrounds and detector response to interactions down to single-electron S2s is not great [65], so I strove to improve [66] as recounted in Chapter 4.

1.4 Conclusion to the Introduction

Through this wealth of interrelated information, I found a few places to explore and contribute. Radon-222, daughters of ubiquitous Uranium-238 lead to Lead-214 beta decays that smudge into our search for WIMPs, but they have to happen in between the identifiable, characteristic decays of their parent and daughter nuclei. Background neutrons could be related to muons from cosmic ray showers in the atmosphere reaching the detector and impacting nuclei in the immediate surroundings. Dark Matter particle masses could be as large as the Planck mass, but we haven't really looked for them in a xenon TPC. Accidental coincidence backgrounds and poor limits by S2-only searches are impacted by a high rate of lone-S2s, so can that rate be reduced through detector design and analysis? Lastly, we could be the first to detect CEvNS of Boron-8 solar neutrinos, but most events are very low energy and we need an S1 and S2 to confirm that they are NRs. So how could we explore these low-energy events, and is it practical? In the next chapters, I will present my work into all of these topics, with special consideration to the last two, through which I became an expert in few-electron signals in liquid xenon dark matter detectors.

2. THE BIG SPHERE RADON VETO AND MENTORING UNDERGRADUATES

A Purdue Teaching Assistant - a Limerick

There once was a TA at Purdue
teaching undergrads all that she knew.
She gave them some data,
and code (still in beta);
Experience for them, and her, too.

When starting in an unfamiliar field, it is important to begin with the basics. Coming into graduate school, my only coding experience was with LabView (more on LabView in Section 3.1). In this chapter, I describe my first research project with the Dark Matter Group at Purdue, and other projects I conducted with undergraduates at a similar level. After handing off the Radon Veto to fellow graduate student Juehang Qin, we looked for signs of rare but multiply interacting massive dark matter particles near to the Planck Mass ($\lesssim 10^{19}$ GeV/c^2). When this project was taken over by Postdoctoral Researcher Dr. Michael Clark, we looked for rare events directly caused by cosmic ray muons. While most of my time was dedicated to the content of the rest of this Thesis, the portion I spent on these projects and their first-time researchers was not insignificant.

The XENON data used by undergraduates is stored on Data Depot at Purdue University [67], with a hosted network-accessible JupyterHub [68] anchored on a dedicated computer named Bothe. By remotely accessing Bothe, we performed analyses in Jupyter Notebooks using Python, and our Notebooks were available to other group members for facilitated collaboration and code sharing. We used a subset of the total XENON1T data, which is hosted by the University of Chicago's Midway Clusters [69]. As a graduate student in XENON, I was able to access Midway to load data, make initial rough cuts, and transfer it to Data Depot where it is accessible on Bothe. Without the credentials to access Midway, undergraduates performed research projects on the data sets we (the graduate students) transferred. It was also overall easier to perform analyses on Bothe since its JupyterHub was easier to access than launching a JupyterLab session in a job on Midway.

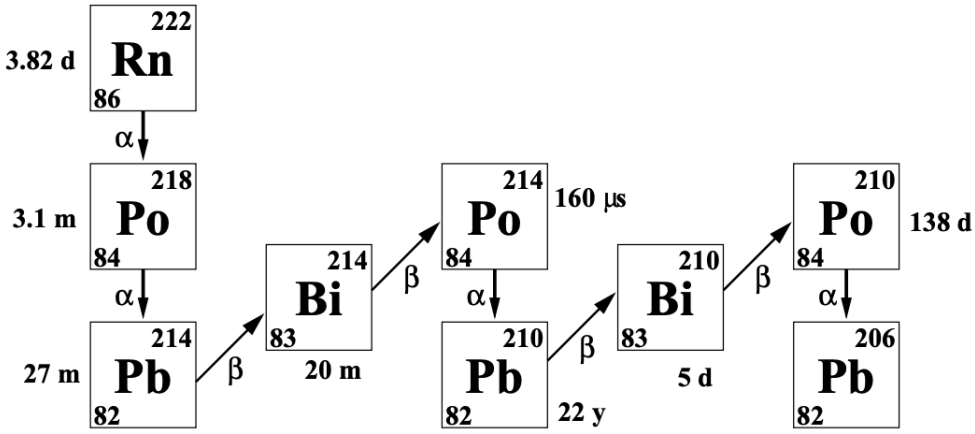

Figure 2.1. The Radon-222 decay chain to stable Lead-206. From Reference [70].

2.1 The Big Sphere Radon Veto

As evidenced by Figure 1.9, a majority of low-energy particle interactions in the currently world-leading liquid xenon TPC, XENON1T, are ERs. Nearly all of these are Lead-214 beta decays from the Radon-222 decay chain [63], which is shown in Figure 2.1. Trace amounts of Uranium-238 in all materials slowly decays to Radon-222. Then this radioactive decay chain becomes a problem for liquid xenon TPCs.

Being another noble element, radon easily mixes with the xenon, diffusing throughout the TPC's volume within its half-life of nearly four days. Normal purification methods, a hot zirconium getter, do not work on noble, inert elements. When Radon-222 does alpha decay to Polonium-218, the three minute half-life of Polonium-218 means that another alpha decay will soon follow to create Lead-214. Lead-214 lives longer, undergoing the problematic beta decay to Bismuth-214 which, in turn, has a similar half-life of nearly half an hour. Once the Bismuth does decay, Polonium-214 is so short-lived that its NR-like alpha decay appears with the Bismuth-214 beta's ER signature in a combined event, known as a BiPo. The population of BiPos is unique and identifiable. Polonium-218 alpha decays are monoenergetic, and also unique and identifiable. Somewhere in the meantime must be a Lead-214 beta decay that cannot be dark matter.

Starting this analysis in the summer of 2017, I worked together with Ryan Kim, a talented visiting student undertaking an NSF-funded Research Experience for Undergraduates. We also had support from veteran graduate student Darryl Masson. We explored a few months of XENON1T data from its primary dark matter search science run [2]. For the Radon Veto to tag Lead-214 beta decays between Polonium-218 alpha decays and BiPos, we needed to understand how individual atoms moved in the liquid xenon. XENON100 saw a central cell of significant convection in the liquid [71]. Therefore, we wanted to know how far the atoms could have drifted before decaying and proceeded to characterize convection in XENON1T. We exploited the relatively short three-minute half-life of Polonium-218 to match Radon-222 parent alpha decays with the daughter Polonium-218 alpha decays. We matched all Radon-222 events to all Polonium-218 events that occurred within three Polonium-218 half-lives of each other. A clear band of correct matches is evident in Figure 2.2, corresponding to a convection velocity of 0.3 cm/s.

The Big Sphere Radon Veto was mostly convection-agnostic and did not use the directional information of the convection cell. We could start at the Polonium-218 alpha decay and expand a veto sphere outward with time according to the 0.3 cm/s speed until we found a low energy event, or until we reached a point where we were vetoing more of the detector volume than was reasonable for a cut in this background contribution. We maximized the fraction of Lead-214 that would have decayed in that time relative to the fraction of the total detector used for that veto volume and found the maximum radius to be $\sim$13 cm. Looking forward in time from the Polonium-218, we observed twice as many (17 events) low energy events than we expected simulating random locations in the TPC at random times and searching for low energy events (8 events).

There are more Polonium-218 decays than BiPos, which could be for two reasons. For BiPos, identifying correctly-matched pile-up events of a Bismuth-214 beta decay and a Polonium-214 alpha is less efficient than just looking for Polonium-218 alphas. Also, they can just disappear when metallic Lead-214 or Bismuth-214 plates onto the electrodes (particularly the negatively charged Cathode), or attaches to the walls, or diffuses out of the TPC. Events at and below the Cathode do not necessarily produce an S2 due to the electrons being drifted down in these regions to never reach the amplification region. Events at the

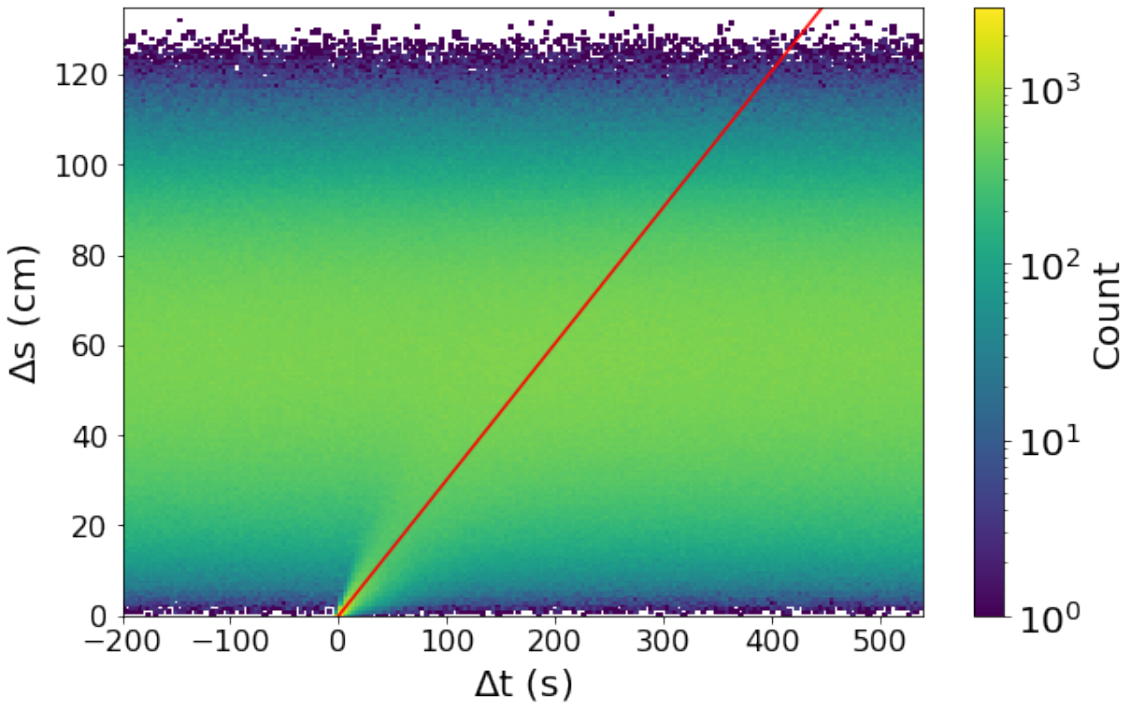

Figure 2.2. All possible matches of Polonium-218 and Radon-222 events that occur within three Polonium-218 half-lives of each other. For the correct matches, the Polonium-218 events happened after the Radon-222, and there is a visible band for small Δs and Δt values with a mean velocity of 0.3 cm/s, indicated by the red line.

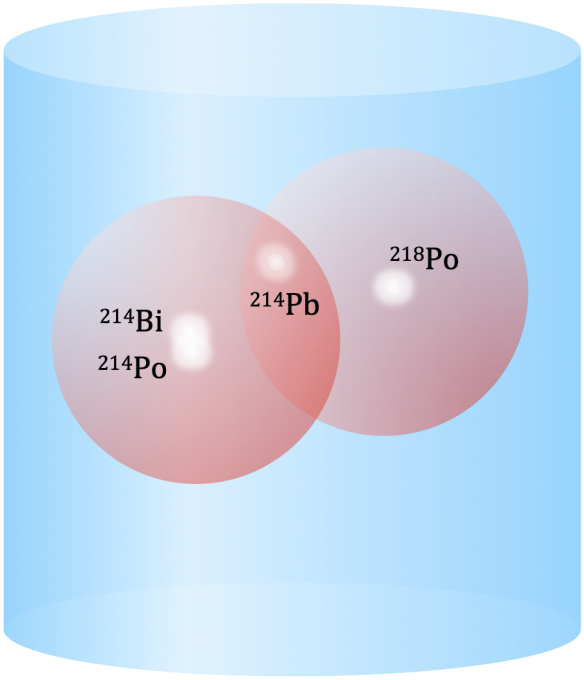

Figure 2.3. Rendition of the Big Sphere Radon Veto finding a Lead-214 event by both looking forward in time from the Polonium-218 decay and backwards from the BiPo.

walls can also lose their S2 electrons if they are captured on the wall materials. Therefore we chose to look forward in time from the Polonium-218 to not miss Lead-214 events that did not have a BiPo. Later, our thinking changed.

The Lead-214 half-life is longer than the Bismuth-218 half-life, so looking backwards from the BiPo can be more efficient for finding more Lead-214 decays in a smaller sphere. There are fewer veto volumes, and an observed BiPo is more likely to have a Lead-214 parent that is also observable. Additionally, this direction helps save computing time with fewer Big Spheres to search. We could have made the veto stricter by requiring a Lead-214 event to be connected to both a Polonium-214 and a BiPo, as shown in Figure 2.3. However, the veto volumes become larger while the probability of finding events decreases. We should be able to follow the convection vector field, reconstructed from Radon-222 and Polonium-218 pairs in Figure 2.2, with a smaller total veto volume for a longer time.

At the end of the summer, Ryan Kim left and I returned my focus to my classes and teaching introductory physics laboratory sections. A dozen undergraduates continued various aspects of the Radon Veto throughout the year, particularly toward identifying correct Radon-222 and Polonium-218 pairs and constructing a good convection vector field from Figure 2.2. A few tried to simulate the observed convection cell with ANSYS Fluent [72], of which I learned a thing or two. Darryl, who was working on the Purdue small-scale TPC, was preparing to graduate, so I learned to take over that project, detailed in Chapters 3 and 4. By the summer of 2018, Juehang Qin joined the group as a new graduate student, and he took over the Radon Veto project, which is now almost done and able to track the decay chain of a single Radon-222 atom around an accurate convection vector field.

2.2 Planck Mass Dark Matter

In the Fall of 2018, there were nearly a score of Purdue Undergraduates interested in gaining research experience for course credit with our group. The Radon veto was running out of tasks for first-time researchers, so we started exploring dark matter particles up to the Planck Mass. A recent paper had proposed Multiply Interacting Massive Particles (MIMPs) that would be too few for previous experiments to have found but so massive and with such a large cross section that they would scatter multiple times passing through the detector [73]. These multi-scatter events should leave traceable tracks.

Dark matter travels roughly 220 km/s with respect to the Earth as we move with the Sun around the Milky Way Galaxy. A MIMP taking about 4 μs to traverse the XENON1T detector could interact so much that the individual S1s of each interaction site would overlap in time. The resulting merged S1s would look more S2-like, which we denoted $\tilde{S}$. The signature would be like nothing we had seen, except for muons ploughing through the detector. An example muon track is in Figure 2.4.

Muons are relativistic and would not have an $\tilde{S}$. They are also charged, and XENON1T has an instrumented water tank surrounding the TPC to look for the Cherenkov light of charged muons traveling faster than the speed of light in water. We could know when a muon track passed through the TPC based on the water tank's muon veto trigger.

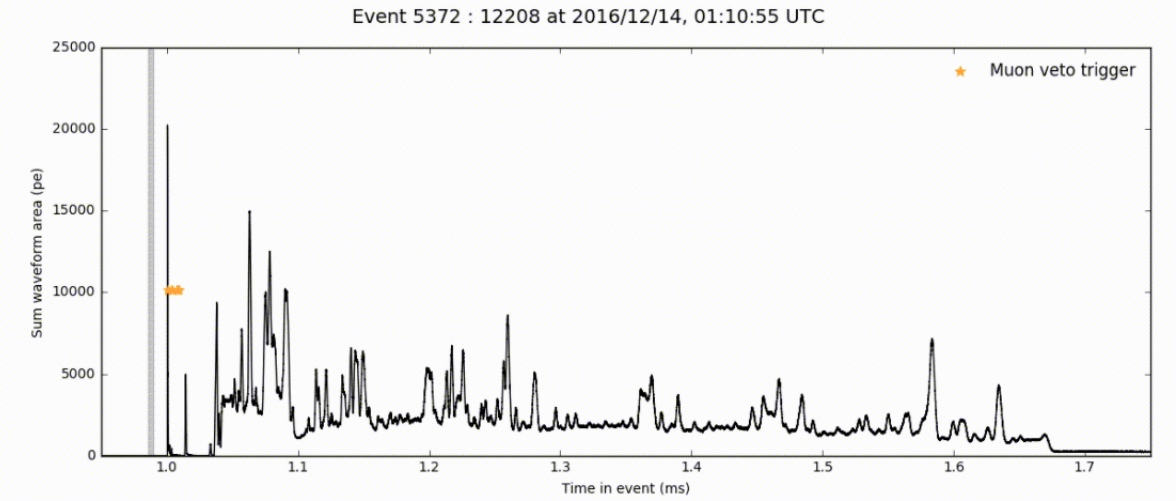

Figure 2.4. An example waveform of a muon track passing through the XENON1T detector. Image Credit: Jelle Aalbers.

Similar to muons, a track's S2 could be a few microseconds long if it was horizontal and all interaction site S2s were measured at the same time. If the track was vertical through the detector, the S2s could pile up to be nearly a millisecond long, spanning the full drift time range of the detector. Tracks passing vertically between the gas and liquid would not have a distinct $\tilde{S}$, since the S2 would start immediately. Therefore we determined that we would not consider such tracks that crossed the liquid-gas interface.

With the undergraduates, we looked at how the waveforms of the muon tracks were processed in terms of S1s and S2s with the Processor for Analyzing XENON (PAX) [74]. It became clear that muons traveling a large vertical distance in the detector were often broken up into multiple S2s. Also, these S2s could be cut shorter by a parameter in PAX "max_hits_per_pulse". This parameter limited how much light a single PMT could see in a given time in order for the processor to count it toward an S1 or S2. We reprocessed some data by increasing this value by an order of magnitude and it did not make the processor slower.

By the summer of 2019, we created an expectation for a MIMP track through XENON1T. The S1s would create an $\tilde{S}$ that would be tagged as an S2 by PAX, but would be in the liquid and not the gas. Due to internal reflection at the liquid-gas interface, most of an S1's light is seen by the bottom PMT array, which we quantify as a low "area_fraction_top", or the fraction of light seen by the top array compared to all light seen to create a peak. The $\tilde{S}$ would have this low area_fraction_top despite being classified as an S2. The actual S2s of the track would likely be split into many similarly-sized S2s. We elected to change some splitting parameters in PAX, as well as the "max_hits_per_pulse" and reprocess the data so that we could recover the expected very long, very energetic single S2.

Dr. Michael "Mike" Clark joined the group in October of 2018 and took over this analysis for the summer of 2019. We noted that the XENON1T single-scatter limits were not shown to extend to higher masses than 10^3 GeV/c^2 [2]. He extended the XENON1T limits to 10^{18} GeV/c^2 and a cross section of 10^{-30} cm^2 and re-cast the Majorana Demonstrator's limits on tracks from lightly ionizing particles [75]. Our paper published in *Physical Review D*, shows the limits on heavy dark matter in Figure 2.5. He also calculated XENON1T's sensitivity to MIMPs scattering with different multiplicities [76]. There was not much difference

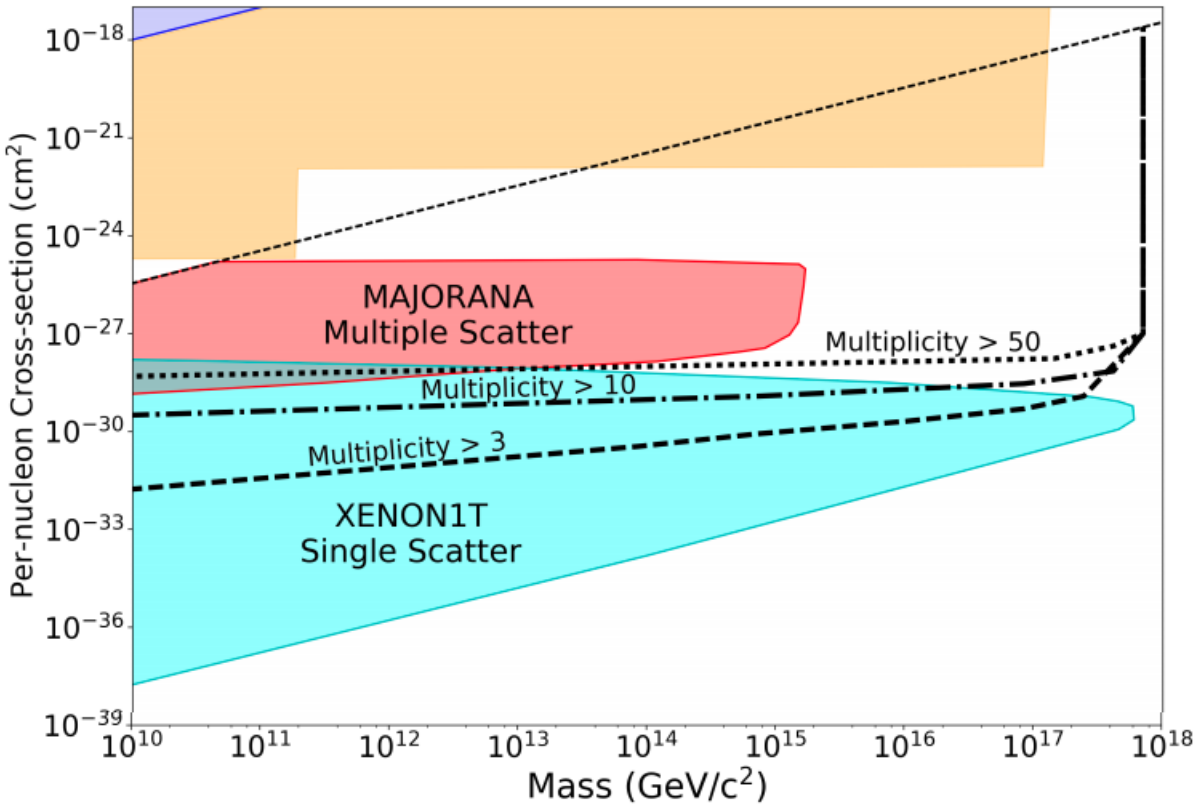

Figure 2.5. Limits on heavy dark matter scattering once in XENON1T and multiply in the MAJORANA DEMONSTRATOR. The sensitivity of XENON1T to MIMPs with different interaction multiplicities are shown. The light dashed line forming the upper limit to these searches indicates where the MIMPs would be stopped by the rock overburden of these underground experiments. From Reference [76].

between 10 scatters and 50, but the 50 would give a clearer $\tilde{S}$. Mike and now Dr. Shengchao Li, a new post-doc, are completing the analysis for MIMP tracks in XENON1T based on the projected sensitivities and two academic semesters of work performed by undergraduates.

2.3 Muons in XENON1T

With the success of the undergraduates' heavy dark matter projects, we started something new for the Fall 2019 semester. We offered a course-based undergraduate research experience with support from Purdue's Data Mine initiative. Students enroll in a living community and choose to partake in real research from a myriad of departments. For our

course on particle physics research, we coordinated with Professor Andy Jung's group. The physics researchers would have a combined lecture hour on Monday to learn physics research techniques, including an introduction to python with Jupyter Notebooks, error propagation, common variable distributions (Gaussian, Poisson), back-of-the-envelope estimations, and dimensional analysis. Directly after the lecture hour, the students were divided into two cohorts for an hour seminar. Some conducted research with us, using data from XENON1T. The others conducted research with Andy's group using data from the Compact Muon Solenoid (CMS) experiment at CERN's Large Hadron Collider (LHC) [77].

During our seminar throughout the semester, each student would give one short science presentation on a topic relating to dark matter and particle physics. Other than this project, the students would submit work as a group and present their group progress every few weeks. We created groups of three to four students, and each group would be assigned a graduate student TA to meet with the groups and oversee their progress. We decided to continue the theme of tracks and focus on muon physics in XENON1T. There were groups exploring muon-generated particle interactions, including NRs from muon-generated neutrons and muon spallation of xenon nuclei in the detector. For spallation, a muon's impact on a xenon nucleus could cause it to break apart into other elements and particles. We also looked into any atmospheric temperature-dependence, which was previously recorded by the GERDA experiment as shown in Figure 2.6. GERDA, like XENON1T, is located underground at the Laboratori Nazionali del Gran Sasso (LNGS) in Italy [78].

We did not find anything particularly noteworthy after a muon trigger. A significant number of events were immediately following the trigger, but there did not appear to be any increase in events beyond a millisecond. It was impossible to determine what spallation would look like, and there were no significant NRs from neutrons. We successfully accessed NASA temperature data to start to recreate Figure 2.6, but calculating the muon rates was more difficult than originally anticipated. Selecting muon trigger events and then calculating the livetime by which to divide them to get an accurate rate was not achieved within the time frame of the course. Livetime calculations are notoriously tricky, and was especially so for me in Chapter 4.

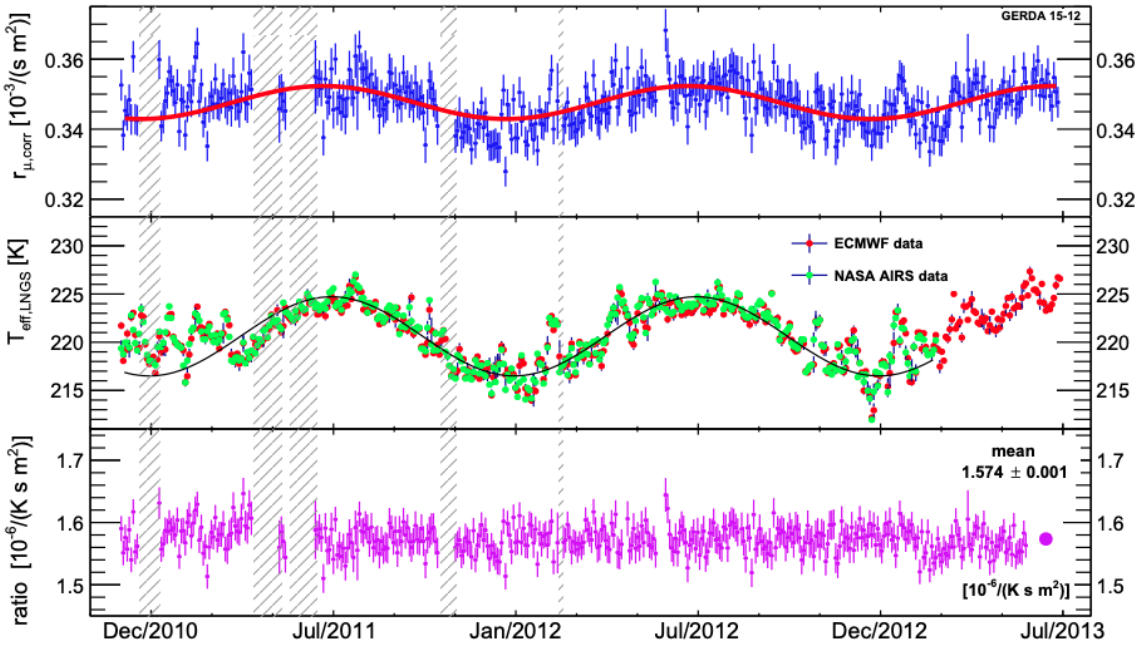

Figure 2.6. Top Panel: the muon flux rate over several years in the GERDA water tank. Middle Panel: the corresponding atmospheric temperature in Gran Sasso during that time. Bottom Panel: the temperature normalized muon rate. From Reference [78].

For the second year of the Data Mine, I won a Graduate Fellowship from the Indiana Space Grant Consortium to focus the undergraduates' efforts on detecting CEvNS from Boron-8 Solar Neutrinos in XENON1T. We would try to detect single-photon S1s. Since this is a topic on which I performed a significant amount of work too, I recount it in Chapter 5.

2.4 Conclusion to the Big Sphere Radon Veto and Mentoring Undergraduates

Overall, my experiences with research at the more basic levels as recounted in this chapter have been useful both as a starting point for my own work and for determining how best to launch the research careers of undergraduates that I mentor. The Radon Veto was an interesting challenge to code up the Radon-Polonium pairing and detector cylindrical geometry with the Big Sphere veto regions. As someone who learns best by doing, it was an excellent introduction to Python.

I firmly believe that small groups of three or four first-time researchers are the best way to organize students and teach them basic research techniques. The groups enable the mentor to offer research experience to a larger pool of interested people, and the new researchers have other people with whom to discuss problems and ideas. The mentor can be less involved as the groups learn collaborative skills and figure out which direction the research should take within the big picture. The students develop a better understanding and ask better thought-provoking questions. Provided the group members are all excited, motivated students, researching in a group is generally more fun.

Throughout these years we have certainly had groups with less-motivated students and poor group dynamics. Part of the experience can be learning to work with difficult people, but we would accommodate students that would like to switch groups. Although making that point clear at the beginning of the semester, we have not needed to switch groups. We do focus most of our energy on supporting the students who appear to be trying.

Research is inherently frustrating, because no one, not even the mentor is sure that a procedure will work as expected. It is hard to gauge progress and success when one is the only new researcher on a project. Being in such a position can lead to anxiety and low self-worth that deter people, particularly under-represented minorities, from pursuing a career

in physics. From the mentor side, clear expectations and constructive feedback are key to alleviating such anxiety, with generous praise when deserved. Frequently scheduled meetings help benchmark progress and brainstorm how to move forward. After brainstorming, it is beneficial for the mentor to summarize and build on the ideas with goals for the next week. This way, the students are eased into research with more structure. With more experience, the mentor role changes from dictating what to do next, to discussing and approving the steps proposed by the students.

Through groups, new researchers learn data analysis techniques, and life skills such as collaboration, leadership, critical thinking, and problem solving. They learn to accept failure and learn from it to eventually succeed. Many people are not willing to endure this, and it is better for them to realize that as an undergraduate rather than a graduate student. However, I think we accomplished making physics research as accessible as possible.

This experience was extremely valuable to me too, since I want to become a University Professor. I am very grateful to the National Science Foundation for awarding me a Postdoctoral Fellowship to continue my work with liquid xenon TPCs and encourage underrepresented minority students to feel welcome pursuing physics.

3. A SMALL TPC FOR EXPERIMENTAL RESEARCH IN XENON

ASTERiX - a Haiku

Purdue's detector
for particles in xenon
is named ASTERiX.

The Purdue detector is lovingly named ASTERiX, after the Gaul of comic book fame [79]. I turned the name into an acronym: **A S**mall **T**PC for **E**xperimental **R**esearch **i**n **X**enon. Darryl had begun the process, but I still had a lot of work ahead of me to get ASTERiX operational. In this chapter, I describe the full ASTERiX system, with particular attention to its quirks and evolution into the final design. Figure 3.1 shows the ASTERiX detector and gas system front panel. The television screen mirrors the central laboratory computer's screen, which keeps track of the operating conditions and stability, using the LabView program Vitalstatistix.

A diagram of the actual TPC in its final version is shown in Figure 3.2. The active xenon target is bounded by seven stacked Teflon pieces. The bottom disk acts as a reflector rather than having a bottom PMT array. At first, infrared (IR) LEDs were embedded in the bottom, but later they were changed to a fiber, as described in Section 3.6. The next three layers each are 1 cm thick and hold an electrode: Cathode, Gate, and Anode as described in Section 3.3. The thickest piece, the light cone, distances the PMTs from the anode. Seven Hamamatsu R8520 PMTs are cradled between the top two layers to look down into the detector, and are further described in Section 3.4.

Various holes are drilled into the Teflon layers around the outside for different instruments. In Figure 3.2, the holes for the inlet from recirculation, and weir are shown. The IR LED fiber actually goes around the outside of the Teflon stack and is inserted through a hole in the bottom to connect to the diffuser. Other holes drilled top-down around the TPC hold a PT100 temperature sensor, and a coaxial capacitor level meter.

The TPC is suspended at the bottom of a meter-long cryostat, and the Teflon layers do not prevent liquid xenon from flowing in and out of the active region through cracks, mixing

Figure 3.1. A picture of the ASTERiX detector, shielded with lead bricks. Vitalstatistix on the monitor screen and the gas system panel with valves are visible in the background.

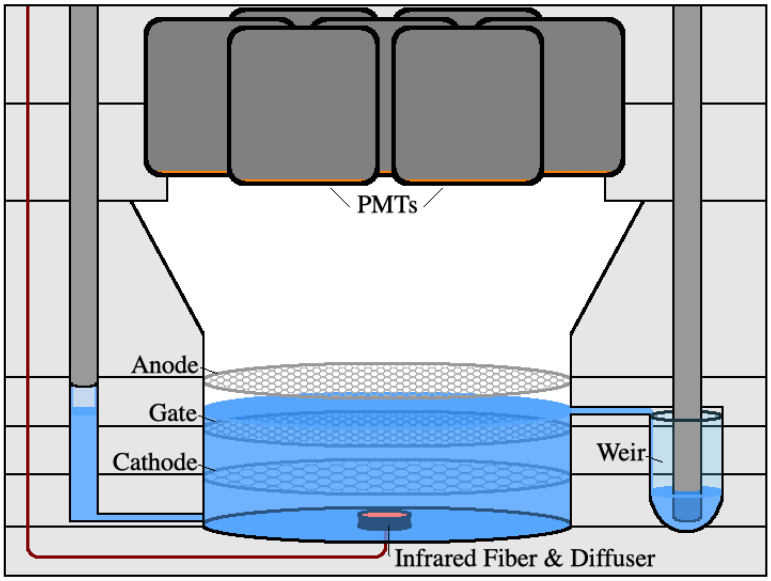

Figure 3.2. The final ASTERiX detector configuration with fiber-coupled infrared light diffuser and weir.

with a pool of xenon at the bottom of the cryostat. A copper piece on the underside of the bottom disk holds the reboiler heating cartridge and another PT100 temperature sensor. There used to be a diving Bell that fit over this entire stack, and pressurized it to maintain the liquid level with a heater in yet another drilled hole. The heater could burn the Teflon, so I had the excellent glassblowers in the Chemistry Building make a glass sleeve from a test tube to line its hole. The heater would heat the TPC, increasing the vapor pressure, which would force the liquid down and outside the Bell. The level meter reading was supposed to inform how much to heat to maintain the level with a proportional-integral-derivative (PID) controller in LabView (see Section 3.1).

As will be described in Section 3.6, the IR LEDs had a larger heat load than light output. They actually heated the xenon, pressurizing the Bell and reducing the liquid level, leading to a larger gas amplification region and larger S2 signals. With this liquid level instability, I chose to discard the Bell system, remove the PID heater (despite affectionately naming it Pete), and construct a spill-over weir to maintain the liquid level. Another transition was from milliwatt IR LEDs to an optical fiber able to conduct a Watt of IR light.

With the Bell, the to and from recirculation pipes connected with the reservoir of xenon at the bottom of the detector, and clean xenon did not as readily enter the TPC through the cracks in the Teflon layers. This led to worse purity. With a weir system, I had direct access to the top of the detector stack, and could insert the clean xenon from recirculation into the TPC. I then needed to draw the xenon to recirculation out of the weir. To construct the weir, I again asked the glassblowers to turn a 3/4 in diameter test-tube into a 2 cm high weir. I also required two small protrusions on the side to help lock the weir in place relative to the Gate electrode. In the Teflon piece between the Cathode and the Gate, I used a Dremel to carve out a channel for the wings of the weir. They slid down and rotated to lock in place. This positioning left the top of the weir about 2.5 mm above the top of the Gate, which is optimal for the single electron gain. While the weir was enough for my work, and the full meter-long cryostat had temperature and pressure stability for hours, the weir volume was very small compared to the rest of the detector.

A future weir design should hold on the order of 0.1 kg of xenon, comparable to 1/2 cm of depth in ASTERiX and the precision of the level meter reading. The current small weir

can only hold roughly 0.01 kg, and is difficult to find, despite a constant filling speed, due to the large fluctuations in the level meter. It is best to rely on how much xenon has been filled, which can be done with Vitalstatistix.

3.1 Vitalstatistix

Slow Control - a Haiku

Our detector needs
stability to function.
It is just like me!

The operation of ASTERiX relies on stable conditions: constant temperature, pressure, purification, and liquid xenon level. The sensors for these components are supported by National Instruments LabView [80] code. After a few undergraduate students had learned to connect to the different sensors from LabView, I collected the code snippets into a single program, called Vitalstatistix. The front panel of Vitalstatistix is shown in Figure 3.3.

The top graph's red line of Figure 3.3 reads the pressure, measured with a Heise DXD pressure sensor. Its instantaneous value is also depicted in the top right gauge icon and shown in the red-highlighted box. When operating, the absolute pressure should not exceed 3.5 bar or the vacuum-filled PMTs are at risk of imploding and the pressure burst disk will rupture, releasing the xenon into the lab. It should also not drop to 1 bar (atmospheric pressure and indicative of a leak), or below (indicating that the xenon is frozen solid). A gauge on the top of the detector can also be checked manually. As a gauge pressure, it should not exceed 2.5 bar but should be greater than 0 bar.

The orange line is Heater 1, which is controlled by a PID controller of the Lakeshore 336 Temperature Controller. The yellow (gold) line is the temperature of the coldhead (coldfinger, hence goldfinger) of the Cryomech PT90 Pulse Tube Refrigerator (PTR). The Lakeshore maintains the temperature of the coldhead (Input A) at 172 K by compensating for variations in the detector's heat load with Heater 1. The yellow-green line monitors the PT100 temperature sensor (Input B) near the ConFlat flange of the cryostat where there is a switchboard for connecting electronics' wires on the inside to the electric feedthroughs to go outside. This

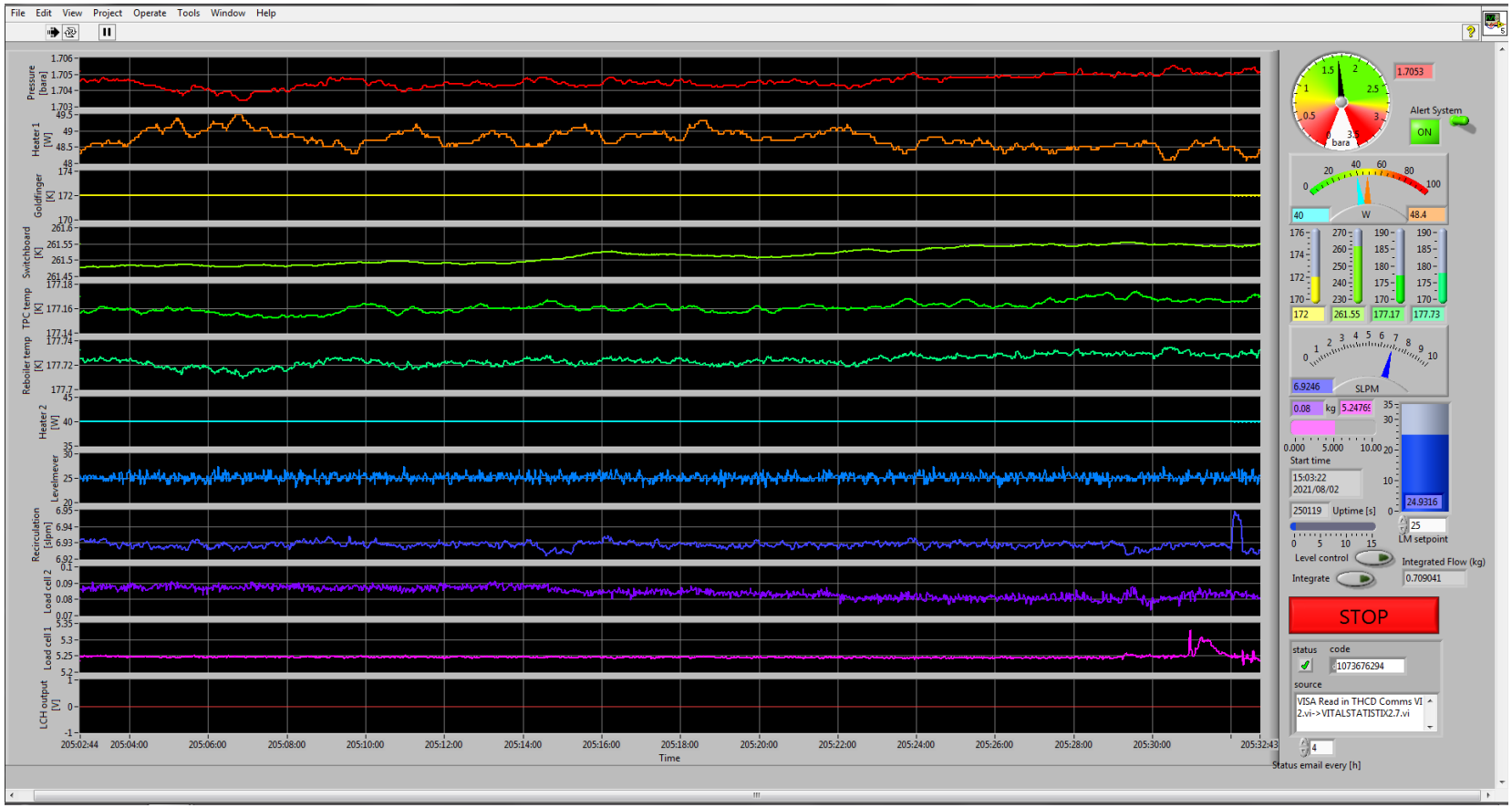

Figure 3.3. Vitalstatistix front panel with controls and real-time monitoring.

is far from the coldhead that drops liquid xenon to the TPC at the bottom of the cryostat, so it stays about 250 K. The bright green line is the temperature in the TPC (Input C). When the TPC is full of liquid xenon at about 177 K, it reads the same temperature as the mint green line, which monitors the very bottom of the cryostat (Input D), where there is a reboiler heater. The heater is only used for faster recuperation. The cyan line is Heater 2, which is necessary to help Heater 1 maintain the coldhead at 172 K with the overpowered PTR.

Heaters 1 and 2 are also represented on the dial below the pressure gauge on the right, with corresponding color-highlighted boxes with the instantaneous values. The four temperature sensors' values are shown like thermometers with nearby highlighted boxes, all appropriately colored to correspond with their respective plots. LabView just reads the Lakeshore values for Heater 1, the four temperature sensors, and Heater 2. Therefore, Heater 1 and 2 need their heater range to be set up manually from "None" (off) to "High" as outputs 1 and 2, respectively, on the Lakeshore unit itself. The coldhead's setpoint for the PID to control Heater 1 can also be changed there.

The blue line is the level meter capacitance reading. A metal rod is set in a metal tube, with fishing line as a spacer to make a concentric cylindrical coaxial capacitor. Liquid xenon, a dielectric liquid, seeps up into the gap and increases the capacitance reading. It is very sensitive, and the calibration offset changes dramatically if the electrodes trip with a sudden discharge. However, it is generally precise for stability. The color-coded gauge on the right side of the screen shows the level reading in millimeters.

The indigo line reads the Teledyne Hastings THCD-100 flowmeter. This is integrated in LabView to check how much xenon is let in or out of the system, and it maintains recirculation at 7 Standard Liters Per Minute (SLPM). This value is a good recirculation speed for the purifying MonoTorr PS4-MT3-R-1 getter, and reins in the power of the Air Dimensions, Inc double head DiaVac R272-BT-AA1 diaphragm pump that drives recirculation. LabView just reads out the flow. The setpoint can be configured on the display inset in the gas system panel. The flow value is shown via the speedometer indicator and indigo-highlighted box on the right-hand side of the LabView front panel. Before xenon starts flowing, it is generally a good idea to zero the flow on the display.

There are actually two bottles to store xenon, although only one is generally used at a time. The Load Cells measure how much xenon is in the bottles. Load Cell 2, purple, has a bottle at less than atmospheric pressure, ready to act as a release volume for xenon from the detector if the cooling power fails. Load Cell 1, pink, has most of the xenon inside. When filling from Load Cell 1, the mass decreases as xenon enters the system, matching the integrated flow through the flowmeter. For recuperation, the bottle is immersed in liquid nitrogen to freeze the xenon, creating a vacuum to cryopump the xenon out of the detector. Therefore, the buoyant force of the liquid nitrogen makes the reading unreliable. A bar on the side indicates how full the bottles are, color-coordinated, and their instantaneous readings are depicted in the corresponding highlighted boxes.

The program can be started by the arrow in the top left, but in order to shut down all communications correctly and close the program safely, the red Stop button must be used. In the top right there is a toggle for emergency SMS and email alarms if the pressure or temperature sensors leave safe operating ranges. Above the Stop button is a rocker switch to integrate the flowmeter for filling and recuperating. The program must be briefly stopped to reset the integration. When the system operated with a diving Bell, a PID controller accessed the level meter reading and tried to maintain a constant level with a heater, which is the maroon line on the graph and "level control" rocker switch. This never really worked because of the finickiness of the level meter. If there is a problem with communicating with an instrument, the error shows in the text box at the bottom right. The values are written out every ten seconds to a csv file, and a general status update email is sent at a configurable time interval, set by the box below the Stop button.

The back end of Vitalstatistix is shown in Figure 3.4. Generally, all communications to the devices are initialized in a stacked sequence structure, one after another. Their connection information and the initial csv storage information is fed into the perpetual while loop operating at 4 Hz. There, the devices' values are read out cyclically in another stacked sequence structure. The values are shown on the front panel and saved every ten seconds to the csv file. They are also sent in a status email with the desired frequency. If the alert system is active, the pressure and temperatures are checked for anomalies. If there are any, it sends out SMS text messages and emails every two minutes as long as the problem persists.

The alert thresholds, email addresses, and phone numbers (using a carrier-dependent email to SMS functionality) can be hard-coded in the "Send Alert!" function. This icon can be double-clicked to open its screen to alter these values. When the big red Stop button is clicked, the while loop ends, and the connections to the devices are safely closed.

3.2 Gas System

Xenon - a Haiku

Xenon gas is rare.
We keep it sealed up tightly
so that it stays pure.

Xenon is a particularly rare element, so it is imperative to maintain the amount we have in an enclosed gas system made of Swagelok ultra high vacuum VCR components. Figure 3.1 shows the gas system panel in the background, and Figure 3.5 is a more detailed drawing. Xenon gas is stored under high pressure in a bottle, and the amount needed is let into the ASTERiX detector during filling. When ASTERiX no longer needs to operate, the xenon is recuperated back into the bottle for storage.

Once the ASTERiX TPC is mounted in place, the cryostat can be lifted closed. The cryostat's ConFlat flange is sealed with 24 half-inch bolts and nuts, and a clean, 10-inch copper gasket (that has not been used more than 3 times). The large black lever next to the cryostat controls the gate valve, and should have been closed. To prepare for filling, open this and turn on the backing (roughing) pump by plugging it in. The lab used to have an Adixen ACP 28 dry scroll pump as a backing pump, but it seized up. Now there is a little Pfeiffer 015-4 diaphragm pump, and it takes longer to get down to $\sim$1 mBar pressure to turn on the Turbo pump, a Pfeiffer HiPace 300. The backing pump pressure can be monitored by the Pfeiffer SingleGauge module mounted on ASTERiX's Bosch frame side nearest the gas system panel. The Pfeiffer control module for the Turbo pump, which also monitors the TPC vacuum pressure, is to the left of the SingleGauge module. When the backing pump's pressure reads about 1 mBar, turn on the Turbo. It will spin up and the TPC pressure

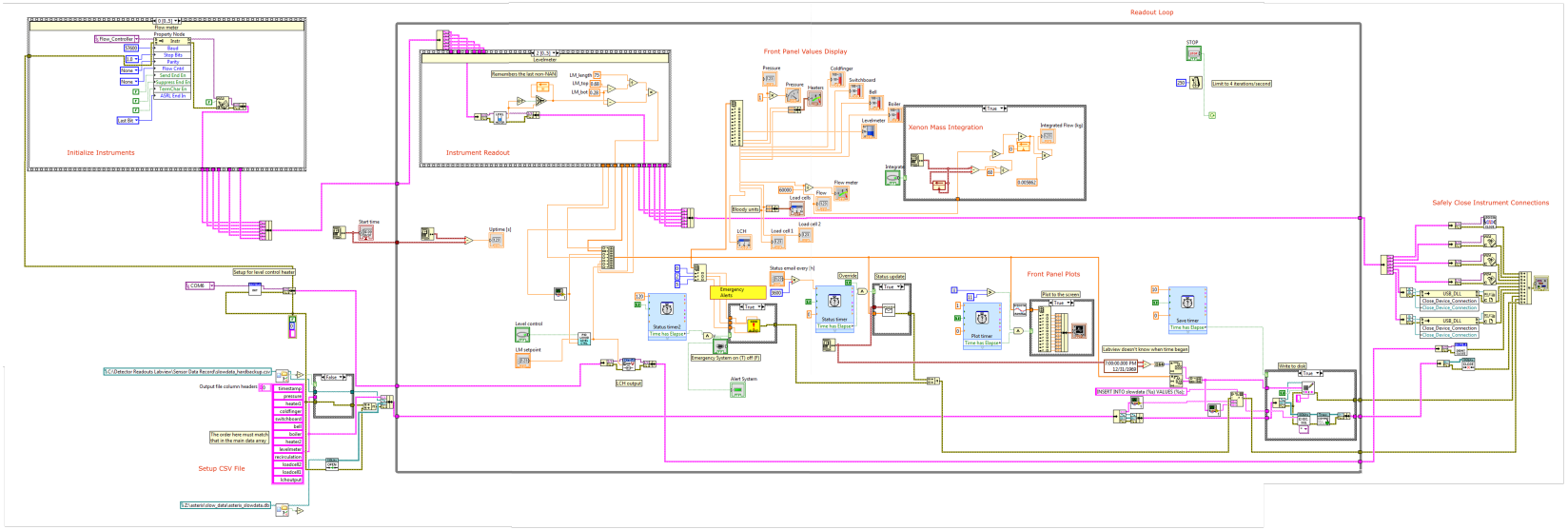

Figure 3.4. Vitalstatistix block diagram showing the general structure for how Vitalstatistix works.

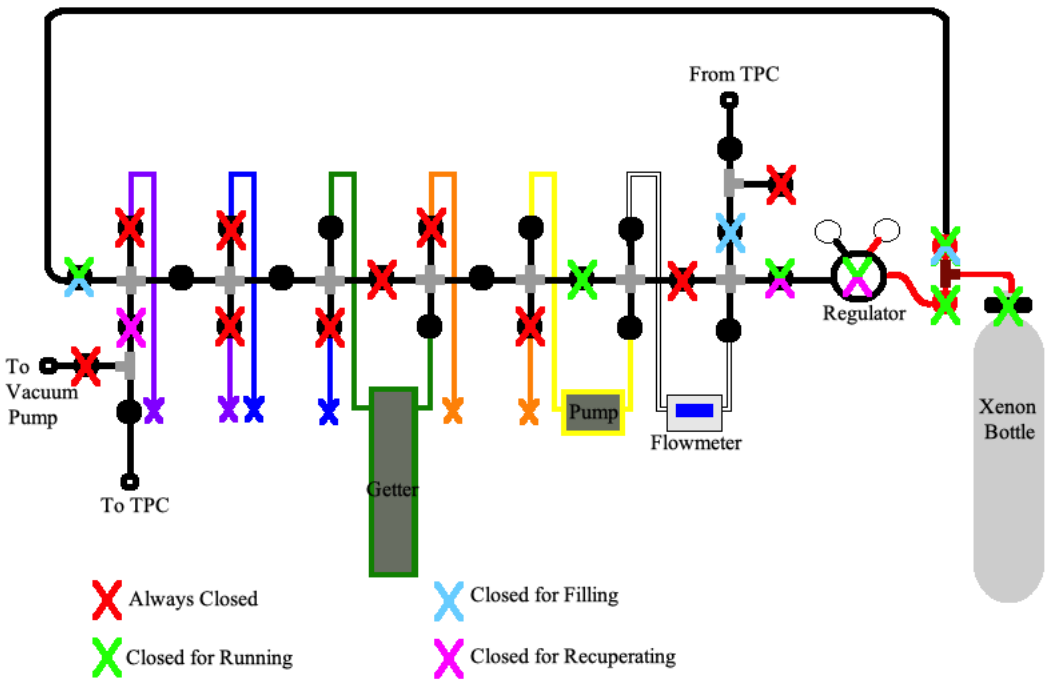

Figure 3.5. The schematic of the gas system. Valves closed for certain operations are denoted.

should drop to 1e-4 mBar rapidly. Pumping to $\mathcal{O}$(1e-6) mBar is preferred and $\mathcal{O}$(1e-8) mBar was achieved in 2021 after pumping for over a year because of the pandemic.

There are two ExTorr residual gas analyzers (RGAs) to check for leaks: RGA 6380 is on the top of ASTERiX, and RGA 7136 is near the HiCube 80 Eco vacuum pump that connects directly to the gas system, as labeled in Figure 3.5. RGA 7136 on the HiCube is only used if a change is made to the gas system, which then needs to be pumped down and leak checked. Alcohol can be sprayed on new connections and the partial pressure of the alcohol mass should not increase. One can also use the Argun; the air gun connected to the argon bottle. The partial pressure of argon should not increase if a connection is leak tight and sprayed with argon. The Argun should be used to check the cryostat ConFlat flange after closing with RGA 6380.

To use an RGA, plug in its power cord on the device itself. Check the correct RGA's communication cable is connected to the central lab Windows computer, and click the corresponding RGA's ExTorr configuration file shortcut on the desktop. In the ExTorr software, click the light bulb icon's switch to start the filament. The scan starts automatically, or press the green "Go" button. The light bulb will turn yellow and the red line will perform continuous mass sweeps tracing the spectrum outlined in black. It should be allowed to run for about half an hour or longer before the black baseline flattens out and the residual gas species' mass peaks are clear. The largest should be four xenon bumps around 130, and a scaled down version of those same peaks around 65 for doubly-ionized xenon. A good scan after the baseline has settled should be printed to a PDF and saved to the computer. For leak checking, the operating parameter should be "trend" rather than the "mass sweep" to track the partial pressure of a specific gas (ethanol or argon) with time. The sound can also be enabled to be particularly annoying, rising in pitch if there is a leak. When finished, turn off the light bulb icon, close the program, and unplug the RGA's power.

With the detector closed and under sufficient vacuum, it is time to fill with xenon gas. On the gas system panel as in Figure 3.1, flip the red rocker switch along the green path to turn on the MonoTorr PS4-MT3-R-1 hot zirconium getter. It will beep, which has to be acknowledged by pressing the bottom button on the back, and then press the top Heater On button to start warming it up for purification. When it gets up to temperature the Life

Status should have a green LED on next to Good, the Valves should have a green LED on next to Purifier, the Temperature should have a green LED on next to Set, and the Heater should have a green LED blinking next to Operating.

On the central lab Windows computer, open the Vitalstatistix LabView program, detailed in Section 3.1, via its shortcut on the Desktop. Make sure the toggle for the alert system is off because the absolute pressure and temperatures will be out of range. The gate valve black lever can be closed again, the Turbo turned off, and the backing pump unplugged.

All of the valves should be closed, but the valves with red and blue X's in Figure 3.5 absolutely must be. There are two more locations for bottles than are shown. They have similar top red valves that connect into the low-pressure side for recuperation, and bottom red valves that go to the regulator. They should also stay completely closed. To open a valve, grasp the knob and turn left all the way then back closed half a turn. Totally open valves can feel sticky, so it is easier to check if a valve is opened or closed by trying to close it a little more. The red high pressure valves and the valves on the bottles (both SS-3NBVCR4) have lock nuts that seal the valve. It is very important not to loosen these nuts when turning the valve knob, or they will leak xenon. For filling, the valves along the path can be opened slowly, starting at the bottle. The gas in the bottle will be at a high pressure, and only the tubing colored red in the figure is safe for high pressure. The top red valves must be closed when operating at high pressure. The bottom red valve can now be opened into the regulator. A good regulator setting is 150 kPa on the left low-pressure side's gauge. To fill to twice atmospheric pressure, a slight over-pressure in the regulator can accelerate the process.

On Vitalstatistix, flip the rocker Boolean control to turn on the mass integration to know how much xenon is entering the system. The xenon, at an appropriate pressure, can be let into the system from the regulator through the first valve and down into the white-labeled loop through the Teledyne Hastings THCD-100 flowmeter. The flowmeter can already be configured to automatically allow a setpoint of 7000 ccpm, which is 7 SLPM. By having a back pressure, the recirculation diaphragm pump does not need to be on. However, there are two buffer volumes that should be filled on either side of the pump, so the two valves to the yellow loop can be opened in addition to the bypass valve between them. At this time, no

dissolved sources are needed, so the orange, blue and purple loops will be bypassed. Make sure that the getter is up to temperature: the Heater's green LED next to Operating should be blinking and the Temperature should be Set. Then open the valves going to and from the getter. After bypassing the blue and purple loops, there are two valves down toward the TPC. On the top of ASTERiX on the side near the whiteboard are two more valves, both of which can be opened. After opening the "To TPC" valve, listen for the xenon entering the system, and watch the pressure climb, flowmeter jump to a steady rate, the bottle mass decreasing slowly, and the mass integration increase on Vitalstatistix.

With 2 bar gas, the bottle can be closed. The rest of the xenon in the high pressure side will slowly pass through the regulator until it is no longer under high pressure. At about 500 PSI, the high pressure pipes hold 0.017 kg. The flowmeter reading will drop to zero and mass integration on Vitalstatistix can be stopped, which will read about 0.42 kg. The valves in Figure 3.5 with green X's should now be closed, and the from TPC ones opened to form a loop from the detector, through the flowmeter, pump, and getter, and back to the detector. The pump can be turned on with its switch on the front gas panel. Now is a good point to check the PMTs and electrodes. If they achieve the desired voltages and there are S1s and S2s visible on the oscilloscope, then proceed with cooling down.

In the back room 340A, check the PTR compressor's Low pressure. It should be about 210 PSI. If it is much lower, it has to be primed with the regulator and tubing on the the nearby shelf and the helium bottle on the rack. Lay the bottle down VERY gently, and move it close to the compressor to connect everything. Keep the compressor's vent valve closed. Pressurize to 200 PSI and re-close the regulator. Using the little t-valve on the tubing, partially vent the tubing to about 20 PSI into the room. Pressurize, close, and vent 8 times before setting the 210 PSI on the regulator and opening the compressor's vent valve. This ensures that pure Helium from the bottle enters the compressor and reduces impurities in the tubing. Once the Low pressure is 210 PSI, close the vent valve and bottle, and vent the tubing and regulator with the t-valve before putting the helium apparatus away. Prior to turning it on, open the cooling water valves on the wall to and from the compressor. Press the green button, and start the cooling. The compressor will roar to life. Listen for the rhythmic pulsing. If the pressure was lower than 210 PSI and not sufficient, it will stop.

Press the Pressure reset button near the bottom and it will try again, but if it keeps turning off, then helium must be added.

Before the xenon flash freezes, make sure Heater 1 on the LakeShore is working. It should show the 172 K setpoint and what percentage the heater is outputting of a range. If the heater range is "None", change it to "High" through the Output Setup button. The temperature and pressure will drop. Once the xenon temperature reaches the setpoint of 172 K, Heater 1 should start heating up. When it gets to 40 W on Vitalstatistix, turn the Heater 2 of Outputs to 80% of "High" to help compensate.

At 172 K, the pressure will decrease. As liquid xenon droplets drip down from the coldhead, they fall into a funnel down into the TPC. Therefore, the TPC and reboiler temperatures should drop to around 180 K. Now, proceed with filling liquid xenon. Recirculation can be stopped by turning off the diaphragm pump, and the valves with blue X's closed. Start the integration on Vitalstatistix, stopping and restarting the program if needed to reset. Beginning with the bottle, open it and the bottom red valve to the regulator. Open the regulator to 100 kPa gauge pressure and let that flow into the detector, bypassing the pump, as the coldhead liquefies it. Since the TPC has a flat bottom in a rounded-bottomed cryostat, about 1.2 kg of xenon needs to be added to the 0.4 kg already inside to reach the TPC's bottom and the level meter.

At this point, there is a little over 0.02 kg per mm of level. Up to the Cathode is 0.2 kg, then more of the same to the Gate electrode. With 2 kg of xenon total in the system, close the bottle. Turn on the PMTs and check that the level is above the Gate by applying a large potential difference (>4 kV) between the Cathode and Gate. If no S2s are visible, then the level is above the Gate. Otherwise, open the bottle and close it to fill in increments of 0.017 kg from the high pressure side until the level is above the Gate. Now is a good point to run a PMT calibration and take some data at the target electric field configurations.

The weir is positioned 2.5mm above the Gate and holds 0.01 kg, so there should be about 0.05 kg still needed. A test data set should show the full 10 μs drift time (depending on purity) for events. A waveform from that data set should indicate that the PMTs are saturating and therefore the liquid level needs to increase to reduce the amplification. The ASTERiX version of the processor, is not optimized for large, wide single electrons, although

the configuration files can be adjusted. Increase the level slowly, 0.017 kg from the high pressure side at a time, and take data to double-check for saturation. Once the level gives good data, keep ASTERiX recirculating with the pump pulling xenon out of the detector, controlled by the flowmeter, and pushing it through the getter and back into the detector.

For recuperation, fill the dewar under the bottle with liquid nitrogen. Open the bottle and bottom red valve to the regulator and see the pressure drop to zero. Only when the regulator shows zero pressure is it safe to open the top red valve. Turn off the diaphragm pump and bypass it. Turn off the PTR Compressor with the same green button and close the cooling water valves. With no xenon flow, start integrating on Vitalstatistix and turn off the alert system. Close the valve down to the TPC with the magenta X, and open the valve nearby to the bottles according to Figure 3.5. Xenon will flow out of the detector, through the flow meter and getter, and into the frozen bottle. The reboiler heater can be turned on to >20 V to boil off the liquid xenon in the bottom of the detector. Try to maintain 2 bar absolute pressure in ASTERiX with the reboiler to avoid flash freezing the xenon in the bottom of the cryostat. The TPC and reboiler temperatures will increase dramatically when they are free of liquid xenon, and the reboiler heater can be turned slightly down to avoid temperatures much above 293 K. Check the regulator pressure often, and add liquid nitrogen to keep the bottle frozen as needed.

The TPC pressure will drop close to zero, the temperatures approach 270 K and the flow reading will decrease over several hours. The integrated mass should be over 2 kg. The pump bypass valve can be closed and the pump restarted to pull the last bit out. When the flow is below 0.01 SLPM, that is less than 5 g per hour and not worth a graduate student's time. Turn everything off, and close all the valves on the gas system, including the two at the top of ASTERiX near the whiteboard.

While at Purdue, I thankfully never had any trouble with the getter. I did have to prime the PTR compressor with helium twice, and replace the diaphragms on the recirculation pump. The pump was leaky, and requires three-ply Teflon diaphragms in Air Dimension's #11011 kits. The torques on the hex screws holding the diaphragm pump together are very particular and available on the specifications sheet. The diaphragms are only rated for a year (less with such a heavy gas as xenon) so I set up the run time counter on the gas system's

panel. At 5,000 hours uptime, the diaphragms need to be replaced. I also witnessed the dying crunch of the Adixen scroll pump and had to improvise with the Pfeiffer diaphragm pump.

In the summer of 2018, we calibrated the load cells. The hard-coded calibration parameters can be set to 1 in the instrument readout stacked loop, and weights added to load cells. Then fit a line to the load-cell readout values and the actual mass values to find the calibration parameters. The level meter can also be calibrated, although it does not stay very long if the electrodes discharge often. The reading when the detector is empty is 0 mm, and then the detector can be filled with xenon until the reading stops changing, and that is 75 mm.

The scariest problem I had with the gas system was when the high pressure Swagelok SS-3NBVCR4 valves started leaking xenon from around the knobs' shafts. There is a lock nut that seals in the high pressure and the xenon will escape if it is loosened. For extra reassurance, the PTFE packing, which forms the seal when compressed by the lock nut, was replaced.

3.3 Electrodes

Electrodes - a Haiku

Two voltages placed
on electrodes well-spaced make
an electric field.

The three electrodes in ASTERiX are stainless steel hexagonal-etched meshes. The Gate and Anode wires are 125 μm with 2.51 mm hexagon pitch. The Cathode is 75 μm wires with 5.33 mm hexagon pitch. The meshes are stretched across stainless steel rims. Since the PMTs are so far from the Anode, no screening electrode is required. In order to detect single electrons with seven PMTs and a 1 cm spacing between the Gate and Anode, a voltage difference exceeding 5 kV was found to be necessary.

The rims have two holes in them with inset female adapters for the male plugs. Darryl distrusted the plugs from past experience with them falling out, and made brass clamps that

fit over the rims. It was a secure electric connection, but the electrode stack configuration was too close-set and there was a high probability of electric discharge between the brass clamps above 4 kV between the Gate and Anode. For a millimeter gap, 1.7 bar of Xenon has almost half the discharge voltage compared to that gap in an atmosphere in air, as seen in the Paschen Curves of Figure 3.6. At the suggestion of Dr. Sergey Pereverzev, we added 1 GΩ resistors to the high voltage wires between the electrodes and the high voltage source. The electrodes still charge through the resistor to the correct voltage, but the high voltage channels are buffered if there is discharge current between electrodes.

My solution to the electrode connections was to create a plug with a Teflon clamping around the male pin, as in Figure 3.7. The male pins do lock into the female connectors inset in the electrodes, but they take a lot of delicate pressure. With these connectors, the point of breakdown actually became the vacuum feedthrough. The Anode has its own Kings connector feedthrough, but the Cathode and Gate were on SHV connectors. Even so, those were vacuum feedthroughs and not optimal in xenon. The Wiener EHS 40200X high voltage module should have been able to output up to 20 kV, but breakdown occurs below 8 kV in the Anode feedthrough. For the Gate and Cathode feedthrough, it was 2 kV. I ordered a T ConFlat piece and a double Kings feedthrough for the Gate and Cathode to operate the Gate and Cathode at negative high voltages while the Anode was at positive high voltage to maximize the voltage differences while limited by the absolute voltage.

I accidentally broke one of the positive high voltage channels of the module while checking the connections and jiggling them while they were on. It tripped and then was not outputting the correct voltage with a reasonable current. Even when channel 0 said it was off, it could be measured to be above 1 kV. The module was sent to Wiener and fixed recently. Luckily the module has two positive high voltage channels, and I ran with channel 0 broken but using channel 1 instead for my main analysis in Chapter 4. With my feedthrough and clamp modifications, I could achieve a sufficient field to observe single electron signals.

The analysis required dedicated high-energy events. Purdue's Radiation and Environmental Management (REM) officers approved the deposition of Polonium-210 on the Cathode. Figure 3.8 shows a picture of the deposition and the reconstructed position of the source in ASTERiX amid background events. We ordered a 0.1 μCi 100 μL liquid source

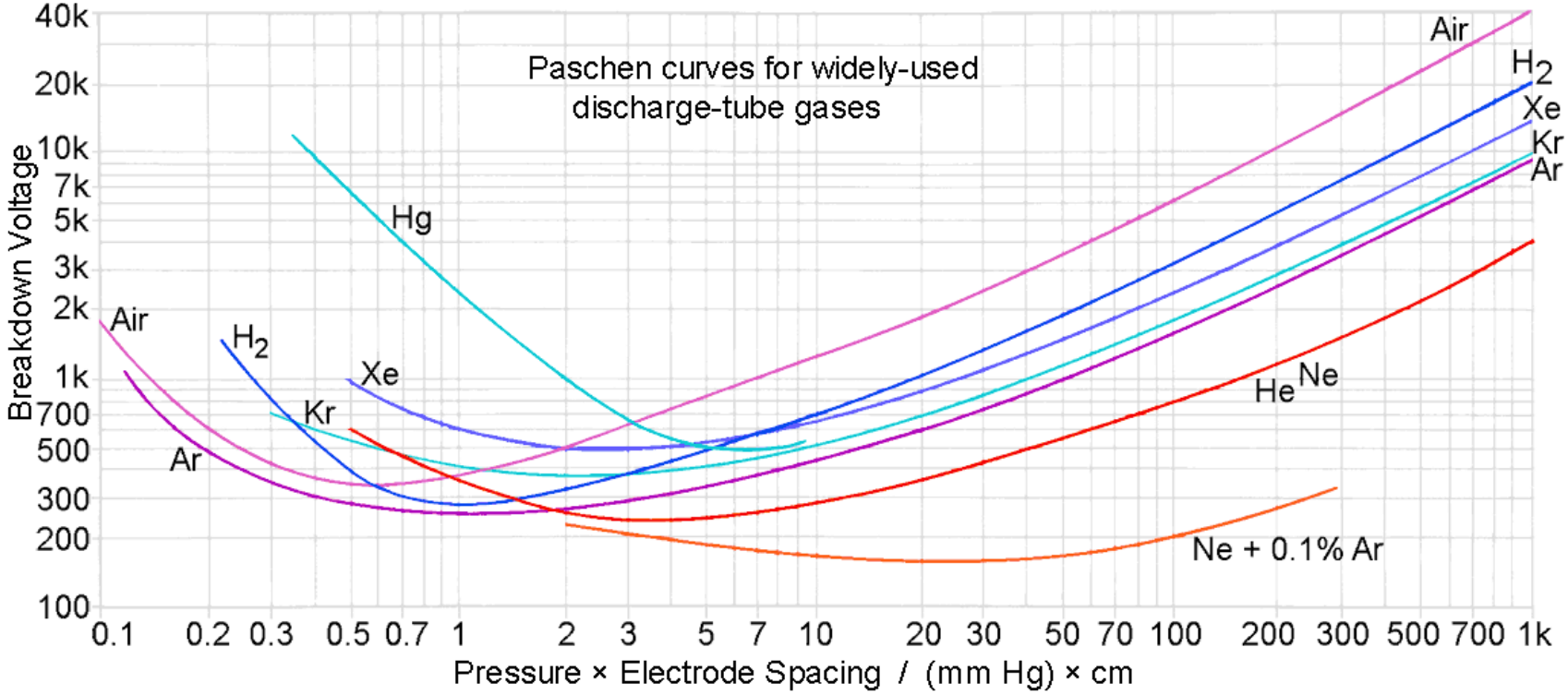

Figure 3.6. The Paschen Curves for electric breakdown for xenon, air and a few other gases. From Reference [81].

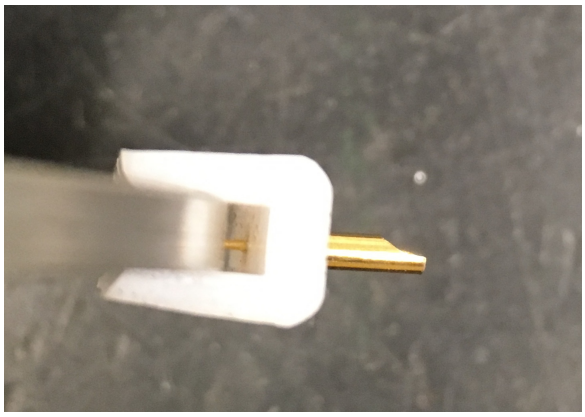

Figure 3.7. My electrode clamp connection, slightly unplugged. The piece fits the stainless steel electrode frame snugly when completely inserted.

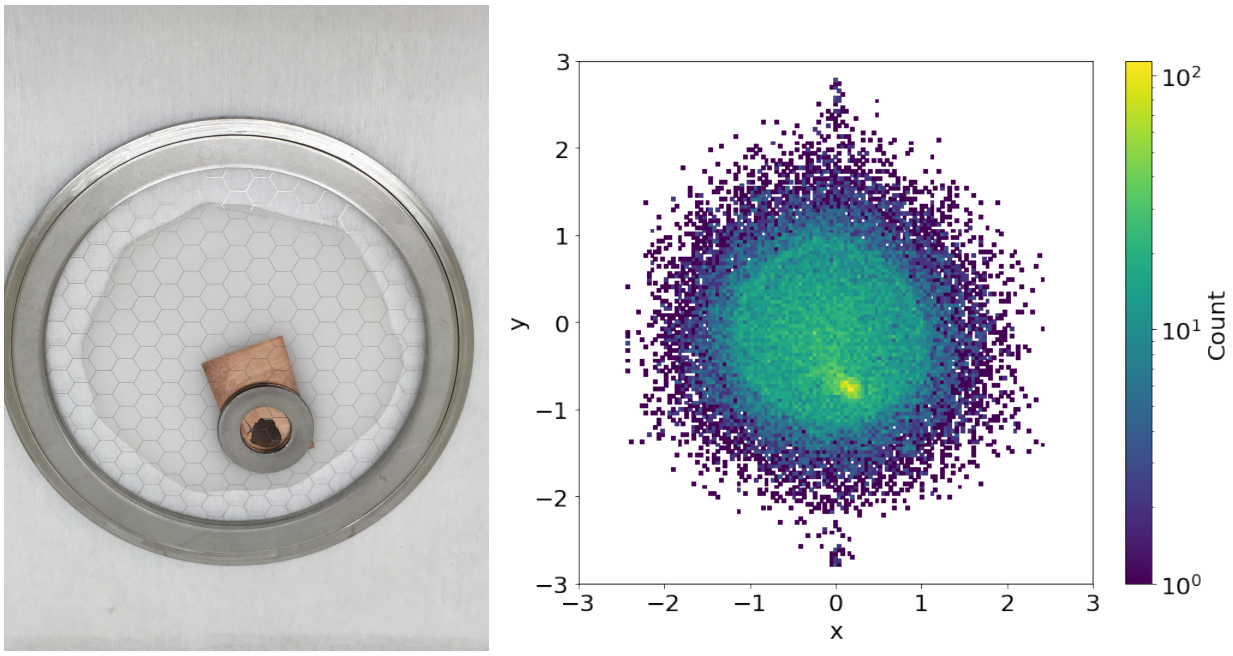

Figure 3.8. Polonium-210 deposited on the Cathode, and the location of the events in ASTERiX.

from Spectrum Technologies and the deposited activity was originally about 0.5 Bq. It was used for tests with the IR LEDs. As outlined in Section 3.6, the LEDs were replaced with a fiber-coupled laser, but the Polonium-210 had decayed away by the time the upgrades were finished. A Cobalt-57 gamma source placed outside the cryostat was used instead.

3.4 PMTs

Photosensors - a Haiku

To see light's quantum,
turn photon to electron.
Measure the current.

There are seven Hamamatsu R8520 PMTs arranged as in Figure 3.9. When I started the project, they were biased with a positive high voltage configuration on their bases' readout circuit. At the electrode configuration necessary to see single electrons, S2s from higher energy events were incredibly bright. The positive high voltage configuration for PMTs has a capacitor between the signal read-out and the positive high voltage. The signal's current

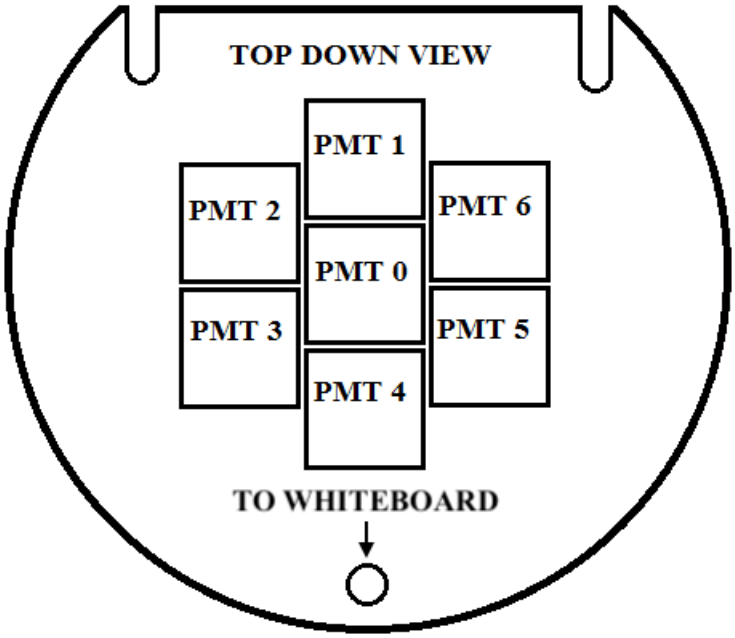

Figure 3.9. A top-down view of the PMT arrangement and Labeling scheme and orientation in the lab.

drew from the capacitor, and resulted in an overshoot of the baseline after the signal to recharge the capacitor. For giant signals, this overshoot lasted a very long time, and made us blind to single electrons that came directly after large S2s. It also made it difficult to accurately calculate the area in the peak when part of the integration was negative. Since that is the entire purpose of Chapter 4, this was unacceptable.

At first, I used much larger capacitors on the PMT bases, which seemed to work as in Figure 3.10. However, a high-capacitance surface-mount capacitor able to hold a 700 V difference in xenon does not commercially exist. Even if the capacitors worked in air, they would break with an audible pop in xenon, because of the behaviors in Figure 3.6. The capacitors were tested in argon because it has an even lower breakdown voltage than xenon. The only way to avoid zapping the capacitors was to coat them in Stycast epoxy. If they survived argon tests, then they were ready for xenon. Even then, there was a high likelihood for eventual failure. Ultimately, the PMT bias was switched to negative high voltage so the signal could be read directly off the ground without needing to be coupled over a capacitor. Such a setup completely avoided any overshoot.

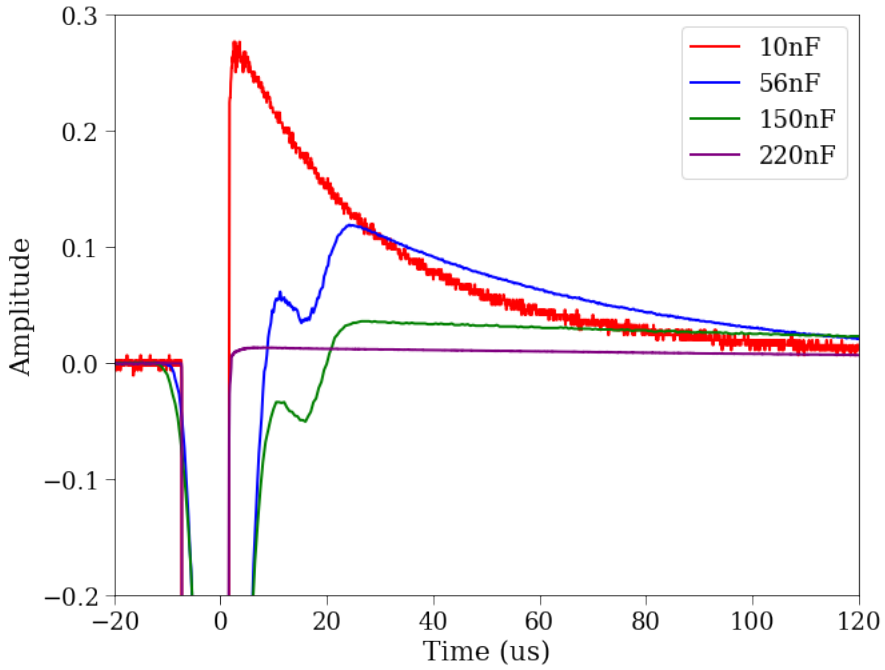

Figure 3.10. The PMT baseline overshoot after a signal with different capacitors between signal readout and high voltage.

Similarly to the Electrodes, the PMTs are powered with a Wiener high voltage module. The seven PMTs were controlled at first by a EHS8020p 8-channel 2kV-rated high voltage module. We then purchased the negative version of the same module, EHS8020n. Both the PMT and electrode modules were contained in a single controller that can be managed with a LabView program to turn on and off the PMTs and electrodes. The LabView program also monitors the voltages and currents in real time. A dangerous excess of light in the detector will be visible as any sudden feature in the PMT currents. A discharge between electrodes will be a large jump in affected channels' voltages and currents.

The PMTs' signals are amplified 10x by a NIM fan-out amplifier. One set of outputs is recorded by a CAEN V1724 digitizer, and the other set is summed in another NIM module and shown on the InfiniiVision DSOX3034A oscilloscope. The scope is vital for checking PMT behaviors. For PMT calibrations, there is a 405 nm violet LED embedded in the Teflon near PMTs 1 and 6. The Teflon acts as a diffuser of photons to all of the PMTs. The LED is flashed, using a Berkeley Nucleonics Corporation 505 pulse generator. The square wave of the pulse generator is too abrupt of a voltage change for the LED, so it is passed through a Thorlabs EF122 lowpass filter and split in 3 to go to the LED, the scope, and a logic NIM module. One of the negative logic outputs is sent as a trigger to the digitizer and another is shown on the scope.

During the PMT calibration, the pulser's mode period should be set to 0,001.000.00s for a 1 kHz rate and the pulse-width should be 50 μs. The output voltage necessary will be greater than 5.00 V. With the LED blinking, the scope will show the smooth signal sent to the LED, the square trigger sent to the digitizer, and a few photons in the PMT signals coincident with the LED waveform maximum. Data under these conditions can be used to calibrate single photons. The LED cable can be disconnected and this set-up maintained for an LED off noise run. The noise is subtracted from the calibration run with the LED on to best see the single photon signal area distribution. This conversion factor between integrated signal area and number of detected photons gives the unit of energy used for the scintillation light signals: Photoelectrons (PE).

Outside the detector, the PMTs have to be handled with gloves to avoid fingerprints on the photocathode. They are kept in a dark, sealed box in the back room 340A, and are

tested in the upgraded Dark Box. In 2019, a group of undergraduates outfitted a Pelican case with high voltage SHV and signal BNC couplings. The Dark Box seals closed and can be pumped down to a little less than atmospheric pressure and filled with argon to a little more than atmospheric pressure for an argon environment to test PMT bases. It is also light-tight to test PMTs themselves. PMTs should never be exposed to large amounts of light when on, which could break them. Also, if their internal vacuum seal breaks, gasses can enter resulting in afterpulsing, flashing, and an overall degradation in performance [82]. Helium is particularly harmful to PMTs, since it diffuses through the smallest leaks. Special care should be taken for them around the helium cylinder.

3.5 Obelix

DAQ - a Haiku

With a computer:
electric pulses make sense.
Without: well, good luck!

Viewing waveforms one at at time on the oscilloscope is not a firm basis for an analysis. The PMT waveforms are digitized and recorded in events by a CAEN V1724 digitizer with the program Obelix [83], running on a dedicated computer, zinc. Obelix is loosely based on CAEN's WaveDump software. For an LED PMT calibration, the digitizer is externally triggered to record when the LED is lit so that single-photon pulses for each PMT can be determined. For actual S1 and S2 data taking, a sufficiently large pulse of light in at least two PMTs triggers an event window to be recorded. Through Obelix, the duration of the event window can be set in a configuration JSON file. The threshold of light per PMT can also be set, and a lower zero-length encoding threshold, under which every signal can be set to zero to speed up readout and suppress electronic noise. The sampling rate of 100 MHz is ideal, although it can be decimated for improved performance. A percentage of the event window can record the time before the trigger which is temporarily stored in a circular buffer. The data in the circular buffer is overwritten if the trigger doesn't cause it to be written out.

Darryl got a majority of the data processing pipeline working before graduating, but I fixed a few bugs.

Firstly, the post-trigger event window percentage value of the configuration file was not being set for the data taking. I learned that for V1724 specifically, the digitizer needed a decimation value set, even if no decimation was required, before setting the percentage of the window to happen after the trigger. This was fixed relatively easily by following the digitizer's rigid order of setting parameters when initializing for data taking.

The other major problems came with handling the raw data output of Obelix to be processed by the XENON Collaboration's Processor for Analyzing XENON (PAX) [74]. PAX took a configuration file of the detector (with PMT placements, dimensions, PMT gains, and other parameters) and identified S1s and S2s. It also calculates the energy in PE of the S1s and S2s and the peaks' characteristics such as height, width, x and y position, and contributing PMTs. Then it forms interactions of S1s and S2s with calculated drift times. The zero-length encoding was not being correctly handled by PAX, so each PMT's waveforms were skewed in time depending on when they saw light. I corrected the timing when the baseline was recording zeros so the PMT's pulses lined up and peaks could be found. I also corrected a typo in PMT 4's x-location. Ultimately, I achieved a running system that could turn seven PMT's current waveforms into analyzable particle interactions.

A few features were developed to monitor detector performance before taking particle interaction data. There is a noise configuration of Obelix that is manually triggered. A noise data set containing 100 event windows is good for checking the electronic noise on the PMTs and the offset. The Noise Trigger Monitor python script analyzes the noise events, and gives the baseline, which should be 16000. If the values is higher than 16000, the PMT DC offset value in the configuration should be increased. If it is too low, the configuration value should be lowered. With the electrodes off, the number of pulses of a given size should decrease smoothly and sharply with pulse size, and be the same in every PMT. With the PMTs' baselines calibrated, one should do an LED calibration.

The LED configuration of Obelix should take an externally-triggered runs with and without the LED. The raw specialty AST binary files can be directly loaded into the calibration

Jupyter Notebook. This gives the PE gain of each PMT to set in the PAX ASTERiX configuration file. The LED set-up was described in Section 3.4.

With PAX and Obelix calibrated for the PMT's conditions, it is fine to take self-triggered particle interaction data. This data can be processed with PAX, and used to check the detector's performance. A Jupyter notebook is set up for quality control, looking for single electrons, checking the xenon purity with S2 size per drift time, or plotting the S2 width distribution in x and y, which should be uniform if the detector is level.

If the detector is not level (a clear gradient of widths across the detector), the three set screws that hold the detector above the Bosch frame can be adjusted. There are two near the whiteboard and one near the door to the lab, corresponding to the reference frame of Figure 3.9. If the S2s are systematically wider near PMT 1, then there is a larger gas gap there, and the set screw nearest the door needs to be loosened to lower that side of the detector slightly. Generally, mounting ASTERiX in the cryostat using a bubble level, and then using a bubble level to adjust the set screws is already very good leveling.

With 500 V between the Cathode and Gate, the maximum drift time in ASTERiX is about 10 μs. That means that a window of 3,000 ten-nanosecond samples with a post-trigger value of 60% is sufficient to observe full interactions. With a binary buffer, I originally chose 2^{12} = 4,096 samples, or 40,960 ns, for the event windows with the 60% post-trigger. The digitizer unfortunately requires significant dead-time between events to read them out before triggering on the next event. A new firmware designed for the XENON Collaboration eliminates this dead-time for the triggerless data of XENONnT, but ASTERiX's V1724 did not have this upgrade. Therefore, I eventually chose the maximum event window duration that the buffer could handle in order to have sufficient livetime after an interaction and see the desired electron backgrounds. The buffer could handle 2^{19} samples = 5.242880 ms windows, and I chose 99% post-trigger. Only now are all systems set to take the data, such as presented in Chapter 4.

Recently, I've learned that the buffer can be configurable, and is the main culprit for dead-time. In XENONnT, each PMT has a low trigger threshold and its waveform above threshold is saved individually with many smaller buffers. Therefore, zero-length encoding is not necessary because nothing is saved below trigger threshold and readout livetime is

essentially continuous. With each PMT having these small events above baseline, the data needs to be handled slightly differently to go back and synchronize pulses in an S1 or S2. The firmware is only part of the work for triggerless data acquisition. My understanding of this system was basic enough to get something working, although it is not ideal.

3.6 Infrared Light Modifications

Infrared Light - a Haiku

A millimeter
is a long wavelength for light.
It is infrared.

I ran ASTERiX to test a specific detector background of single electrons that I confirmed were spatially and temporally correlated with energetic particle interactions that had large S2s. Such single electron trains continue appearing long times after free electrons should have stopped. One hypothesis was that these electrons were trapped at the liquid surface and tunneled out after a long delay. The Schottky barrier at the surface, adjusted for extraction field, could be around 0.34 eV [84]. Another hypothesis is that electronegative impurities are trapping the electrons, but they eventually do escape to create these backgrounds. The most prevalent electronegative impurity is expected to be diatomic oxygen, with an electron affinity of 0.45 eV [85]. In either hypothesis, the bound electrons require less energy than is found in infrared (IR) light.

First, it was necessary to determine if the PMTs were blind to IR light in the Dark Box. Despite the low quantum efficiency at that wavelength, a high-intensity 950 nm LED (such as used in surveillance cameras) caused an excess of photon signals. Next, 1650 nm MTE5016-095-IR LEDs were tested, which still have 0.75 eV photons and can output one milliwatt. The PMTs were blind to this light.

To check that the IR LEDs were actually working and would work in the detector, a MTPD1346D-100 photodiode was used. The photodiode was amplified by a circuit using an LT1001 Operational Amplifier biased with +/- 12 V. An LED, attached to a thermocouple

and facing a photodiode, was slowly lowered into a dewar partially filled with liquid nitrogen. The signal ceased at roughly -120°C, which should work in liquid xenon (-93°C).

Three of these 1650 nm IR LEDs were installed in the bottom Teflon disk of ASTERiX, and two photodiodes placed in the top Teflon between PMTs, looking down into the detector. When all components finally worked, I took data to determine the effect of infrared light on the single-electron backgrounds.

When looking for these electron backgrounds after energetic Polonium-210 alpha decays, it became apparent that the digitizer had significant dead-time between events. However, I looked at the overall rates of these peaks. If the IR light reduced single electrons, then I should be able to quantify that. Also, perhaps the S2s of the Polonium-210 will be increased if the IR light photodetaches electrons from impurities or scatters with the electrons and prevents them from getting trapped at the surface for long. According to Figure 3.11, these effects on the single electron and Polonium-210 populations appeared to occur.

I later learned with the fiber set-up that the IR light was not actually suppressing the electron backgrounds. The heat load of the IR LEDs was likely changing the liquid level of the detector inside the Bell. Additionally, the LEDs' power output as read by the photodiodes appeared to degrade with time. I estimated the heat load of the LEDs and set the TPC heater, Pete, to output that wattage in an attempt to compensate for the heating during comparison runs when the LEDs were off. Even so, there is a slight increase in the single electron gain when the IR LEDs were on, characteristic of a lower liquid level. The fewer single-electrons are also a sign of a reduced extraction efficiency, since the electric field in the liquid is lower with less dielectric. I attempted to normalize this variation in gain out of the Polonium-210 events by comparing their S2s based on number of electrons. The resulting differences between the IR on and off runs were promising enough to try 1 Watt of infrared light using a fiber, but inconclusive.

With XENONnT being built at this time, and IR light looking promising, I requested that the fibers carrying light to calibrate the PMTs be broadband to also work for IR, or IR-friendly. I picked out FG105LCA low-OH doped silica fiber that had high efficiency for both 405 nm calibration light and 1550 nm IR light. For XENONnT, we ordered four fiber bundles,

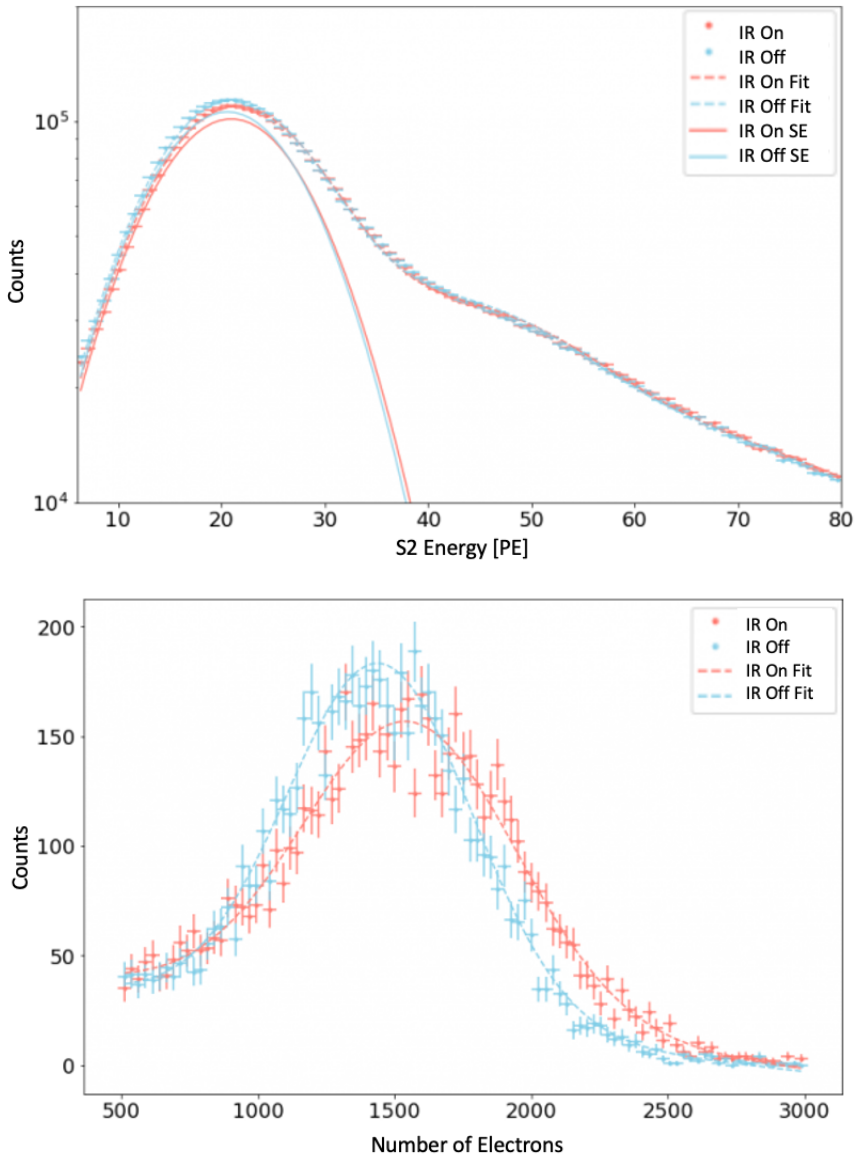

Figure 3.11. *Top:* The single-electron S2 population with IR light on and off. *Bottom:* The Polonium-210 S2 population with IR light on and off.

which each had seven 10-m strands fanning out from a single SMA 905 connector. Figure 3.12 shows these fibers being prepared for XENONnT. I also used this fiber in ASTERIX.

To achieve 1 Watt of infrared light, we borrowed an IPG Photonics EAR-1K-C-LP-SF fiber amplifier from Professor Daniel Elliott. Amy Damitz, a graduate student in his group, helped set it up, after which we took the photograph in Figure 3.13. A milliwatt ThorLabs S1FC1550 Fabry-Perot laser fed into the amplifier, which could then output between 0.2-1 Watt. Its wavelength was 1550 nm, a standard in commercial communication applications, rather than the 1650 nm previously used. A 1550 nm light photon has 0.8 eV of energy and initially the PMTs appeared blind to this wavelength.

At first, I tried a fiber strand connected on one end to an SMA connector and cut at the other, which fed into a small hole in the bottom of the detector. This configuration directed the full Watt of IR light directly onto PMT 0, and created an increase in single-photon signals in that PMT. To project infrared light throughout the detector, I used a different fiber with SMA connectors on both sides, and connected the end to a ThorLabs DG05-220-MD ground glass diffuser set in the bottom Teflon disk. With the diffuser, the Watt of IR light was not directed at any one PMT, and they did not observe any significant increase in single photons. This fiber and diffuser set-up was the final achieved for the data presented in Chapter 4.

3.7 Conclusion to A Small TPC for Experimental Research in Xenon

In this chapter, I have summarized the extensive work I undertook to bring ASTERiX to life as a working liquid xenon TPC. Specifically, a TPC sensitive to single electrons and with a data acquisition system that could turn the PMT pulses into something that I could analyze. Many of the problems briefly discussed were difficult to diagnose and required many attempts to solve. Even with an understanding of how things should be working, there were pieces that would inevitably break when closing, or pumping down to vacuum, or cooling down to liquid xenon temperatures. Even in the published data of Chapter 4, PMT 1 had stopped working after cooling down. I was able to operate with six PMTs, but many similar

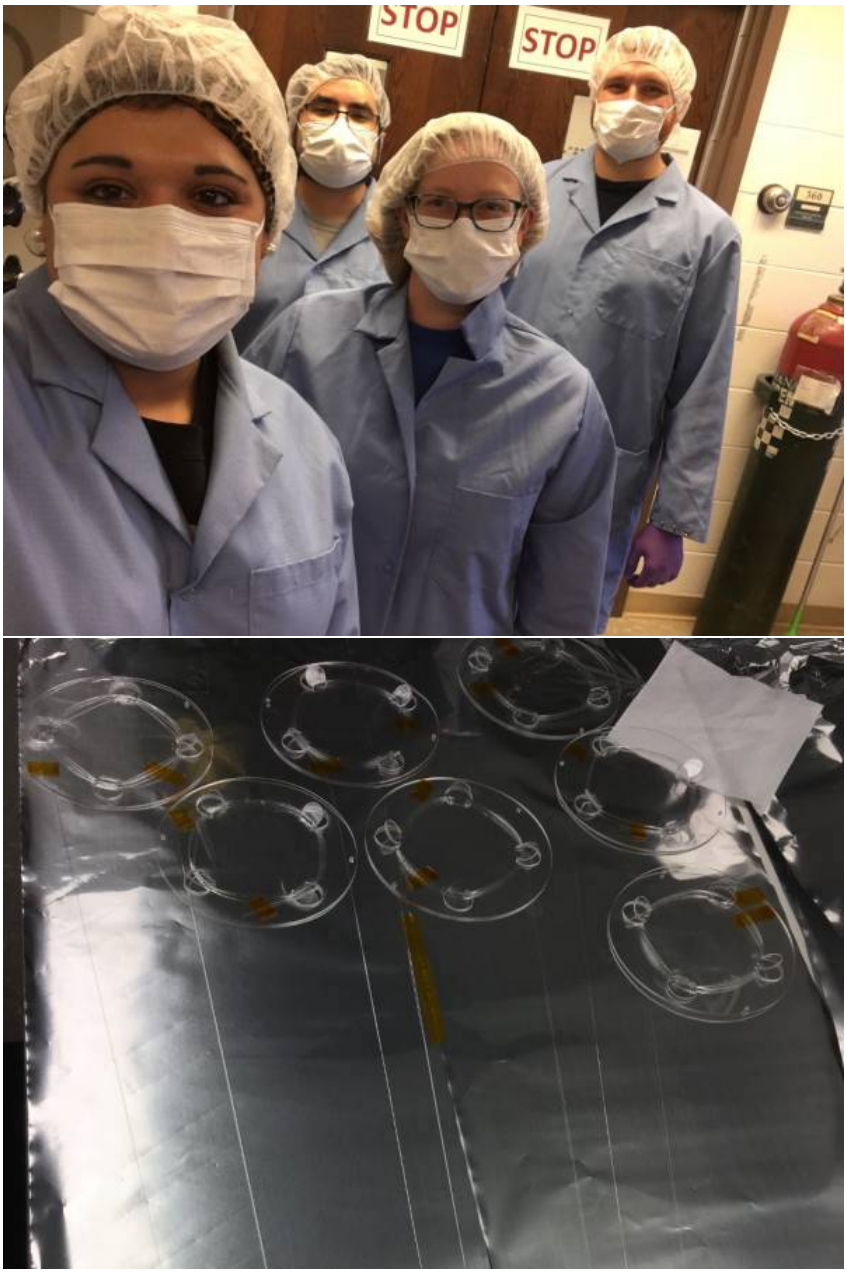

Figure 3.12. *Top:* The Crew from left to right: Amanda, Mike, me, and Mitch (an undergraduate). *Bottom:* A picture from untangling, cleaning, and preparing the IR-friendly fiber bundles for XENONnT.

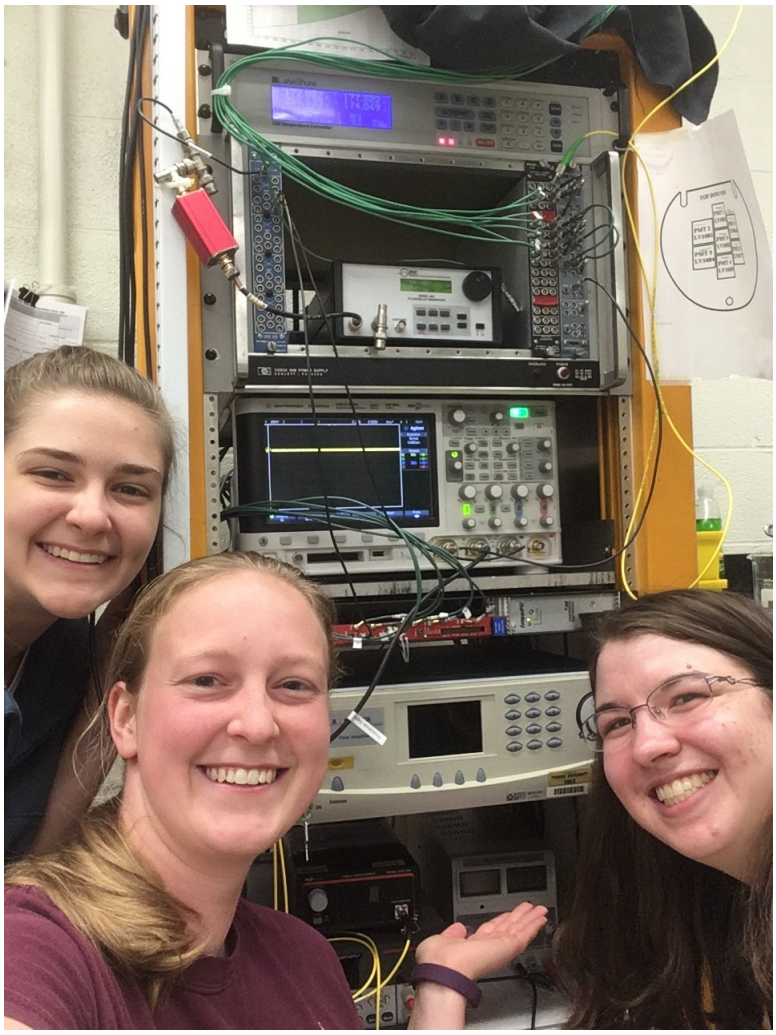

Figure 3.13. Installing the Fiber Amplifier and IR laser system. The laser is to the left of my hand, and the amplifier is above that. Left to right: Becks (an undergraduate), me and Amy.

set-backs often required me to open the cryostat, replace a wire that had disconnected, and close again.

The Bell was especially difficult to maneuver, because the TPC would need to be dismounted to lift the Bell comfortably to fix a PMT or electrode connection. The inflexible vacuum cables needed to thread down around the edge of the Bell and back up between the Bell and the cryostat wall to the switchboard. They had to be pulled tight enough to reach the switchboard and stay connected via flimsy connectors to the wires to the feedthroughs and outside, but loose enough not to break the wires where they were soldered to the PMT bases. Getting rid of the Bell vastly improved accessibility to fix components. However, the weir was never perfected, since it is too small of a volume to be particularly useful.

The level meter was inconvenient. Perhaps the capacitance readout circuit needed to be replaced since the offset changed so much when the electrodes tripped. Fluctuations of 2 mm are a lot for a xenon TPC, where even a slight level change can greatly affect the measured S2s as discussed in Section 3.6. The concentric cylinders with a small enough gap to have a high capacitance had a problem with capillary action, which also made the Vitalstatistix PID Bell heater control ineffectual. We discussed a parallel plate capacitor level meter just between the gate and anode. However, with the space constraints in ASTERiX, the required capacitance for the readout would need a potentially unfeasible number of plates, closely spaced in an interleaved comb structure.

Purity in ASTERiX was also a problem, leading to a low electron lifetime. S2s produced at the bottom of the TPC lost most electrons to electronegative impurities before the S2 signal was extracted into the gas and measured. The single-walled chamber volume at the top around the coldhead has a large temperature gradient in the gaseous xenon between the warm walls and the 172 K coldhead. The warmer components are expected to outgas more electronegative impurities, such as diatomic oxygen. Currently, the gaseous xenon returning from recirculation is piped into this volume, although close to the coldhead and directed toward a funnel. The funnel aids in catching liquid xenon dripping from the coldhead during cool down. Unfortunately, the mixing xenon gas could pick up impurities from the warm components outgassing and direct them down the funnel into the TPC. In the future it would make sense to direct the clean xenon from recirculation directly back down into the TPC,

without mixing in this volume. Additionally, reducing the amount of xenon to purify can help accelerate overall purification.

A potential upgrade I was not able to implement was to reduce the wasted xenon pooled at the bottom of the cryostat. We have an excellent chunk of copper, which would aid the reboiler heater and house both it and the corresponding PT100 temperature sensor. I even drew out the machining specifications. It would fit into that dead space and serve as the bottom of the TPC, supporting the first bottom Teflon disk. The methods by which I attained the dimensions of the bottom of the cryostat are infamous. I placed a plastic bag of Plaster of Paris in the bottom. I expected the plaster to set and then I could pull the bag out of the bottom of the 1 m cryostat. I was not aware that the plaster was exothermic, reducing the integrity of the bag, and causing the cryostat walls to expand, which the plaster flowed to fit. The result was that the plug of plaster was stuck in the bottom of the cryostat. Eventually to get it out, I used vinegar to dissolve some of the plaster, and had Jim help me crack a line down the middle with a sharp pipe, and pulled the plug out in chunks. The cryostat needed some serious cleaning after that, but was not ultimately harmed.

Throughout it all, I was able to build my resilience to frustration and gain incredible knowledge of these systems. From January to March of 2021, I worked at the Laboratori Nazionali del Gran Sasso in Italy, where I was invaluable to the commissioning of XENONnT. I am grateful that I have such a complete knowledge of these detectors from xenon-handling gas systems, through PMT and electrode electronics, to the data acquisition and analysis. As a bonus, I learned a decent amount about optics. Maybe one day I will design my own system and can implement other upgrades I was not able to accomplish, such as a larger weir, stronger cabling connectors, less wasted xenon pooled below the detector, a trustworthy level meter, channeling the clean xenon from recirculation directly into the TPC, and a triggerless DAQ.

4. SINGLE- AND FEW-ELECTRON SIGNALS

S2s - a poem

A flash of light from xenon struck, an interaction's sign,
heralds electrons drifting up to the liquid-gas line.
While traveling within a cloud, they reach terminal speeds
determined by electric fields, and xenon's properties.

The liquid xenon buffets them, diffusing them around.
They're pursuing the Anode's pull, seeking a place to ground.
But lurking in the xenon are impurities that wish
to catch electrons as they pass, as sharks waiting for fish.
To these electronegative impurities, one should
expect some electrons to lose, but are they gone for good?

The electrons that make it to the surface are not done.
They burst into the xenon gas, but is it every one?
Alas, if the extraction field is just a bit too weak,
Some cannot leave the liquid so they through the gas don't streak.
Trapped at the liquid interface in that layer, one should
expect some electrons to lose, but are they gone for good?

Electrons that have reached the gas cause luminescence bright
And photoionization frees more of them with light.
Measured or trapped, those die away, and none should now be found.
Yet still some electrons appear. Why is there this background?

A significant puzzle facing liquid noble element time projection chambers are high rates of single- and few-electron S2s. Although mostly studied in xenon TPCs, the rates are also high in argon TPCs such as DarkSide-50 [86]. XENON100 characterized photoionization electrons appearing within one maximum drift time after a bright S2, and recognized that overall rates were correlated with the concentration of electronegative impurities in the xenon [57]. Single-electrons trailing after high-energy events were observed in XENON10 for much longer than the maximum drift time, and have since been known as "electron trains" [56]. They appear in several detectors from small-scale test beds [87]–[89] to full-scale dark matter experiments such as LUX [90] and the XENON detectors. In this chapter, I will present my study of these electron trains in ASTERiX, which I published in the *Journal of Instrumentation (JINST)* with DOI:10.1088/1748-0221/16/07/p07014 [66].

4.1 Delayed Ionization Signals

I used a 122 keV Cobalt-57 gamma source to trigger energetic events in the liquid xenon. With event windows over 5 ms long, I was able to observe small S2 signals correlated with the primary Cobalt-57 interaction that continued for times two orders of magnitude longer than I expected for free electrons. The maximum drift time of an electron from the bottom of ASTERiX is about 10 μs.

Due to many changes to the system, the purity of ASTERiX was not very good for these data sets. There was a high concentration of electronegative impurities (usually dominated by diatomic oxygen) that capture electrons from the S2 as they drift to the top of the detector. The exponential decrease in electrons in the S2 with drift time has a time constant known as the electron lifetime. From Figure 4.1, I calculated an electron lifetime of 2 μs corresponding to an oxygen equivalent impurity concentration of ~200 ppb. This impurity concentration, N in ppb, depends inversely on the electron lifetime, τ in μs, as given in Equation 4.1. For units, the equation also requires the atomic mass of xenon (130 g/mol), its liquid density (3000 g/L), and the attachment rate constant of diatomic oxygen, which is about 10^{11}L/(mol·s) at the 500 V/cm drift field of ASTERiX. The attachment rate constant does not vary significantly between typical drift fields of 100-1000 V/cm [91].

$$N = \frac{10^{15} M}{\tau K_{O_2} \rho} \tag{4.1}$$

The data population fit in Figure 4.1 are the Cobalt-57 events that I eventually used as primary interactions. I made the event selections based on S2 area and drift time between the S1 and S2. An example event is shown in Figure 4.2. The S2 of the primary interaction is at 0.0 ms, and then all trailing S2s in the event are shown. There is a large background of single- and few-electron S2s that appear at times beyond the maximum drift time of 10 μs, indicated by the dashed line.

The S2 area spectrum of these electron trains is shown in Figure 4.3. To completely avoid photoionization backgrounds, which extend to the maximum drift time after the bright S2 and may have secondary echoes, the small S2s are required to be at least 3 drift times (30 μs) after the main S2. I then chose the purest populations of 1, 2 and 3-5 electron S2s, denoted

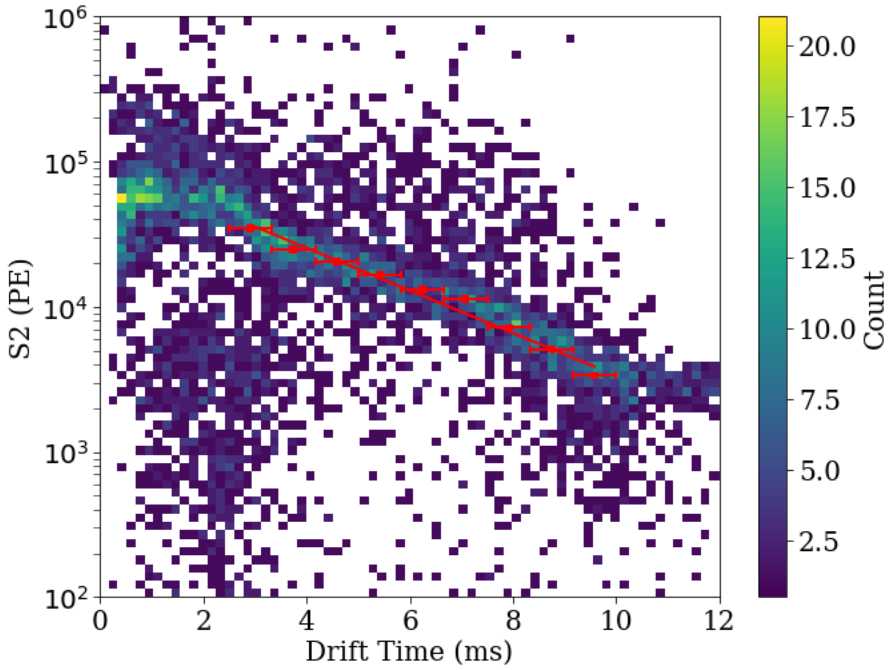

Figure 4.1. The Cobalt-57 events' S2s in ASTERiX exponentially decrease in measured size with drift time due to electrons being lost to electronegative impurities. The electron lifetime is 2 μs.

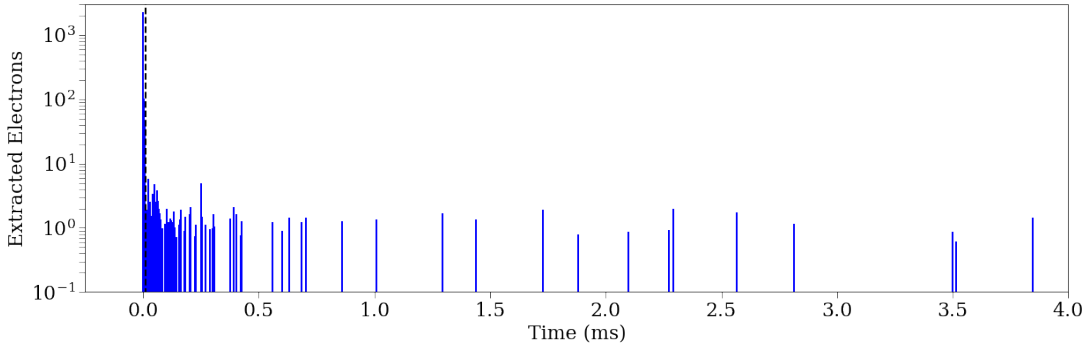

Figure 4.2. An example Cobalt-57 event, with electron signals appearing for milliseconds afterward. This graph shows the central time locations of all reconstructed S2s in the event window and their electron multiplicity. The primary interaction's S2 is at 0.0 ms. The maximum drift time of electrons in ASTERiX is 10 μs, represented by the dashed line.

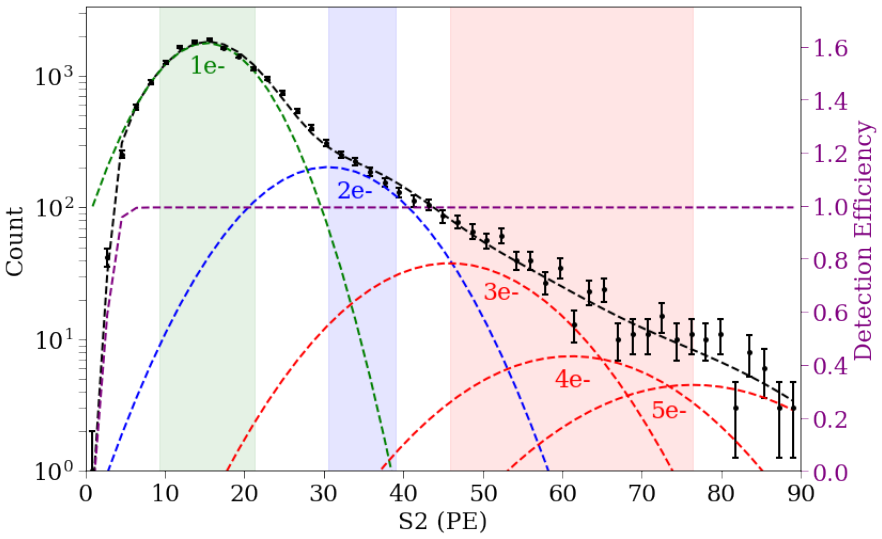

Figure 4.3. The spectrum of small S2s in the electron trains following over 30 μs after accepted Cobalt-57 primary interactions. Gaussians were fit to each electron multiplicity, and the shaded regions denote the S2 energy ranges used for the singe-electron (green), double-electron (blue), and 3-5 electron (red) populations.

by the shaded regions, to study the behavior of different S2 electron multiplicities. The single-electron gain is 15.3±0.1 PE for the Anode biased at +5 kV and the Gate biased to -5 kV.

Since I was interested in small S2s up to five electrons, any S2 larger than six electrons (∼90 PE) could be a primary interaction that causes these backgrounds. To avoid peaks incorrectly split by the processor and to deal with potential multi-scatter events, I lumped consecutive large S2s within a drift time together. I took their sum size and the weighted average of their timestamps as a single primary interaction S2. Such a correction does not affect the behavior of the backgrounds over 30 μs afterwards. With the primary interactions' times and sizes established, I matched all of the smaller S2s with the primary interaction that came before it and measured the livetime windows until the next primary or the end of the event window. I then wanted to ensure that the electron trains I was studying were from the current primary interaction, and not from a larger primary interaction that came just before. Therefore, I implemented an overlap cut as shown in Equation 4.2 where an accepted primary interaction's size needed to be greater than ten times the previous primary interaction's size

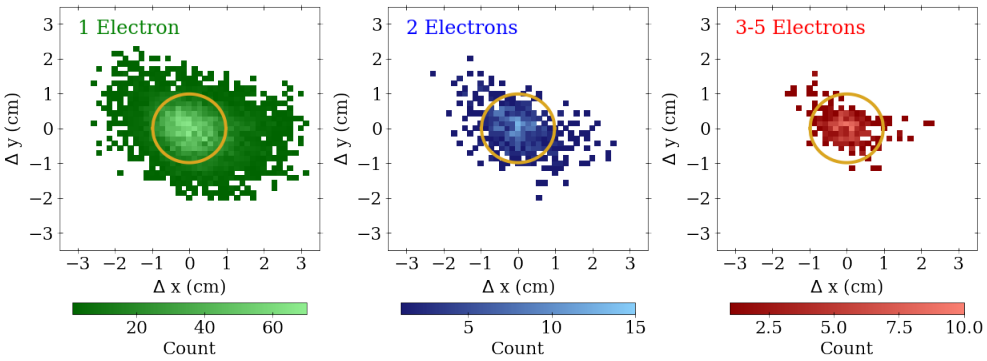

Figure 4.4. The displacement of signals from the primary interaction location for single-electron, double-electron, and 3-5 electron populations (left to right). The gold circle denotes the radius 9.9 mm, containing 80% of the position-correlated single-electron populations, and ∼70% of all electron train S2 signals.

exponentially decreased over the previous primary interaction's livetime window $w_{\mathrm{i}-1}$ with a time constant of 1 ms. With all primary interactions and their trains and livetime windows constructed, I selected the Cobalt-57 events and their trains that passed the overlap criteria.

$$S2_{\mathrm{i}} > 0.1 \cdot S2_{\mathrm{i}-1} \cdot \mathrm{e}^{-w_{\mathrm{i}-1}/[ms]} \tag{4.2}$$

From the population selections in Figure 4.3, the reconstructed positions of the S2s in these populations relative to the position of the primary interaction can be determined. This displacement, shown in Figure 4.4, favors the same location as the primary interaction. From a simulation of random possible electron train locations matched to a random primary location, the random coincidence background can be estimated. I then used that to form a coordinate transformation from Δr to where that background was flat, which we called $\tilde{d}$. I transformed the true data Δr of electron train single-electron S2s to primary interaction locations and subtracted the flat component. Then I chose the $\tilde{d}$ value containing 80% of the remaining position-correlated backgrounds. This corresponded to a radius of 9.9 mm, and about 70% of all matched electron train S2s. This radius was also applied to the double-electron and 3-5 electron S2 populations.

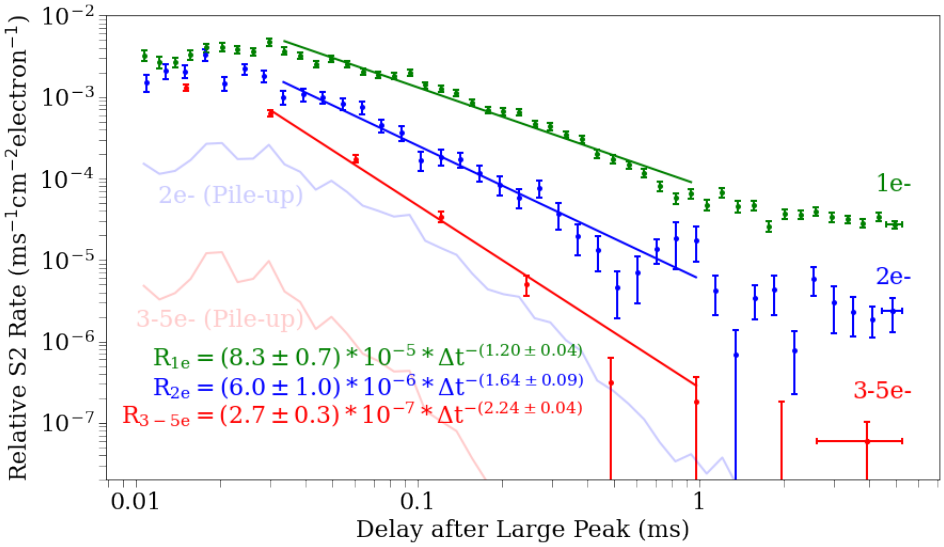

Figure 4.5. The evolution of the rates of position-correlated single (green), double (blue) and 3-5 (red) electron signals after a Cobalt-57 interaction with time. They are normalized by the position-correlated area of 9.9 mm radius, and the number of electrons produced in the primary interaction (corrected for electron lifetime and drift time). The horizontal error-bars of the last data point in each series illustrate the bin ranges. The expected contribution from pile-up is indicated for the double (light blue) and 3-5 (light red) electron signals.

By this time, I had matched all S2s smaller than six electrons to the S2 larger than six electrons that came before. I avoided overlapping electron trains from previous large events and selected my Cobalt-57 primary interactions and their livetime windows that contain their electron trains. I selected the purest populations of single, double, and 3-5 electrons in the trains, particularly observing that the vast majority were position-correlated to the primary interaction, and selecting those. I can now construct how the rates of these populations depend on time, which is found to be power-law-like and shown in Figure 4.5. I fit a power-law $R = A \cdot t^b$ using a maximum likelihood [92], and found that the power-law power of $b = -1.2 \pm 0.04_{stat}$ is consistent with other studies [88], [90].

From Figure 4.5, it can be seen that the double and 3-5 electron populations are not due to pile-up of single electrons. The coincidence window for simultaneous single electrons to be grouped together into a single S2 is less than a microsecond. I assumed a Poisson

process with a rate R of single-electron signals. The probability of observing a coincidence time window t with n-electron pile-up S2s is given below in Equation 4.3.

$$P(n|R \cdot t) = \frac{(R \cdot t)^n}{n!} \mathrm{e}^{-R \cdot t} \tag{4.3}$$

Therefore, the rate of pile-up R_n to form an n-electron S2 is related to the rate of single-electron S2s R_1:

$$R_n = \frac{(R \cdot t)^n}{n!} R \cdot \mathrm{e}^{-R \cdot t} = \frac{(R \cdot t)^{n-1}}{n!} R_1 \tag{4.4}$$

When the total rate R in a sufficiently small coincidence window has an expectation value less than one, the single-electron rate dominates R. In the case of the double-electron S2s from pile-up, their rate R_2 can be approximated in terms of the single-electron rate:

$$R_2 = \frac{R_1^2 \cdot t}{2} \tag{4.5}$$

By this expectation for pile-up, and taking into account the normalization factors for position-correlation area selection within a 9.9 mm radius and the number of electrons produced in the Cobalt-57 primary interaction of typically 10^4 electrons, the double-electron S2 contribution from single-electron pile-up is an order of magnitude below the measured double-electron signal rates. Additionally, the double-electron power b would necessarily be twice that of the single-electrons, since the pile-up rate roughly scales as R_1^2, which is not consistent with my observations.

Regarding contamination, the single-electron Gaussian tail contamination in the double-electron population is less than 10%. Since the double-electron rates are within an order of magnitude of the single-electron rates and the powers are different, I concluded that these are true double-electron signals, and not from single-electron contamination or pile-up. The same arguments apply to the 3-5 electron populations, indicating some mechanism that can produce delayed, position-correlated signals with different electron multiplicities.

By integrating the rate plot, I calculated the number of electrons appearing in this electron train from 30 μs to 1 ms, and found the typical number as a fraction of the total number of electrons produced in the primary S2. The power b and amplitude A have significant covariance, and the power law is not a perfect fit. Forcing the typical power b, the amplitude

A is analogous to the typical number of electrons per electron-multiplicity population in the electron train. My goal is to reduce this background, so I compared this fraction of measured signals, normalized by the primary interaction size, for different detector operating conditions.

4.2 Effect of Extraction Field

With the Cathode and Gate biased to -5.5 kV and -5 kV respectively, data was taken while varying the Anode voltage from the default +5 kV down to +1 kV in 1 kV steps. A 15-minute data set was taken at each Anode voltage, allowing the detector to settle for 10 minutes after changing the bias voltage and before taking data. The five corresponding extraction fields just below the liquid surface were estimated to be 5.9, 5.3, 4.7, 4.1, and 3.5 kV/cm for the 1 cm electrode spacing and the liquid level being 2.5 mm above the Gate. The electrodes were approximated as a parallel plate capacitor partially filled with a dielectric liquid, $\kappa = 1.85$ [59], to convert from applied voltage to electric field.

If the small S2 electrons were remnants of the S2 trapped at the liquid-gas interface, I hypothesized that a better extraction efficiency from higher extraction fields would cause the electrons to be emitted faster and make the power b more negative. I did not find this to be the case: the power law only significantly changes in amplitude A, not power b, despite the extraction efficiencies ranging from 50% to 95% [60].

The left plot of Figure 4.6 shows that the number of single- and few-electron signals increases with increased extraction field and extraction efficiency. The linear trend with extraction field supports that observed by Sorensen and Kamdin in the amplitude of their slow exponential component [93]. The slopes of the lines of best fit are $(97 \pm 2) \cdot 10^{-5}$, $(47 \pm 3) \cdot 10^{-5}$, and $(23 \pm 1) \cdot 10^{-5}$ $(\text{kV/cm})^{-1}$ for the single, double and 3-5 electron populations respectively. They show how the fraction of electrons in the trains relative to the number of electrons produced in the primary interaction depends on the extraction field in the liquid. Their intercept at 1.5 kV/cm is consistent with the threshold field required to extract electrons [60]. The linear effect also appears consistent with the recent findings in the PIXeY research detector, although they do not perform any fits [89].

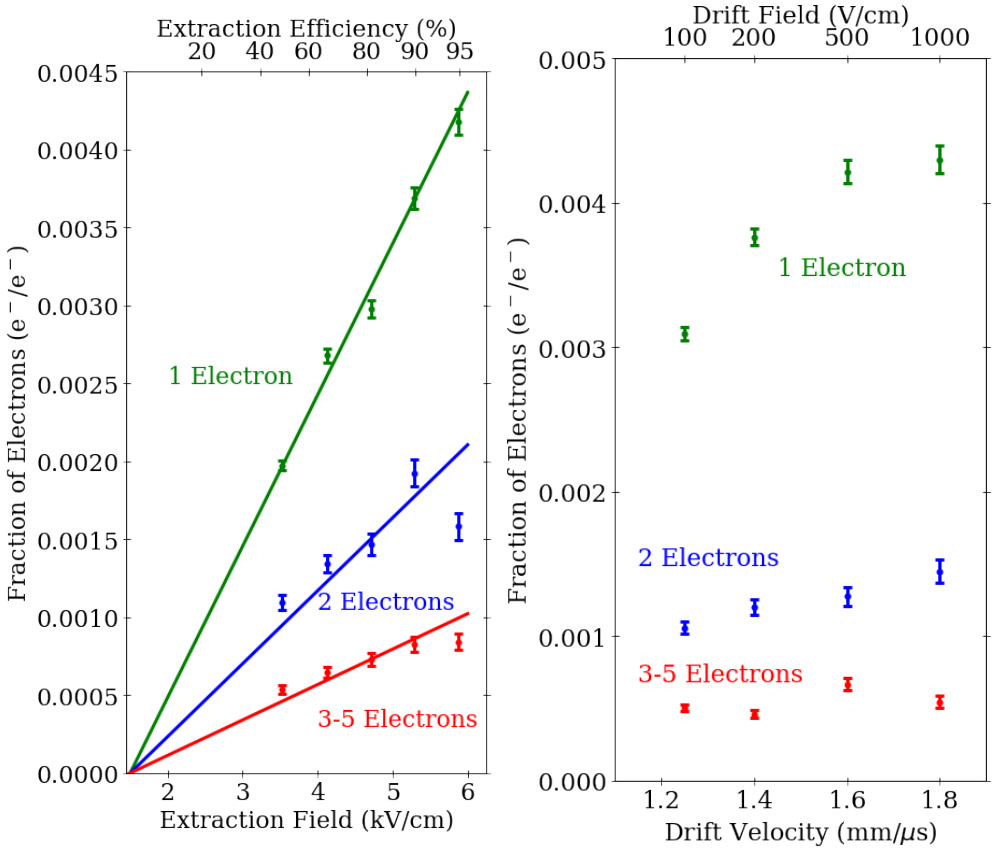

Figure 4.6. The number of electrons between 30 μs and 1 ms in single (green), double (blue) and 3-5 (red) electron signals as a fraction of the number of electrons produced in the primary interaction, corrected for electron lifetime and drift time. The *left* plot shows this fraction's dependence on different extraction fields (bottom x-axis) and electron extraction efficiencies (top x-axis). The *right* plot shows this fraction's dependence on different electron drift velocities (bottom x-axis) and drift fields (top x-axis).

Despite different electron extraction efficiencies with different extraction fields, the rates of single and few electron signals maintain the same power b. However, the amplitude A and therefore the total number of small signals increases directly with increased extraction field. I found it striking that the increase is linear with extraction field and not extraction efficiency.

4.3 Effect of Drift Field

With the Anode set to the default +5 kV, the Cathode bias voltage was varied between -6 kV and -5.1 kV corresponding to drift fields of 1000, 500, 200 and 100 V/cm. Again, 15-minute data sets were taken for each field, after 10-minute relaxation periods following changes to the detector conditions.

With increased drift field, I hypothesized that the electron power law could be steepened and the fraction reduced if the dominating mechanism is electronegative impurities trapping electrons and releasing them at later times. The increased kinetic energy should make electrons less likely to become trapped or allow them to be released more quickly. For these data sets, the electron lifetime does not change with drift velocity. However, at lower fields, more electrons are lost to electronegative impurities for events near the bottom of the detector due to the longer drift times for a given distance. The power law amplitude A increases with increased electron drift velocity, particularly for the single electron population, but still does not change the power b. The drift velocities agree with Reference [94].

The right plot of Figure 4.6 shows that the number of single-electron signals increases with increased electron drift velocity. The number of double- and 3-5 electron signals do not exhibit a strong correlation. The measured electron lifetime in ASTERiX for all of these data sets was 3 μs, which indicates a high concentration of electronegative impurities [57], [95]. Electronegative impurities are expected to only bind to a single electron each, and the fact that an effect is clearest in the single electron population indicates a potential effect from purity.

With faster drift speeds, the measured S2 size is slightly larger, due to fewer electrons lost to the lifetime and a larger total charge yield. Therefore, the typical electron lifetime

correction applied to the measured S2 size to calculate the number of electrons produced in the initial interaction decreases with increased drift field. Removing this correction, applied to the denominator in the right plot of Figure 4.6, I found rather a decrease of these relative backgrounds with drift field. This is consistent with Reference [89], which had a detector with an electron lifetime longer than the maximum drift time, and did not apply electron lifetime S2 corrections. This nuance indicates that the measured size rather than the produced size of the primary interaction's S2 has an effect on the behavior of the electron trains.

4.4 Effect of Primary Interaction Depth

Two 15-minute data sets taken four hours apart at default detector conditions (+5 kV Anode, -5 kV Gate and -5.5 kV Cathode) are consistent with each other, so I was pleased with the detector stability. With these higher statistics from 10,218 event windows of data, I chose Cobalt-57 events from different depths in the 1 cm detector volume below the Gate. Based on the location of the source, most events were near the bottom of the target volume. The fractions of the single- and few-electron signals relative to the number of electrons produced in the primary interaction, and relative to the number of electrons measured uncorrected for lifetime, are shown in Figure 4.7.

If the electron trains were dominated by delayed emission from impurities, then the fraction should always be larger at deeper positions because there are more impurities in a longer drift column to catch and release electrons. This was the observation in LUX [90].

If delayed emission from the liquid surface dominates, the effect of drift time on the fraction is more complicated. S2s from deeper in the detector are smaller when they reach the interface because of the electron lifetime. Therefore, I expected them to be able to leave fewer electrons at the surface compared to the number of electrons produced in the original interaction and thus have smaller fractions. This appears to be the case in the left plot of Figure 4.7. However, S2s from deeper in the detector are also spatially larger and less dense due to diffusion, which could affect electron emission processes of the liquid-gas interface, increasing the fraction compared to the measured S2. Diffusion area is linearly dependent on time. In the right plot of Figure 4.7, the fraction is taken relative to the number of electrons

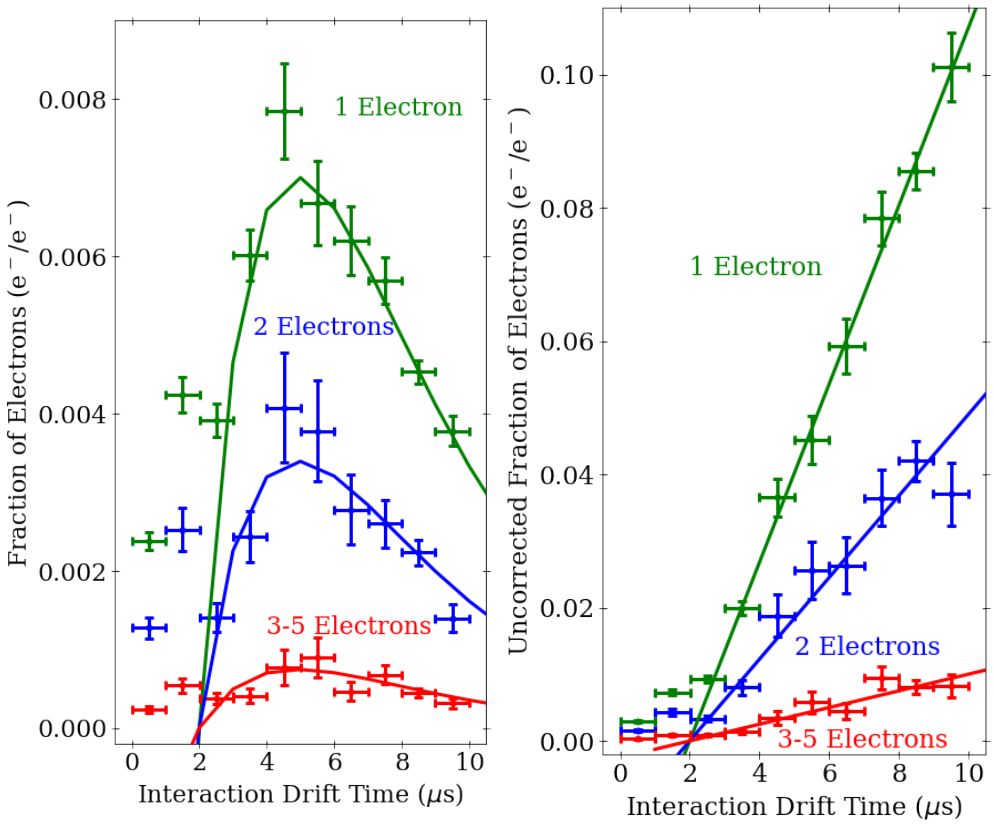

Figure 4.7. The *left* plot shows the number of electrons between 30 μs and 1 ms in single (green), double (blue) and 3-5 (red) electron signals as a fraction of the number of electrons produced in the primary interaction, corrected for electron lifetime, at different depths in the detector. The *right* plot shows the same number of electron signals per population, but as a fraction of the number of measured S2 electrons, without correcting for electron lifetime. The liquid level is 2.5 mm above the gate, giving a drift time above the Gate of ~ 2 μs.

left in the S2 when it reaches the surface, which is the measured S2, uncorrected for electron lifetime.

The slopes of the lines of best fit for how the fraction of trailing electrons relative to the uncorrected measured S2 depend on drift time are $(133 \pm 2) \cdot 10^{-4}$, $(61 \pm 4) \cdot 10^{-4}$, and $(12 \pm 1) \cdot 10^{-4}$ $(\mu s)^{-1}$ for the single, double, and 3-5 electron populations respectively. The intercept at 2 μs is the location of the gate, and indicates a discontinuity consistent with the discontinuity in the electric fields and drift velocities. The left plot corrects for the exponential electron lifetime. The lines of best fit are therefore the same but multiplied with the decreasing exponential electron lifetime factor that is applied to the primary interaction S2 in the denominator of the fraction.

This study cannot exactly disentangle whether overall smaller S2s, perhaps from less energetic interactions, cause proportionally larger trains, or whether S2s from deeper in the detector would cause larger trains. The fraction is linear rather than exponential with depth, which favors a depth dependence rather than an S2 size dependence, since the measured size of the S2 drops exponentially with drift time.

4.5 Infrared-Light Stimulated Emission

In an effort to determine if these backgrounds were due to impurities, I irradiated the detector volume with 1 W of infrared light (1550 nm), corresponding to a photon energy of 0.8 eV. This was discussed in Chapter 3. I tested and confirmed that the PMTs are blind to this long wavelength, so the IR light was left on for the duration of data taking. The most common electronegative impurity is expected to be O_2^-, which has an electron affinity of 0.45 eV [85] and a photodetachment cross-section at this photon energy of about 10^{-19} cm^2 [96]. It is likely that the relative affinity is lower and the cross-section is higher, since the ions in the detector are in an electric field. At 1 W, there is a photon density coverage of one per $\sim 5 \cdot 10^{-15}$ cm^2 in a millisecond, ignoring the high reflectivity of the PTFE walls. The relative fraction of O_2^- impurities undergoing stimulated photodetachment per millisecond is conservatively estimated to be $2 \cdot 10^{-5}$. This is not as small as one might think.

I think there is a significant equilibrium concentration of O_2^- built-up. The drift velocity of O_2^- under the default detector conditions is 0.4 cm/s [97]. By Einstein's Relation, the diffusion coefficient of O_2^- is on the order of 10^{-5} cm^2/s. The ions take seconds to reach the liquid surface, and days to diffuse from the middle to the edge of the detector. Meanwhile, thousands of electrons are being lost per Cobalt-57 interaction due to the electron lifetime and tens of interactions are happening per second. Based on the number of electrons in the trains relative to the number of electrons lost to the electron lifetime, it appears that nearly all electrons caught on impurities are lost forever, and are never extracted and measured. From the electron lifetime, the O_2 equivalent concentration of neutral, electron-accepting impurities can be calculated [57] per Equation 4.1. In the case of ASTERiX, it would be about 200 ppb and approximately 10^{17} impurities in the volume of ASTERiX. Therefore, despite the low photodetachment cross-section, 1 W of infrared light should significantly increase at least the position-uncorrelated single electron rate in the time region of interest from 30 μs to 1 ms.

A typical Cobalt-57 event producing 10^4 electrons halfway down the detector would lose about 80% of the electrons. But with less than 10^4 freshly caught electrons, the infrared light could have a negligible affect on position-correlated electron train events, if they are re-emitted electrons from that primary S2. The photodetachment cross-section makes the effect of one more electron from IR light subdominant to whatever mechanism could be causing these position-correlated electron trains.

Table 4.1 lists the fraction of electrons in the signal populations relative to the number of electrons in the initial primary S2. I observed no significant effect with infrared light, except for the position-uncorrelated single electrons. This corresponds to an increase of about 20 more electrons in 1 ms and could indicate an O_2 equivalent population of about a million in the $\sim$150 g detector. Such a number of negative ions would be produced in less than a minute in ASTERiX, so there must be a mechanism neutralizing most of these ions other than diffusion to the wall to prevent them from building up and causing significant changes to the electrodynamics and even the operation of the detector. Neutralization on the Gate electrode is one of the most likely possibilities.

Table 4.1. The fraction of single, double, and 3-5 electron signals from 30 μs to 1 ms after a Cobalt-57 event compared to the total number of electrons produced in the primary interaction, corrected for electron lifetime and drift time, with and without 1 W of infrared light. Position correlated events are within 9.9 mm of the primary interaction, and the uncorrelated events are outside this radius.

	Position Correlated (10^{-5}e$^-$/e$^-$)	Position Uncorrelated (10^{-5}e$^-$/e$^-$)
Single Electrons IR ON	402 ± 8	127 ± 3
Single Electrons IR OFF	416 ± 7	109 ± 3
2 Electrons IR ON	157 ± 7	16 ± 2
2 Electrons IR OFF	141 ± 7	16 ± 2
3-5 Electrons IR ON	140 ± 7	13 ± 2
3-5 Electrons IR OFF	129 ± 6	14 ± 2

4.6 Conclusion to Single- and Few-Electron Signals

I investigated single- and few-electron background signals in ASTERiX that extend after an energetic interaction for times at least two orders of magnitude longer than the maximum electron drift time in the detector. These are strongly position-correlated to their primary interaction and their rates evolve as a power law with time. No detector condition that I investigated significantly altered the power law exponent b; changing parameters only increased or decreased the overall amplitude. Most of what I discussed here is in my paper [66].

The relative fraction of the measured electron trains compared to the number of electrons produced in the primary interaction is in total less than 1% of those electrons produced in the interaction. The short electron lifetime of ASTERiX meant that 95% of electrons from deep in the detector were lost while drifting. A ^{57}Co event near the cathode would produce $\sim$ 10,000 electrons, of which only about 1,000 would be detected in the primary S2, but $<$ 50 electrons would appear in the train.

My findings argue against the conclusion that these signals are dominated by electrons from the primary interaction that are caught and later released by impurities. Typical impurities only capture single electrons, and I observed few-electron signals at rates above what is expected by coincident single-electron pile-up. The fractions do not increase linearly with extraction efficiency, which would be expected if the electrons were caught on and released by impurities in the bulk liquid below the gate. For a constant drift field, a constant number of re-released electrons from the bulk would only be affected by the changing extraction efficiency when they reach the surface from changing the extraction field. Also, all populations increase linearly with extraction field, not just the single electrons.

The increased fraction of the single-electrons with drift field might indicate that more electronegative impurities released their electrons at first glance. PIXeY observes an opposite trend [89], with which my data is only consistent when I took the fraction compared to the measured S2 rather than the produced S2 size, accounting for the electron lifetime and drift time. With an electron lifetime shorter than the maximum drift time in ASTERiX, I could disentangle that these electron train dependencies are more related to the measured S2 size

rather than the S2 size produced in the bulk xenon drift region. This key distinction builds on previous results [89], [90], [93], and points to an effect at the liquid surface rather than electronegative impurities catching and releasing electrons in the drift region. The rigidity of the power b–despite the expectation that electronegative impurities drift faster with a higher drift field and therefore should disappear more quickly [89]–additionally argues against an effect in the bulk.

Although more electrons are lost to electronegative impurities deeper in the detector, the fraction of electrons relative to the electrons produced in the primary does not strictly increase with increased depth of the primary interaction. Rather, the fraction of electrons in the train relative to the number of measured electrons–which is reduced according to the exponential electron lifetime with depth–increases linearly with primary interaction depth. Again, since the S2 is measured at the surface, the trend with measured S2 rather than the number of electrons produced at the interaction site points toward an effect at the surface. Attempting to induce photodetachment with infrared light does nothing, except potentially validate the theory of photodetachment by increasing position-uncorrelated single electrons. From a simple estimation of rates, it appears that an overwhelming majority of impurities that capture electrons do not release them.

The observations that the electron backgrounds increase linearly with extraction field, that the few-electron signals cannot be coincident single electrons, that the effects depend more on measured S2 size than S2 size produced at the interaction site, and that the power law power b does not change, all indicate an effect at the liquid surface. Perhaps unextracted electrons pool just below the liquid surface. Their initial cross-sectional area from their primary S2 could be determined from diffusion, which depends linearly on drift time. A surface charge density proportional to the extraction field would be expected at this dielectric surface. I also expect a layer of electronegative impurities that have drifted to the surface, and which do not have a mechanism of neutralizing, to affect the surface electrodynamics. In this case, there would be an effect of purity, but acting at the liquid surface.

The electron cloud bursting through the surface could cause mechanical ripples of the liquid that change local electric potentials. This would increase collisions in the impurity layer and/or cause points where a few electrons can be emitted from the unextracted pool or

the rapidly changing surface charge density. The relaxation of the liquid ripples should not be affected by electric fields, infrared light, or where the cloud originated in the detector, and could explain the power law. A continuous sum of exponentially distributed exponentials can appear as a power law [98], so damped sinusoidal ripples with exponential probabilities of electron emission with different multiplicities is a promising explanation. We plan to run ASTERiX again to test this with an ultrasonic transducer mounted on the outside of the detector to induce ripples.

The density of these charge reservoirs would directly depend on extraction field. They could be affected by a build-up of electronegative impurities, which would be reduced with better purity. The overall charge density would directly depend on the density of the S2 when it reaches the liquid-gas interface, particularly the number of electrons and the cross-sectional area. The detector conditions determine the effect of the depth of the interaction: a smaller incident S2 would have a smaller number of electrons in the train. A larger cross-sectional area from diffusion could increase the amount of delayed, thermalized electrons at the surface as proposed by Sorensen [84]. Increased drift velocity could cause an increase in the electron trains, since the initial charge yield increases and the typically shorter drift times reduce the effect of the electron lifetime, both of which lead to overall larger measured S2s in primary events. Because of this, the number of electrons in the electron trains relative to the uncorrected, measured S2 size decreases with drift field. This might be explained by a build-up of electronegative impurities at the surface, which would have a lower equilibrium concentration if they capture electrons at a lower rate due to the increased drift field.

In order to increase the fields, I increased the bias voltages on the stainless steel electrodes. However, due to no "hot spots" in the full (x, y)-distribution of S2s, it is unlikely that there was a significant emission of electrons from metal surfaces. Metal surfaces, as conductors, readily emit electrons, particularly via photoionization [57] and could be likely material origins of electrons, particularly around surface imperfections. Ultimately, electron emission from metals is unlikely to be the leading contribution, as it is unclear why emission processes from metals should be position-correlated with the primary interaction to such long times. Emission from the metal electrodes might still be reasonable for the position uncorrelated signals.

I was not able to model this theory, so the ripple hypothesis and electronegative impurity build-up at the surface remains speculation in my paper. There could also be multiple compounding processes. My findings disagree with theories that these electron trains are from electrons caught and released by electronegative impurities in the liquid bulk, or are from metal surfaces. They rather indicate that the electron trains are an effect at the liquid-gas interface.

By identifying this background, I allow liquid xenon dark matter experiments to more effectively remove these backgrounds via positional and temporal cuts, based on the manifestation of the power law and position-correlation findings in a given detector. These tools also enable researchers to more carefully model these background contributions. Such a study is imperative to the success of the LBECA experiment, which aims to use a liquid xenon TPC to study low-energy interactions through few-electron ionization signals. This characterization offers a method to improve a detector's sensitivity to such interactions, particularly from solar neutrinos and light dark matter candidates. Continuing my focus on low-energy interactions, I also looked into lowering the S1 detection threshold, as outlined in the next Chapter.

5. A SINGLE-PHOTON S1 THRESHOLD TOWARD BORON-8 SOLAR NEUTRINO DETECTION

Sun's Neutrinos - A Poem

Sunshine streaming,
solar surface
seething, seeming
without solace.

Underneath its
undulations
cosmic units'
unifications.

Nuclei, new,
neutrinos send,
notated nu,
never they end.

From the left panel of Figure 1.9 on Page 40 in the Introductory Chapter 1, the S1 signal becomes undetectable first, meaning that lower-energy interactions are characterized by a lone S2. The lowest energy interactions detectable in a dual-phase liquid xenon TPC create a single-electron S2 [51]–[53]. As shown in Chapter 4, there is a large detector background to the smallest S2 signals. Under the detector background, the particle physics process with the highest rate at this energy is expected to be Boron-8 solar neutrinos undergoing Coherent Elastic Neutrino-Nucleus Scattering (CEvNS) [64], [99]. However, as of writing, CEvNS of non-reactor neutrinos has never been directly measured, and even with nuclear reactor neutrinos, it has not been measured in xenon [9], [100]–[102].

As a large 131 GeV/c^2 atom, xenon's energy threshold is higher than targets used by the COHERENT Collaboration, which has made the best measurements of CEvNS to date [100]. However, the CEvNS cross-section σ varies directly with the nucleus' neutron number squared, N^2, which is higher for a larger nucleus. The differential cross-section for the CEvNS process per nuclear recoil energy $\frac{d\sigma}{dE_{NR}}$ is generally given in the following equations. It depends on the Fermi Constant G_F, the mass of the target (in this case xenon) M,

the neutrino energy E_ν, the vector standard model coupling constants for protons g_V^p and neutrons g_V^n and its nuclear form factor $F^V(Q^2)$ dependent on momentum transfer Q, the same variables for the standard model axial-vector coupling g_A^p, g_A^n and $F^A(Q^2)$, the number of protons Z and neutrons N, and those nucleons' spin quantum states $Z_{\uparrow,\downarrow}$ and $N_{\uparrow,\downarrow}$ [103].

$$\frac{d\sigma}{dE_{NR}} = \frac{G_F^2 M}{2\pi}\left[(G_V+G_A)^2 + (G_V-G_A)^2\left(1-\frac{E_{NR}}{E_\nu}\right)^2 - (G_V^2-G_A^2)\frac{ME_{NR}}{E_\nu^2}\right] \tag{5.1}$$

$$G_V = (g_V^p Z + g_V^n N)F^V(Q^2) \tag{5.2}$$

$$G_A = (g_A^p(Z_\uparrow - Z_\downarrow) + g_A^n(N_\uparrow - N_\downarrow))F^A(Q^2) \tag{5.3}$$

The recoil energy is much smaller than the neutrino energy, $E_{NR}/E_\nu \ll 1$, so the nuclear form factors are approximately unity, $F^V(Q^2) \sim 1$, $F^A(Q^2) \sim 1$. The vector couplings are $g_V^n = 1/2$ and $g_V^p = 1 - 4\sin^2(\theta_W)$, but $\sin^2(\theta_W) = 0.231$ is close enough to $1/4$ that $g_V^p Z \ll g_V^n N$ and $G_V \sim N/2$. Xenon has an even number of protons (54) and its most abundant isotopes are stable, so $G_A \sim g_A^n$ and $G_A^2 \ll G_V^2$. These simplifications mean that Equation 5.1 can be approximated by Equation 5.4 and the cross-section is enhanced by the neutron number squared $\frac{d\sigma}{dE_{NR}} \propto N^2$ [101].

$$\frac{d\sigma}{dE_{NR}} \sim \frac{G_F^2 M}{2\pi}\left[2 - \frac{ME_{NR}}{E_\nu^2}\right]\frac{N^2}{4} \tag{5.4}$$

Although a neutrino's most likely interaction with xenon becomes this CEvNS process, which is independent of neutrino flavor, the deposited energy, E_{NR} is typically very small and at the edge of detection [104]. An S1 quickly becomes undetectable because the PMTs themselves have a typical quantum efficiency of 30% [105]. The total light collection efficiency after geometric considerations is usually less than 20%. Another limitation is the $\mathcal{O}(10)$ Hz PMT dark count rates, which are false photon signals dominated by thermionic emission of electrons from the photocathode. XENON1T required three PMTs detecting coincident light signals to constitute an S1, which we reduced to two PMTs in our ultimately unsuccessful search for Boron-8 solar neutrino CEvNS [62].

Analyses searching for Boron-8 CEvNS so far have benefited most from requiring an S1. S2-only analyses have had a greater uncertainty in the backgrounds and high background rates that outweigh the increased expected CEvNS rates [64]. Poisson process background rates are strongly suppressed by requiring a coincident S1. The rate of accidental coincidences is the product of the lone S1 and S2 rates suppressed by the less than 1 ms coincidence window. With an S1, nuclear recoils can be selected and electronic recoils rejected. An S1 is also very useful for avoiding backgrounds at the Cathode and above the Gate by enabling clear depth perception. While XENON1T required three coincident PMTs to constitute an S1, I wanted to see if this could be reduced to a single photon in one PMT.

Because dark counts are dominated by thermionic electron emission, they are expected to follow the single-photon response spectrum of a PMT. Highly energetic 178 nm xenon scintillation photons can actually trigger two simultaneous photoelectrons from the photocathode roughly 20% of the time. The relative fraction of double photoelectron (DPE) pulses for measured photons depends on the wavelength as in Figure 5.1 [106].

This means that lone PMT hits that are the size of DPE are much more likely to be actual scintillation photons than dark counts. LUX first explored an S1 threshold of single-photons with DPE signals [107], and I started doing the same in XENON1T data, with the particular goal of detecting Boron-8 solar neutrino CEvNS. For CEvNS, I identified four channels at the lowest detection threshold limits.

One channel for CEvNS mentioned is an S2-only search, since the CEvNS signal from Boron-8 solar neutrinos is expected to be the dominant particle interaction process. From a simulation of Boron-8 CEvNS events in XENON1T, using the Noble Element simulation Tecnique (NEST) software package [108], I expect about 100 events/(ton·year). Since the best XENON1T S2 background rate (including some cuts based on Chapter 4) was $\sim$0.7mHz [62], which would be over ten thousand background events/(ton·year), and not a worthwhile detection avenue.

Having an S2 matched to an S1 seen by two PMTs, which we ultimately achieved in [62], is another channel. I would expect from the simulation less than 10 events/(ton·year). The largest background would be accidental coincidences of the background S2 rate and the rate of dark-count pile-up S1s. For 248 PMTs, a total dark count rate of 10 kHz was

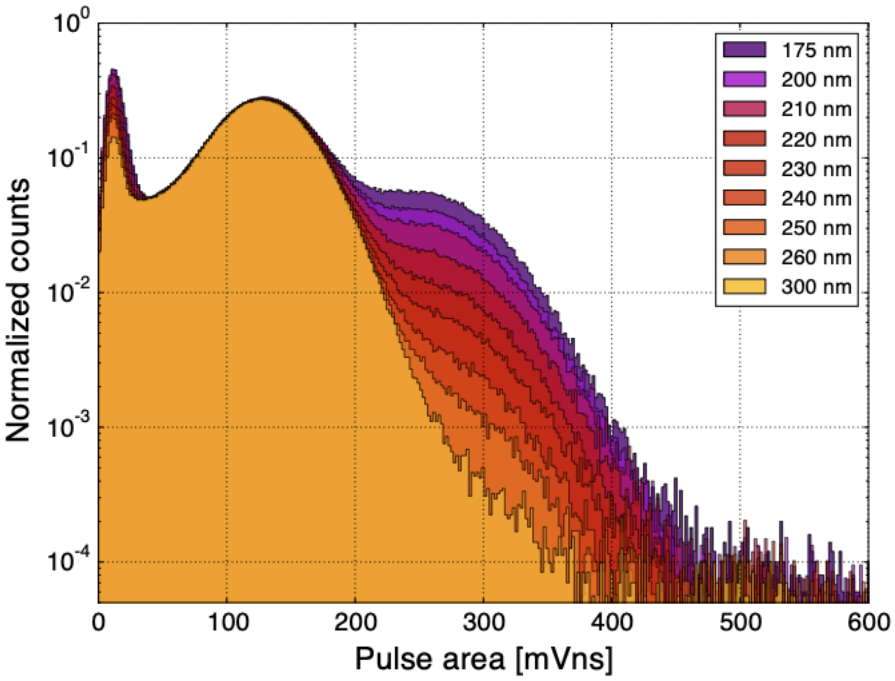

Figure 5.1. Increased probability of double photoelectron (DPE) signal for a single incident photon for increasing photon energy (decreased wavelength). From Reference [106].

over-estimated to be conservative. With only 2 ms event windows to analyze, the quieter times between events likely has a lower rate. With the two PMTs' S1 restricted to a 50 ns coincidence window, the final accidental coincidence background rate of random S2s and false S1s is around 10^{-6} Hz, which is roughly 50 events/(ton·year).

In the main analysis channel with three coincident PMTs for an S1, the simulation predicted less than 5 events/(ton·year). Pile-up false S1s are even more unlikely, so the S1-S2 accidental coincidence rate is close to 10^{-7} Hz, giving 6 events/(ton·year). Detection was not possible in XENON1T, but will be possible in XENONnT, which is expected to accumulate 20 ton·years of exposure.

The last detection channel, which I pursued is a DPE S1 in 1 PMT matched to an S2. The simulation predicted around 50 events/(ton·year) for a single-photon detectable S1, so requiring the photon to have caused a DPE S1 would cut the expected signal events to about 10 events/(ton·year). However, since dark counts are not expected to create DPE signals, the background S1 rate and therefore the accidental coincidence S1-S2 rate are suppressed by at least 3 orders of magnitude for the nominal 80% decrease in signal. I therefore also expected the background to be about 10 events/(ton·year).

For this analysis, I wanted a clear understanding of the PMTs, in case some should be excluded for higher dark count rates or lower DPE xenon scintillation fractions. I started with XENON1T to characterize the DPE fraction per PMT, but I needed to find times where I knew the PMTs were seeing true single xenon scintillation photons. In XENON1T with 248 PMTs, a single-electron signal was only 28 PE, so most contributing PMTs would only detect a single photon, and the < 1 μs duration means that dark counts during the electron signal are unlikely. Unfortunately, PAX only calculated the area per PMT and hits per PMT, without giving the exact area per photon hit. For the upgrade to XENONnT, we were transitioning to a triggerless DAQ to have no dead time and complete sensitivity to every dark count. To deal with this data, we developed the Streaming Analysis for Xenon (STRAX) processing framework. With STRAX, I could recover the single xenon scintillation photon spectrum for each PMT, and some XENON1T data was converted to a STRAX format for testing.

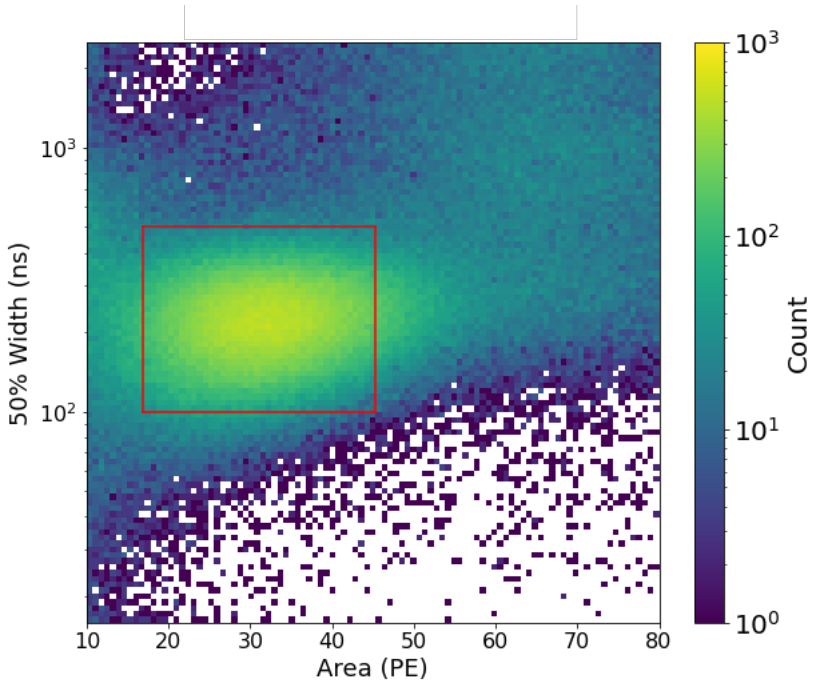

Figure 5.2. A rough selection of the single electron population in XENON1T.

I first identified XENON1T's single-electron S2s in STRAX, which are most apparent in an width and size parameter space as shown in Figure 5.2. I then selected a majority of them to deconstruct into their photon signals. I recorded the global start and end time of the S2 waveform and worked some STRAX magic.

With STRAX, it is easy to reprocess raw data, and I made the impossible requirement that neither an S1 nor an S2 could be found without 999 PMTs contributing. This forced all photon signals to be considered independently as lone hits of light in a PMT, so I could analyze photon pulses' individual areas and know in which PMT they occurred. I gathered all the information for the photons that occurred during the single-electron S2s and acquired the per-PMT xenon scintillation spectrum. I still ultimately required the pulses to be isolated by 100ns to avoid incomplete integration between multiple pulses in a PMT. The final spectra are shown in Figure 5.3. Even with the isolation requirement, the top array PMTs detect more photons, as expected. The more central PMTs also see more light than the PMTs around the edges.

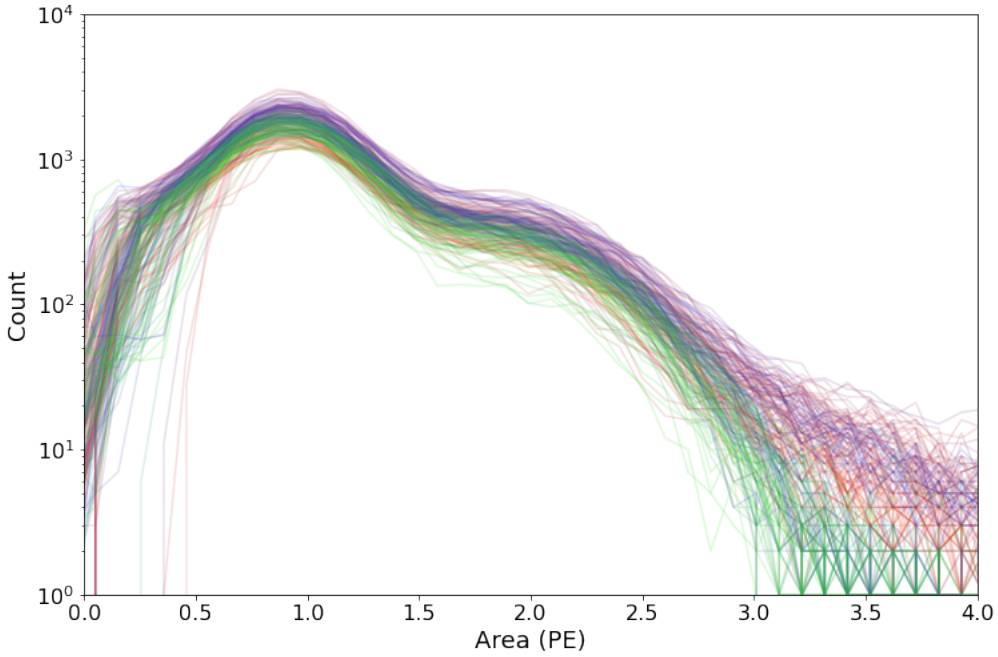

Figure 5.3. The XENON1T PMTs' xenon scintillation photon spectra. The PMTs on the top PMT array are colored purple to red with expanding radius from the detector center, and the PMTs of the bottom array are colored blue to green with expanding radius.

With these single xenon scintillation photon spectra, I needed to determine how they compared to the expected background from dark counts. Then I could choose the PE ranges for each PMT where I would be more certain that a hit was a photon and not a dark count. For XENON1T, I could never be sure that the lone hits were truly dark counts without significant xenon scintillation contamination.

XENONnT provided an excellent dark count opportunity. I requested a day of dark count data from the PMTs in vacuum. The PMT gains were not yet set to the science data, the Cherenkov muon veto water tank had not been filled with water, and the temperatures were far above liquid xenon temperatures. Without the water in the tank, a higher external gamma radiation background was expected. With lower temperatures, the dark count rates decrease, but I was not sure if the full dark count spectrum, including any contribution at higher PE, would scale uniformly. I became worried because there seemed to be a non-negligible dark count rate for dark counts above the single photon 1 PE expected peak, measuring in size up to nearly 15 PE.

When XENONnT was filled with xenon and the electrodes and PMTs had achieved science run conditions, I checked the PMT's dark count spectra from this data with the vacuum dark count data spectra. I required that a dark count must be the only signal that a PMT had seen for over 10 μs to avoid including afterpulses. Noting that LUX had identified photon trains in addition to electron trains [90], I required the dark count to be at least 10 ms after any peak larger than 200 PE, a size where most of XENONnT's 494 PMTs still would not have seen any light. The spectra matched, and the non-negligible tail of large-PE dark counts was confirmed.

To visualize what to expect from the PMTs per ton·year exposure of XENONnT, the CEvNS single-photon S1 expectation rate was divided among the 494 PMTs, with the top array seeing 1/3 of the light and the bottom array seeing 2/3 of the light to account for the S1 photons being emitted in the liquid and having a high likelihood of total internal reflection at the liquid xenon surface. The measured "area_fraction_top" of S1s is roughly 30%. The bottom array PMTs, submerged in liquid xenon, typically have a higher dark count rate than the top array PMTs in gas. The PMTs' single xenon scintillation photon response spectrum was then normalized to their expected measured CEvNS S1 signal for

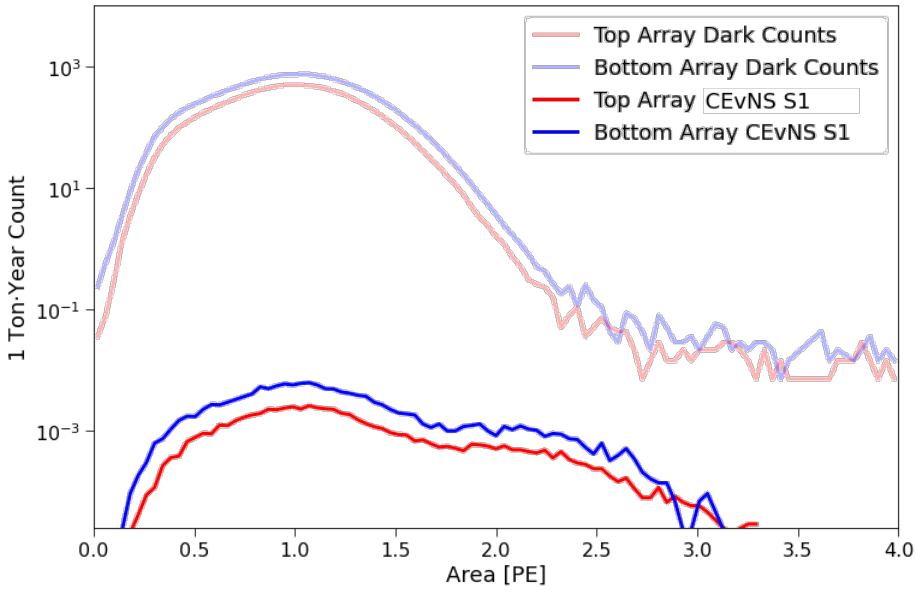

Figure 5.4. Two example XENONnT PMTs' expected spectra for Boron-8 CEvNS xenon scintillation light S1s and dark counts accidentally coincident with a background S2 for a ton·year exposure of XENONnT with a 4-ton fiducial volume and 3-month livetime.

1 ton·year exposure. With rough cuts based on Chapter 4, the lone S2 rate was estimated to be 50 mHz. The drift time of XENONnT is a little over 2 ms in its current configuration and it is expected to have a 4 ton fiducial volume, so over the course of a quarter of a year for the 1 ton·year exposure, there will be a little over 1,000 s of time before S2s where a dark count can be accidentally coincident. Based on that livetime, the dark count spectrum can also be calculated. As can be seen in Figure 5.4, the accidental coincidence background is much too high to expect to see CEvNS in this channel.

Before I had confirmed that this method would not find solar Boron-8 neutrinos, I had proposed working on it with the Purdue Data Mine undergraduate researchers and earned a Graduate Fellowship from the Indiana Space Grant Consortium. I asked the undergraduates to try the analysis through brute force with XENON1T, matching appropriately sized S2s (150-300 PE) with larger (2-3 PE) lone hits and trying to weed out physically impossible matches based on other parameters. In less than a week of data where we expected no CEvNS events, they found hundreds of the accidental coincident S1-S2 events. They did good work, and one group's poster presentation placed second at the Purdue Spring Research Conference.

Even if we had been able to optimize the cuts and perform more sophisticated cuts based on the phenomenology of the electron trains, it is clear that the accidental coincidence background was too high in XENON1T.

5.1 Conclusion to Single-Photon S1s toward Boron-8 Solar Neutrino Detection

Over a longer time, a DPE S1 could be a viable channel, but requiring two or three coincident PMTs in an S1 will be more sensitive at that point. If the PMT dark count spectrum ended at the 1 PE Gaussian and did not have a non-negligible spectrum extending to higher hit areas, then there would have been a PE range per PMT where this analysis could have succeeded. The upgrade to LUX, LUX-ZEPLIN, which uses the same PMTs as XENON1T and XENONnT, appeared unaware of this contribution in their low-mass dark matter projections paper [109].

It is unclear what these large dark counts are. Thermionic emission from the photocathode does dominate but can only create one photoelectron. There may be ambient radioactivity, so the dark count spectra should be compared for a set of PMTs above ground with higher cosmic radiation and then deep underground and well-shielded from radiation.

Another interesting theory is that these are ghost afterpulses. The mechanism of afterpulsing is typically expected to be that a photoelectron from the photocathode ionizes residual gas in the PMT on its way to the first dynode. The gas ion accelerates to the photocathode and causes one or more electrons to be emitted and they are amplified down the dynodes like photoelectrons. The delay time from the gas atom ionizing to it reaching the photocathode and creating the afterpulse is characteristic of the gas species. Helium, argon and xenon with increasing mass have increased delay times to their afterpulses. Afterpulses can be upwards of 10 PE, with helium afterpulses attaining more than 30 PE occasionally [82].

For a ghost afterpulse, no measured initial photoelectron causes a gas atom to ionize and collide with the photocathode. Perhaps there are alpha decays of intrinsic Radon-222 in the PMTs. The alpha particle, essentially a doubly-ionized helium atom will create a large signal when impacting the photocathode. For residual gas somehow ionizing and causing

these ghost afterpulses after no initial signal, we can compare the spectra of PMTs with different levels of residual gas, and expect the leakier PMTs to have a higher rate of these large dark counts. The individual PMTs' radon contamination is unknowable while the detector is closed, so if these large dark counts were dominated by alpha particles, it would be difficult to determine. Previous efforts have lowered the intrinsic radioactivity of the XENONnT PMTs to where they are now [110].

With the triggerless DAQ of XENONnT and using STRAX, we can have a much better understanding of the PMTs and their dark counts. We will also have excellent statistics to explore the electron trains and optimize stringent cuts to reduce the lone S2 rates. A much lower S2 rate is essential for fewer accidental coincidence backgrounds, because the overall $\sim$10 Hz dark count rate per PMT and non-negligible large dark counts appear to be systematic limitations. Ultimately, a single-photon DPE S1 is an interesting exercise for searching for dark matter, but is not the best analysis channel for discovering Boron-8 solar neutrinos.

6. SUMMARY POEM

Pausing to Reflect before a New Beginning - A Freeform Poem

The Work presented in this Thesis
I performed over four years
(part of my five years)
in the Purdue Physics and Astronomy doctorate program.
The plethora of projects
are tied to the theme
of rare particle interactions
in liquid xenon time projection chambers.
I performed several investigations
in XENON1T data, starting
with the Big Sphere radon veto.
I guided undergraduates through analyses
to look for multiply-interacting massive particles,
investigate muon events,
and try to detect Boron-8 solar neutrinos.
Co-requisite to Boron-8 solar neutrinos,
(with S1s down to a single photon)
was to suppress the rates of small S2s.
I built the ASTERiX detector
to characterize the background S2s
correlated with location and time
to energetic primary interaction events.
Despite my attempts with infrared light,
the stubborn background remained.
I failed
to get rid of the overwhelming signals.
I succeeded
in providing an analysis framework
to work around the backgrounds.
Even then, these backgrounds
and the dark counts of the PMTs
and the scarcity of neutrino interactions
and the paucity of energy in the interactions
and the only 20% DPE signal single photon fraction
meant I could not
detect Boron-8 solar neutrinos.

Now as I pause
...
Previous work now to summarize

before starting the next steps
anew.
I have been awarded a
three-year Mathematical and Physical Sciences
Ascending Postdoctoral Research Fellowship
from the National Science Foundation
to go to
the University of California at San Diego
and continue my work, searching for Boron-8 solar neutrinos
and light dark matter candidates interacting
with the XENONnT dark matter detector.
A condition of the fellowship:
to continue to encourage and mentor
and foster and guide and teach
a new generation of physics researchers, particularly
underrepresented minorities (URM).
As a woman, though not a usual minority,
I know the strenuous struggle to feel
like I belong.
I endeavor to encourage everyone
especially URM
to enter, integrate, and embrace physics.
As I have found,
XENON detector data is an excellent introduction
to research and big data and physics.
I spent one month in December 2019
constructing the XENONnT TPC.
I spent three months January through March 2021
babysitting and debugging all XENONnT.
With such an investment,
and excitement for what we could find,
I am thrilled to stay on this path with XENONnT,
confirmed to continue
for the next five or so years.
After that, there is DARWIN, too!

Toward the detection of low-energy interactions
from Boron-8 solar neutrinos via
coherent elastic neutrino-nucleus scattering
or light dark matter candidates,
there is work to adapt the electron train analysis to XENONnT.
There is work to cut these backgrounds
and have enough detector livetime
(and maybe events?)
to make a good analysis or neutrino measurement.

Maybe we can be the first to detect this
coherent elastic neutrino-nucleus scattering
with xenon nuclei in XENONnT.
Tangential open questions remain:
What can be improved in ASTERiX?
What causes electron train backgrounds?
What are the high energy dark counts?
If the trains are really at the liquid-gas
interface,
can we make a better detector
with only liquid xenon?
But the prospect of perfect ionization charge signal detection
is so far constrained to dual-phase detectors:
Practically infinite electron lifetime
(Check, achieved in XENONnT),
practically 100% extraction efficiency
(Check, for liquid electric fields over 10 kV/cm[60]),
practically 100% peak finding efficiency
(Check, for single-electron signals over 10 PE).
In a single-phase liquid xenon detector
some S2s are seen, as such,
but
Single-electron signals have not been detected
yet.
It is one of my goals at
the University of California at San Diego
to help construct such a single-phase TPC,
which may not have the electron trains
and could easily detect neutrinos via
coherent elastic neutrino-nucleus scattering.
I have assessed my past
secured my future
and seek now to graduate with my PhD.
I will continue to search for
what the Universe is made of
after this stopping point.

REFERENCES

[1] N. Aghanim *et al.*, "Planck 2018 results. VI. Cosmological parameters," *Astron. Astrophys.*, vol. 641, A6, 2020. DOI: 10.1051/0004-6361/201833910. arXiv: 1807.06209 [astro-ph.CO].

[2] E. Aprile *et al.*, "Dark Matter Search Results from a One Tonne-Year Exposure of XENON1T," *Phys. Rev. Lett.*, vol. 121, no. 11, p. 111 302, 2018. DOI: 10.1103/PhysRevLett.121.111302. arXiv: 1805.12562 [astro-ph.CO].

[3] J. Aalbers *et al.*, "DARWIN: towards the ultimate dark matter detector," *JCAP*, vol. 11, p. 017, 2016. DOI: 10.1088/1475-7516/2016/11/017. arXiv: 1606.07001 [astro-ph.IM].

[4] B. J. Mount *et al.*, "LUX-ZEPLIN (LZ) Technical Design Report," 2017. arXiv: 1703.09144 [physics.ins-det].

[5] H. Zhang *et al.*, "Dark matter direct search sensitivity of the PandaX-4T experiment," *Sci. China Phys. Mech. Astron.*, vol. 62, no. 3, p. 31 011, 2019. DOI: 10.1007/s11433-018-9259-0. arXiv: 1806.02229 [physics.ins-det].

[6] P. Zyla *et al.*, "Review of Particle Physics," *PTEP*, vol. 2020, no. 8, p. 083C01, 2020. DOI: 10.1093/ptep/ptaa104.

[7] W. Röntgen, *On a New Kind of Rays*. Dec. 1895, ISBN: 9780199554652. DOI: 10.1093/owc/9780199554652.003.0032.

[8] P. A. Cherenkov, "Visible radiation produced by electrons moving in a medium with velocities exceeding that of light," *Phys. Rev.*, vol. 52, pp. 378–379, 1937. DOI: 10.1103/PhysRev.52.378.

[9] D. Akimov *et al.*, "Observation of Coherent Elastic Neutrino-Nucleus Scattering," *Science*, vol. 357, no. 6356, pp. 1123–1126, 2017. DOI: 10.1126/science.aao0990. arXiv: 1708.01294 [nucl-ex].

[10] S. Chatrchyan *et al.*, "Observation of a New Boson at a Mass of 125 GeV with the CMS Experiment at the LHC," *Phys. Lett. B*, vol. 716, pp. 30–61, 2012. DOI: 10.1016/j.physletb.2012.08.021. arXiv: 1207.7235 [hep-ex].

[11] G. Aad *et al.*, "Observation of a new particle in the search for the Standard Model Higgs boson with the ATLAS detector at the LHC," *Phys. Lett. B*, vol. 716, pp. 1–29, 2012. DOI: 10.1016/j.physletb.2012.08.020. arXiv: 1207.7214 [hep-ex].

[12] P. W. Higgs, "Broken symmetries, massless particles and gauge fields," *Phys. Lett.*, vol. 12, pp. 132–133, 1964. DOI: 10.1016/0031-9163(64)91136-9.

[13] B. T. Cleveland, T. Daily, R. Davis Jr., J. R. Distel, K. Lande, C. K. Lee, P. S. Wildenhain, and J. Ullman, "Measurement of the solar electron neutrino flux with the Homestake chlorine detector," *Astrophys. J.*, vol. 496, pp. 505–526, 1998. DOI: 10.1086/305343.

[14] J. N. Bahcall, A. M. Serenelli, and S. Basu, "New solar opacities, abundances, helioseismology, and neutrino fluxes," *Astrophys. J. Lett.*, vol. 621, pp. L85–L88, 2005. DOI: 10.1086/428929. arXiv: astro-ph/0412440.

[15] R. Davis Jr., D. S. Harmer, and K. C. Hoffman, "Search for neutrinos from the sun," *Phys. Rev. Lett.*, vol. 20, pp. 1205–1209, 1968. DOI: 10.1103/PhysRevLett.20.1205.

[16] K. S. Hirata *et al.*, "Observation of B-8 Solar Neutrinos in the Kamiokande-II Detector," *Phys. Rev. Lett.*, vol. 63, p. 16, 1989. DOI: 10.1103/PhysRevLett.63.16.

[17] A. W. P. Poon *et al.*, "Neutrino observations from the Sudbury Neutrino Observatory," *AIP Conf. Proc.*, vol. 610, no. 1, E. Norman, L. Schroeder, and G. Wozniak, Eds., pp. 218–230, 2002. DOI: 10.1063/1.1469931. arXiv: nucl-ex/0110005.

[18] C. Giganti, S. Lavignac, and M. Zito, "Neutrino oscillations: The rise of the PMNS paradigm," *Prog. Part. Nucl. Phys.*, vol. 98, pp. 1–54, 2018. DOI: 10.1016/j.ppnp.2017.10.001. arXiv: 1710.00715 [hep-ex].

[19] A. Melfo and G. Senjanovic, "Neutrino: chronicles of an aloof protagonist," Jun. 2021. arXiv: 2107.05472 [physics.hist-ph].

[20] I. Newton, *Philosophiæ Naturalis Principia Mathematica*. England, 1687.

[21] A. Einstein, "Zur Allgemeinen Relativitätstheorie," *Sitzungsber. Preuss. Akad. Wiss. Berlin (Math. Phys.)*, vol. 1915, pp. 778–786, 1915, [Addendum: Sitzungsber. Preuss. Akad. Wiss. Berlin (Math.Phys.) 1915, 799–801 (1915)].

[22] J. C. Kapteyn, "First Attempt at a Theory of the Arrangement and Motion of the Sidereal System," *Astrophys. J.*, vol. 55, pp. 302–328, 1922. DOI: 10.1086/142670.

[23] G. Bertone and D. Hooper, "History of dark matter," *Rev. Mod. Phys.*, vol. 90, no. 4, p. 045 002, 2018. DOI: 10.1103/RevModPhys.90.045002. arXiv: 1605.04909 [astro-ph.CO].

[24] M. S. Turner, "Cosmological parameters," *AIP Conf. Proc.*, vol. 478, no. 1, D. O. Caldwell, Ed., pp. 113–128, 1999. DOI: 10.1063/1.59381. arXiv: astro-ph/9904051.

[25] C. Grupen, *Astroparticle Physics*, 2nd ed. Springer, 2020, ISBN: 978-3-030-27339-2. DOI: 10.1007/978-3-030-27339-2.

[26] E. Gawiser and J. Silk, "The Cosmic microwave background radiation," *Phys. Rept.*, vol. 333, pp. 245–267, 2000. DOI: 10.1016/S0370-1573(00)00025-9. arXiv: astro-ph/0002044.

[27] A. Friedmann, "On the Possibility of a world with constant negative curvature of space," *Z. Phys.*, vol. 21, pp. 326–332, 1924. DOI: 10.1007/BF01328280.

[28] E. Hubble, "A relation between distance and radial velocity among extra-galactic nebulae," *Proc. Nat. Acad. Sci.*, vol. 15, pp. 168–173, 1929. DOI: 10.1073/pnas.15.3.168.

[29] J. Frieman, M. Turner, and D. Huterer, "Dark Energy and the Accelerating Universe," *Ann. Rev. Astron. Astrophys.*, vol. 46, pp. 385–432, 2008. DOI: 10.1146/annurev.astro.46.060407.145243. arXiv: 0803.0982 [astro-ph].

[30] P. A. R. Ade *et al.*, "Planck 2015 results. XIII. Cosmological parameters," *Astron. Astrophys.*, vol. 594, A13, 2016. DOI: 10.1051/0004-6361/201525830. arXiv: 1502.01589 [astro-ph.CO].

[31] D. J. Eisenstein *et al.*, "Detection of the Baryon Acoustic Peak in the Large-Scale Correlation Function of SDSS Luminous Red Galaxies," *Astrophys. J.*, vol. 633, pp. 560–574, 2005. DOI: 10.1086/466512. arXiv: astro-ph/0501171.

[32] V. C. Rubin and W. K. Ford Jr., "Rotation of the Andromeda Nebula from a Spectroscopic Survey of Emission Regions," *Astrophys. J.*, vol. 159, pp. 379–403, 1970. DOI: 10.1086/150317.

[33] E. F. Bell, C. M. Baugh, S. Cole, C. S. Frenk, and C. G. Lacey, "The Properties of spiral galaxies: Confronting hierarchical galaxy formation models with observations," *Mon. Not. Roy. Astron. Soc.*, vol. 343, p. 367, 2003. DOI: 10.1046/j.1365-8711.2003.06673.x. arXiv: astro-ph/0303531.

[34] K. Freese, M. Lisanti, and C. Savage, "Colloquium: Annual modulation of dark matter," *Rev. Mod. Phys.*, vol. 85, pp. 1561–1581, 2013. DOI: 10.1103/RevModPhys.85.1561. arXiv: 1209.3339 [astro-ph.CO].

[35] F. Zwicky, "Die Rotverschiebung von extragalaktischen Nebeln," *Helv. Phys. Acta*, vol. 6, pp. 110–127, 1933, [Gen. Rel. Grav.41,207(2009)]. DOI: 10.1007/s10714-008-0707-4.

[36] D. Clowe, M. Bradac, A. H. Gonzalez, M. Markevitch, S. W. Randall, C. Jones, and D. Zaritsky, "A direct empirical proof of the existence of dark matter," *Astrophys. J. Lett.*, vol. 648, pp. L109–L113, 2006. DOI: 10.1086/508162. arXiv: astro-ph/0608407.

[37] E. O. Nadler *et al.*, "Milky Way Satellite Census. III. Constraints on Dark Matter Properties from Observations of Milky Way Satellite Galaxies," *Phys. Rev. Lett.*, vol. 126, p. 091 101, 2021. DOI: 10.1103/PhysRevLett.126.091101. arXiv: 2008.00022 [astro-ph.CO].

[38] J. Yoo, J. Chaname, and A. Gould, "The end of the MACHO era: limits on halo dark matter from stellar halo wide binaries," *Astrophys. J.*, vol. 601, pp. 311–318, 2004. DOI: 10.1086/380562. arXiv: astro-ph/0307437.

[39] M. Lisanti, "Lectures on Dark Matter Physics," in *Theoretical Advanced Study Institute in Elementary Particle Physics: New Frontiers in Fields and Strings*, Mar. 2016. DOI: 10.1142/9789813149441_0007. arXiv: 1603.03797 [hep-ph].

[40] X. Calmet and F. Kuipers, "Theoretical bounds on dark matter masses," *Phys. Lett. B*, vol. 814, p. 136 068, 2021. DOI: 10.1016/j.physletb.2021.136068. arXiv: 2009.11575 [hep-ph].

[41] S. W. Hawking, "Particle Creation by Black Holes," *Commun. Math. Phys.*, vol. 43, G. W. Gibbons and S. W. Hawking, Eds., pp. 199–220, 1975, [Erratum: Commun. Math. Phys. 46, 206 (1976)]. DOI: 10.1007/BF02345020.

[42] C. Alcock *et al.*, "EROS and MACHO combined limits on planetary mass dark matter in the galactic halo," *Astrophys. J. Lett.*, vol. 499, p. L9, 1998. DOI: 10.1086/311355. arXiv: astro-ph/9803082.

[43] R. N. Rogalyov, "CP violation in K meson decays," in *24th International Workshop on Fundamental Problems of High Energy Physics and Field Theory*, 2001, pp. 17–43. arXiv: hep-ph/0204099.

[44] L. C. Hockley, "Direct CP Violation in B Meson Decays," Ph.D. dissertation, Adelaide U., 2020.

[45] R. D. Peccei and H. R. Quinn, "Cp conservation in the presence of pseudoparticles," *Phys. Rev. Lett.*, vol. 38, pp. 1440–1443, 25 May 1977. DOI: 10.1103/PhysRevLett.38.1440.

[46] S. Weinberg, "A New Light Boson?" *Phys. Rev. Lett.*, vol. 40, pp. 223–226, 1978. DOI: 10.1103/PhysRevLett.40.223.

[47] M. Dutra, "Origins for dark matter particles : from the "WIMP miracle" to the "FIMP wonder"," Ph.D. dissertation, Orsay, LPT, 2019.

[48] E. Aprile *et al.*, "Measurement of the Quantum Efficiency of Hamamatsu R8520 Photomultipliers at Liquid Xenon Temperature," *JINST*, vol. 7, P10005, 2012. DOI: 10.1088/1748-0221/7/10/P10005. arXiv: 1207.5432 [astro-ph.IM].

[49] D. S. Akerib *et al.*, "Liquid xenon scintillation measurements and pulse shape discrimination in the LUX dark matter detector," *Phys. Rev. D*, vol. 97, no. 11, p. 112 002, 2018. DOI: 10.1103/PhysRevD.97.112002. arXiv: 1802.06162 [physics.ins-det].

[50] E. Aprile *et al.*, "The XENON1T Dark Matter Experiment," *Eur. Phys. J. C*, vol. 77, no. 12, p. 881, 2017. DOI: 10.1140/epjc/s10052-017-5326-3. arXiv: 1708.07051 [astro-ph.IM].

[51] E. Boulton *et al.*, "Calibration of a two-phase xenon time projection chamber with a ^{37}Ar source," *JINST*, vol. 12, no. 08, P08004, 2017. DOI: 10.1088/1748-0221/12/08/P08004. arXiv: 1705.08958 [physics.ins-det].

[52] D. Akerib *et al.*, "Ultralow energy calibration of LUX detector using ^{127}Xe electron capture," *Phys. Rev. D*, vol. 96, no. 11, p. 112 011, 2017. DOI: 10.1103/PhysRevD.96.112011. arXiv: 1709.00800 [physics.ins-det].

[53] B. Lenardo *et al.*, "Low-Energy Physics Reach of Xenon Detectors for Nuclear-Recoil-Based Dark Matter and Neutrino Experiments," *Phys. Rev. Lett.*, vol. 123, no. 23, p. 231 106, 2019. DOI: 10.1103/PhysRevLett.123.231106.

[54] A. Burenkov, D. Akimov, Y. Grishkin, A. Kovalenko, V. Lebedenko, V. Solovov, V. Stekhanov, F. Neves, and T. Sumner, "Detection of a single electron in xenon-based electroluminescent detectors," *Phys. Atom. Nucl.*, vol. 72, pp. 653–661, 2009. DOI: 10.1134/S1063778809040103.

[55] E. Santos *et al.*, "Single electron emission in two-phase xenon with application to the detection of coherent neutrino-nucleus scattering," *JHEP*, vol. 12, p. 115, 2011. DOI: 10.1007/JHEP12(2011)115. arXiv: 1110.3056 [physics.ins-det].

[56] J. Angle *et al.*, "A search for light dark matter in XENON10 data," *Phys. Rev. Lett.*, vol. 107, p. 051 301, 2011, [Erratum: Phys.Rev.Lett. 110, 249901 (2013)]. DOI: 10.1103/PhysRevLett.107.051301. arXiv: 1104.3088 [astro-ph.CO].

[57] E. Aprile *et al.*, "Observation and applications of single-electron charge signals in the XENON100 experiment," *J. Phys. G*, vol. 41, p. 035 201, 2014. DOI: 10.1088/0954-3899/41/3/035201. arXiv: 1311.1088 [physics.ins-det].

[58] D. Akerib *et al.*, "Calibration, event reconstruction, data analysis, and limit calculation for the LUX dark matter experiment," *Phys. Rev. D*, vol. 97, no. 10, p. 102 008, 2018. DOI: 10.1103/PhysRevD.97.102008. arXiv: 1712.05696 [physics.ins-det].

[59] B. Edwards *et al.*, "Extraction efficiency of drifting electrons in a two-phase xenon time projection chamber," *JINST*, vol. 13, no. 01, P01005, 2018. DOI: 10.1088/1748-0221/13/01/P01005. arXiv: 1710.11032 [physics.ins-det].

[60] J. Xu, S. Pereverzev, B. Lenardo, J. Kingston, D. Naim, A. Bernstein, K. Kazkaz, and M. Tripathi, "Electron extraction efficiency study for dual-phase xenon dark matter experiments," *Phys. Rev. D*, vol. 99, no. 10, p. 103 024, 2019. DOI: 10.1103/PhysRevD.99.103024. arXiv: 1904.02885 [physics.ins-det].

[61] E. Aprile *et al.*, "First Dark Matter Search Results from the XENON1T Experiment," *Phys. Rev. Lett.*, vol. 119, no. 18, p. 181 301, 2017. DOI: 10.1103/PhysRevLett.119.181301. arXiv: 1705.06655 [astro-ph.CO].

[62] E. Aprile *et al.*, "Search for Coherent Elastic Scattering of Solar ^{8}B Neutrinos in the XENON1T Dark Matter Experiment," *Phys. Rev. Lett.*, vol. 126, p. 091 301, 2021. DOI: 10.1103/PhysRevLett.126.091301. arXiv: 2012.02846 [hep-ex].

[63] E. Aprile *et al.*, "Observation of Excess Electronic Recoil Events in XENON1T," *Phys. Rev. D*, vol. 102, no. 7, p. 072 004, 2020. DOI: 10.1103/PhysRevD.102.072004. arXiv: 2006.09721 [hep-ex].

[64] E. Aprile *et al.*, "Light Dark Matter Search with Ionization Signals in XENON1T," *Phys. Rev. Lett.*, vol. 123, no. 25, p. 251 801, 2019. DOI: 10.1103/PhysRevLett.123.251801. arXiv: 1907.11485 [hep-ex].

[65] B. Lenardo *et al.*, "Measurement of the ionization yield from nuclear recoils in liquid xenon between 0.3 - 6 keV with single-ionization-electron sensitivity," 2019. arXiv: 1908.00518 [physics.ins-det].

[66] A. Kopec, A. L. Baxter, M. Clark, R. F. Lang, S. Li, J. Qin, and R. Singh, "Correlated single- and few-electron backgrounds milliseconds after interactions in dual-phase liquid xenon time projection chambers," *JINST*, vol. 16, no. 07, P07014, 2021. DOI: 10.1088/1748-0221/16/07/P07014. arXiv: 2103.05077 [physics.ins-det].

[67] Information Technology at Purdue, Rosen Center for Advanced Computing, *Data Depot*, https://www.rcac.purdue.edu/storage/depot, 2021.

[68] Project Jupyter, *Project Jupyter*, https://jupyter.org/index.html, 2021.

[69] Research Computing Center at UChicago, *Midway*, https://rcc.uchicago.edu/support-and-services/midway2, 2021.

[70] V. E. Guiseppe, S. R. Elliott, A. Hime, K. Rielage, and S. Westerdale, "A Radon Progeny Deposition Model," *AIP Conf. Proc.*, vol. 1338, R. Ford, Ed., pp. 95–100, 2011. DOI: 10.1063/1.3579565. arXiv: 1101.0126 [nucl-ex].

[71] E. Aprile *et al.*, "Results from a Calibration of XENON100 Using a Source of Dissolved Radon-220," *Phys. Rev. D*, vol. 95, no. 7, p. 072 008, 2017. DOI: 10.1103/PhysRevD.95.072008. arXiv: 1611.03585 [physics.ins-det].

[72] I. ANSYS, *ANSYS Fluent*, https://www.ansys.com/campaigns/ansys-fluids-computational-dynamics-simulation, 2021.

[73] J. Bramante, B. Broerman, R. F. Lang, and N. Raj, "Saturated Overburden Scattering and the Multiscatter Frontier: Discovering Dark Matter at the Planck Mass and Beyond," *Phys. Rev. D*, vol. 98, no. 8, p. 083 516, 2018. DOI: 10.1103/PhysRevD.98.083516. arXiv: 1803.08044 [hep-ph].

[74] XENON Collaboration, *PAX GitHub Repository*, https://github.com/XENON1T/pax, 2018.

[75] S. I. Alvis *et al.*, "First Limit on the Direct Detection of Lightly Ionizing Particles for Electric Charge as Low as e/1000 with the Majorana Demonstrator," *Phys. Rev. Lett.*, vol. 120, no. 21, p. 211 804, 2018. DOI: 10.1103/PhysRevLett.120.211804. arXiv: 1801.10145 [hep-ex].

[76] M. Clark, A. Depoian, B. Elshimy, A. Kopec, R. F. Lang, and J. Qin, "Direct Detection Limits on Heavy Dark Matter," *Phys. Rev. D*, vol. 102, no. 12, p. 123 026, 2020. DOI: 10.1103/PhysRevD.102.123026. arXiv: 2009.07909 [hep-ph].

[77] S. S. Ghosh, "Highlights from the Compact Muon Solenoid (CMS) Experiment," *Universe*, vol. 5, no. 1, p. 28, 2019. DOI: 10.3390/universe5010028. arXiv: 1901.05340 [hep-ex].

[78] M. Agostini *et al.*, "Flux Modulations seen by the Muon Veto of the GERDA Experiment," *Astropart. Phys.*, vol. 84, pp. 29–35, 2016. DOI: 10.1016/j.astropartphys.2016.08.002. arXiv: 1601.06007 [physics.ins-det].

[79] R. Goscinny and A. Uderzo, *Asterix - the official website*, https://www.asterix.com/en/, 2021.

[80] N. I. Corp., *What is LabView?* https://www.ni.com/en-us/shop/labview.html, 2021.

[81] D. W. Knight, *Gas Discharge Tubes - Introduction*, https://g3ynh.info/disch_tube/intro.html, 2021.

[82] V. C. Antochi *et al.*, "Improved quality tests of R11410-21 photomultiplier tubes for the XENONnT experiment," *JINST*, vol. 16, no. 08, P08033, 2021. DOI: 10.1088/1748-0221/16/08/P08033. arXiv: 2104.15051 [physics.ins-det].

[83] D. Masson and A. Kopec, *Obelix GitHub Repository*, https://github.com/purdue-darkmatters/obelix, 2018.

[84] P. Sorensen, "Electron train backgrounds in liquid xenon dark matter search detectors are indeed due to thermalization and trapping," 2017, arxiv:1702.04805. arXiv: 1702.04805 [physics.ins-det].

[85] J. Schiedt and R. Weinkauf, "Spin-orbit coupling in the O_2^- anion," *Z. Naturforsch*, vol. 50a, pp. 1041–1044, 1995. DOI: 10.1515/zna-1995-1110.

[86] P. Agnes *et al.*, "Low-Mass Dark Matter Search with the DarkSide-50 Experiment," *Phys. Rev. Lett.*, vol. 121, no. 8, p. 081 307, 2018. DOI: 10.1103/PhysRevLett.121.081307. arXiv: 1802.06994 [astro-ph.HE].

[87] D. Akimov *et al.*, "Measurement of single-electron noise in a liquid-xenon emission detector," *Prib. Tekh. Eksp.*, vol. 2012, no. 4, pp. 6–13, 2012. DOI: 10.1134/S002044121204001X.

[88] D. Akimov *et al.*, "Measurement of Single-Electron Noise in a Liquid Xenon Emission Detector," *JINST*, vol. 11, no. 03, p. C03007, 2016. DOI: 10.1088/1748-0221/11/03/C03007.

[89] E. Bodnia *et al.*, "The Electric Field Dependence of Single Electron Emission in the PIXeY Two-Phase Xenon Detector," 2021, arxiv:2101.03686. arXiv: 2101.03686 [physics.ins-det].

[90] D. Akerib *et al.*, "Investigation of background electron emission in the LUX detector," *Phys. Rev. D*, vol. 102, no. 9, p. 092 004, 2020. DOI: 10.1103/PhysRevD.102.092004. arXiv: 2004.07791 [physics.ins-det].

[91] G. Bakale, U. Sowanda, and W. F. Schmidt, "Effect of an Electric Field on Electron Attachment to SF_6, N_2O, and O_2 in Liquid Argon and Xenon," *J. Phys. Chem.*, vol. 80, 23, pp. 2556–2559, 1976. DOI: 10.1021/j100564a006.

[92] M. L. Goldstein, S. A. Morris, and G. G. Yen, "Problems with fitting to the power-law distribution," *The European Physical Journal B*, vol. 41, no. 2, pp. 255–258, 2004, ISSN: 1434-6036. DOI: 10.1140/epjb/e2004-00316-5. [Online]. Available: http://dx.doi.org/10.1140/epjb/e2004-00316-5.

[93] P. Sorensen and K. Kamdin, "Two distinct components of the delayed single electron noise in liquid xenon emission detectors," *JINST*, vol. 13, no. 02, P02032, 2018. DOI: 10.1088/1748-0221/13/02/P02032. arXiv: 1711.07025 [physics.ins-det].

[94] K. Yoshino, U. Sowada, and W. Schmidt, "Effect of molecular solutes on the electron drift velocity in liquid Ar, Kr, and Xe," *Phys. Rev. A*, vol. 14, pp. 438–444, 1976. DOI: 10.1103/PhysRevA.14.438.

[95] Y. Wei, J. Long, F. Lombardi, Z. Jiang, J. Ye, and K. Ni, "Development of a Sealed Liquid Xenon Time Projection Chamber with a Graphene-Coated Electrode," *JINST*, vol. 16, no. 01, P01018, 2020. DOI: 10.1088/1748-0221/16/01/P01018. arXiv: 2007.16194 [physics.ins-det].

[96] D. S. Burch, S. J. Smith, and L. M. Branscomb, "Photodetachment of O_2^-," *Phys. Rev.*, vol. 112, pp. 171–175, 1 1958. DOI: 10.1103/PhysRev.112.171. [Online]. Available: https://link.aps.org/doi/10.1103/PhysRev.112.171.

[97] W. F. Schmidt, O. Hilt, E. Illenberger, and A. G. Khrapak, "the mobility of positive and negative ions in liquid xenon," *Radiation Physics and Chemistry*, vol. 74, pp. 152–159, 2005. DOI: 10.1016/j.radphyschem.2005.04.008.

[98] D. J. Huntley, "An explantation of the power-law decay of luminescence," *J. Phys.: Condens. Matter*, vol. 18, pp. 1359–1365, 2006.

[99] L. Baudis, A. Ferella, A. Kish, A. Manalaysay, T. Marrodan Undagoitia, and M. Schumann, "Neutrino physics with multi-ton scale liquid xenon detectors," *JCAP*, vol. 01, p. 044, 2014. DOI: 10.1088/1475-7516/2014/01/044. arXiv: 1309.7024 [physics.ins-det].

[100] D. Akimov *et al.*, "First Measurement of Coherent Elastic Neutrino-Nucleus Scattering on Argon," *Phys. Rev. Lett.*, vol. 126, no. 1, p. 012 002, 2021. DOI: 10.1103/PhysRevLett.126.012002. arXiv: 2003.10630 [nucl-ex].

[101] K. Scholberg, "Observation of Coherent Elastic Neutrino-Nucleus Scattering by COHERENT," *PoS*, vol. NuFact2017, p. 020, 2018. DOI: 10.22323/1.295.0020. arXiv: 1801.05546 [hep-ex].

[102] D. Y. Akimov *et al.*, "First ground-level laboratory test of the two-phase xenon emission detector RED-100," *JINST*, vol. 15, no. 02, P02020, 2020. DOI: 10.1088/1748-0221/15/02/P02020. arXiv: 1910.06190 [physics.ins-det].

[103] J. Barranco, O. G. Miranda, and T. I. Rashba, "Probing new physics with coherent neutrino scattering off nuclei," *JHEP*, vol. 12, p. 021, 2005. DOI: 10.1088/1126-6708/2005/12/021. arXiv: hep-ph/0508299.

[104] K. Ni, J. Qi, E. Shockley, and Y. Wei, "Sensitivity of a Liquid Xenon Detector to Neutrino–Nucleus Coherent Scattering and Neutrino Magnetic Moment from Reactor Neutrinos," *Universe*, vol. 7, no. 3, p. 54, 2021. DOI: 10.3390/universe7030054.

[105] A. Lyashenko, T. Nguyen, A. Snyder, H. Wang, and K. Arisaka, "Measurement of the absolute Quantum Efficiency of Hamamatsu model R11410-10 photomultiplier tubes at low temperatures down to liquid xenon boiling point," *JINST*, vol. 9, no. 11, P11021, 2014. DOI: 10.1088/1748-0221/9/11/P11021. arXiv: 1410.3890 [astro-ph.IM].

[106] C. Faham, V. Gehman, A. Currie, A. Dobi, P. Sorensen, and R. Gaitskell, "Measurements of wavelength-dependent double photoelectron emission from single photons in VUV-sensitive photomultiplier tubes," *JINST*, vol. 10, no. 09, P09010, 2015. DOI: 10.1088/1748-0221/10/09/P09010. arXiv: 1506.08748 [physics.ins-det].

[107] D. Akerib *et al.*, "Extending light WIMP searches to single scintillation photons in LUX," *Phys. Rev. D*, vol. 101, no. 4, p. 042 001, 2020. DOI: 10.1103/PhysRevD.101.042001. arXiv: 1907.06272 [astro-ph.CO].

[108] M. Szydagis *et al.*, "NEST: A Comprehensive Model for Scintillation Yield in Liquid Xenon," *JINST*, vol. 6, P10002, 2011. DOI: 10.1088/1748-0221/6/10/P10002. arXiv: 1106.1613 [physics.ins-det].

[109] D. S. Akerib *et al.*, "Enhancing the sensitivity of the LUX-ZEPLIN (LZ) dark matter experiment to low energy signals," Jan. 2021. arXiv: 2101.08753 [astro-ph.IM].

[110] E. Aprile *et al.*, "Lowering the radioactivity of the photomultiplier tubes for the XENON1T dark matter experiment," *Eur. Phys. J. C*, vol. 75, no. 11, p. 546, 2015. DOI: 10.1140/epjc/s10052-015-3657-5. arXiv: 1503.07698 [astro-ph.IM].

VITA

My name is Abigail Kopec, I was born February 2, 1994 in Worcester, Massachusetts. I spent the first five years of my life in Shrewsbury, and then moved to Princeton. I attended Thomas Prince School from Kindergarten to eighth grade, where I graduated to Wachusett Regional High School. After graduating from Wachusett, I earned my Bachelor of Science degree from Boston College (BC) with a major in Physics and minor concentrations in Music and Mathematics. After graduating from BC, I began this PhD program at Purdue University.

Here at Purdue, I have conducted research in astroparticle physics, contributing to the XENON projects and building and operating the ASTERiX detector. I have mentored over 100 undergraduates in research projects, particularly through the Data Mine initiative. From here, I will continue astroparticle research with liquid xenon TPCs, and specifically the XENONnT experiment, at the University of California at San Diego as an NSF MPS-Ascend Postdoctoral Fellow.

FELLOWSHIPS AND AWARDS

NSF MPS-Ascend Postdoctoral Fellowship, October 2021 – September 2024, "Rare Event Searches in Liquid Xenon Time Projection Chambers". National Science Foundation.

Charlotte Ida Litman Tubis Award, October 2021, Purdue University.

Excellence in Graduate Teaching Award, May 2021, Purdue University

1st Place Seminar Award, April 2021, "Searching for Dark Matter Interacting with Liquid Xenon". Midwest Graduate Research Symposium.

Indiana Space Grant Consortium Graduate Fellowship, Fall 2020 – Spring 2021, "Search for Solar Neutrinos in XENON1T with Purdue Data Mine". Indiana Space Grant Consortium.

PRESENTATIONS

"Neutrino Physics in XENONnT" (Talk) September 1, 2021. TAUP 2021, Valencia, Spain (Virtual)

"Correlated Single- and Few-Electron Backgrounds in Xenon Detectors" (Talk) April 18, 2021. APS April Meeting 2021 (Virtual)

"Searching for Dark Matter Interacting with Liquid Xenon" (Talk) April 10, 2021. Midwest Graduate Research Symposium, University of Toledo, Ohio (Virtual)

"Searching for Dark Matter with XENON1T" (Seminar) February 26, 2021. IFIRSE, ICISE Center, Quy Nhon, Vietnam (Virtual)

"What's the Matter with the Universe?" (Seminar) January 19, 2021. Science Seminar, Wachusett Regional High School, Massachusetts (Virtual)

"Single- and Few-Electron Backgrounds in Liquid Xenon TPCs (Talk) September 10, 2020. DARWIN Collaboration Meeting, LNGS, Italy (Virtual)

"The XENON Experiments and XENON1T's Recent Low-Energy ER Excess" (Talk) July 15, 2020. Particle Physics Journal Club, Virginia Tech, Virginia (Virtual)

"Single-Electron Background Studies with the Purdue Detector" (Talk) December 10, 2019. DARWIN Collaboration Meeting, LNGS, Italy

"The LBECA Experiment" (Poster) August 1, 2019. APS Division of Particles and Fields 2019, Northeastern University, Massachusetts

"Mitigating Single-Electron Backgrounds in Liquid Xenon TPCs" (Talk) July 17, 2018. Dark Matter Summer School, State University of New York at Albany, New York

"The Case for Dark Matter" (Talk) July 11, 2018. Graduate Student Seminar, Purdue University, Indiana

"Dark Matter" (Workshop) February 10, 2018. Saturday Morning Astrophysics, Purdue University, Indiana

"Long-Range Ion Tracking in XENON1T" (Talk) September 16, 2017. PIKIO IV Conference, University of Kentucky, Kentucky

"Quantum Tunneling and Differential Conductance", "Dark Matter" (Talks) May 2017, May 2018, May 2019. Senior Physics Course Guest Speaker, Wachusett Regional High School, Massachusetts

TEACHING EXPERIENCE

Mentor to Undergraduate Research Students at Purdue University, Spring 2018 – Summer 2021. *Set research goals for up to 25 undergraduates (divided into groups of 3-4) and guide them to attain these goals. I aim to provide an optimal environment to introduce students to physics research and data analysis.*

PHYS 172: Modern Mechanics, Spring 2017, Spring 2018. Teaching Assistant, Purdue University.*Oversaw four 2-hour lab sections per week of 30-50 students. Fourteen lab exercises throughout the semester focus heavily on coding in Visual Python. Checked students' work.*

PHYS 233: Physics for Life Sciences I, Fall 2016, Fall 2017. Teaching Assistant, Purdue University.*Oversaw three/four 2-hour lab sections per week of 20-30 students. Five multi-week lab exercises throughout the semester focused heavily on video capture and motion analysis. Also graded lab reports.*

PHYS 218: General Physics, Summer 2017. Teaching Assistant, Purdue University. *Oversaw two 1-hour recitation and two 2-hour lab sections per week of 20 students. Thirteen recitations focusing on quantitative problem solving and lab exercises testing relationships in classical mechanics.*

Private Tutor at Purdue University, Fall 2016 – Spring 2020. *Aid individual students during 1-hour sessions in problem solving and conceptual understanding of physics, particularly classical mechanics and electromagnetism.*

VOLUNTEER ACTIVITIES

Saturday Morning Astrophysics, Purdue University, September 2017 – May 2021. *On one Saturday per month, spending 2 hours with 5th-12th grade students learning topics in astrophysics and conducting related experiments.*

Physics Graduate Student Association Purdue University, May 2017 – May 2021. *President to plan meetings, organize the committee, and address the department on behalf of the graduate students. (2020 – 2021). Community Building Chair to plan social activities to improve mental health and morale among graduate students. (2019 – 2020). Graduate Student Representative on the department Safety Council to aid with lab safety inspections. (2018 – 2021). Research Progress and Human Resources Peer Contact for any graduate student who may have a grievance with their advisor that interferes with the student's ability to conduct research and graduate in a timely manner. (2018 – 2019). Attend/Plan meetings throughout the academic year to discuss issues faced by physics graduate students.*

Women in Science Programs Purdue University, August 2016 – August 2021. *One evening per month, attending a lecture and dinner advising women in their careers in science fields.*

Purdue Bands and Orchestras Purdue University, May 2017 – December 2020. *Playing trumpet in an ensemble. I have performed with the Symphony Orchestra, Concert Band, Symphonic Band, Summer Band, Philharmonic Orchestra, Commencement Band, and Wind Ensemble.*

All Campus and Community Chorale, West Lafayette, IN, January 2017 – December 2020. *Singing Soprano part in the choir that meets once a week and has one concert per semester.*

Lafayette Citizens Band, Lafayette, IN, June – August 2017, 2018, 2019, 2021. *Playing trumpet in the semi-professional community band with public concerts every Thursday night over the summer.*

PUBLICATIONS

A. Kopec, et al. Correlated Single- and Few-Electron Backgrounds Milliseconds after Interactions in Dual-Phase Liquid Xenon Time Projection Chambers. JINST 16 P07014 (2021). arXiv e-print: 2103.05077

E. Aprile, et al. (XENON Collaboration) Search for coherent elastic scattering of solar 8B neutrinos in the XENON1T dark matter experiment. Phys. Rev. Lett. 126, 091301 (2021). arXiv e-print: 2012.02846

E. Aprile, et al. (XENON Collaboration) Search for inelastic scattering of WIMP dark matter in XENON1T. Phys. Rev. D 103, 063028 (2021). arXiv e-print: 2011.10431

S. Al Kharusi, et al. (SNEWS 2.0 Collaboration) SNEWS 2.0: A Next-Generation SuperNova Early Warning System for Multi-messenger Astronomy. New J. Phys. 23 031201 (2021). arXiv e-print: 2011.00035

E. Aprile, et al. (XENON Collaboration) 222Rn emanation measurements for the XENON1T experiment. Eur. Phys. J. C 81, 337 (2021). arXiv e-print: 2009.13981

M. Clark, et al. Direct Detection Limits on Heavy Dark Matter. Phys. Rev. D 102, 123026 (2020). arXiv e-print: 2009.07909

E. Aprile, et al. (XENON Collaboration) Projected WIMP Sensitivity of the XENONnT Dark Matter Experiment. JCAP 11 (2020) 031. arXiv e-print: 2007.08796

E. Aprile, et al. (XENON Collaboration) Observation of Excess Electronic Recoil Events in XENON1T. Phys. Rev. D 102, 072004 (2020). arXiv e-print: 2006.09721

J. Aalbers, et al. (DARWIN Collaboration) Solar Neutrino Detection Sensitivity in DARWIN via Electron Scattering. Eur. Phys. J. C 80, 1133 (2020). arXiv e-print: 2006.03114

F. Agostini, et al. (DARWIN Collaboration) Sensitivity of the DARWIN observatory to the neutrinoless double beta decay of 136Xe. Eur. Phys. J. C 80, 808 (2020). arXiv e-print: 2003.13407

E. Aprile, et al. (XENON Collaboration) Energy resolution and linearity of the XENON1T in the MeV energy range. Eur. Phys. J. C 80, 785 (2020). arXiv e-print: 2003.03825

A. Bernstein, et al. (LBECA Collaboration) LBECA: A Low Background Electron Counting Apparatus for Sub-GeV Dark Matter Detection. J. Phys. Conf. Ser. 1468 (2020) 012035 TAUP 2019. arXiv e-print: 2001.09311

E. Aprile, et al. (XENON Collaboration) Search for Light Dark Matter Interactions Enhanced by the Migdal effect of Bremsstrahlung in XENON1T. Phys. Rev. Lett. 123, 241803 (2019). arXiv e-print: 1907.12771

E. Aprile, et al. (XENON Collaboration) Light Dark Matter Search with Ionization Signals in XENON1T. Phys. Rev. Lett. 123, 251801 (2019). arXiv e-print: 1907.11485

E. Aprile, et al. (XENON Collaboration) XENON1T Dark Matter Data Analysis: Signal Reconstruction, Calibration and Event Selection. Phys. Rev. D 100, 052014 (2019). arXiv e-print: 1906.04717

E. Aprile, et al. (XENON Collaboration) The XENON1T Data Acquisition System. JINST 14 (2019) no. 07, P07016. arXiv e-print: 1906.00819

E. Aprile, et al. (XENON Collaboration) Observation of Two-Neutrino Double Electron Capture in 124Xe with XENON1T. Nature 568 7753, p532-535 (2019). arXiv e-print: 1904.11002

E. Aprile, et al. (XENON Collaboration) XENON1T Dark Matter Data Analysis: Signal & Background Models, and Statistical Inference. Phys. Rev. D 99, 112009 (2019). arXiv e-print: 1902.11297

E. Aprile, et al. (XENON Collaboration) Constraining the Spin-Dependent WIMP-Nucleon Cross Sections with XENON1T. Phys. Rev. Lett. 122, 141301 (2019). arXiv e-print: 1902.03234

E. Aprile, et al. (XENON Collaboration) First results on the scalar WIMP-pion coupling, using the XENON1T experiment. Phys. Rev. Lett. 122, 071301 (2018). arXiv e-print: 1811.12482

M. Gray, et al. Evidence for Helical Hinge Zero Modes in an Fe-Based Superconductor. Nano Lett. 19, 4890 (2019). arXiv e-print: 1902.10723